International Scientific-Technical and Production Journal

The Paton WELDING JOURNAL

June
2006
6

English translation of the monthly «Avtomaticheskaya Svarka» (Automatic Welding) journal published in Russian since 1948

Founders: *E.O. Paton Electric Welding Institute of the NAS of Ukraine International Association «Welding»* ***Publisher:*** *International Association «Welding»*

Address:
E.O. Paton Electric Welding Institute,
International Association «Welding»,
11, Bozhenko str., 03680, Kyiv, Ukraine
Tel.: (38044) 287 67 57
Fax: (38044) 528 04 86
E-mail: journal@paton.kiev.ua
http://www.nas.gov.ua/pwj

State Registration Certificate
KV 4790 of 09.01.2001

Subscriptions:
$324, 12 issues per year,
postage and packaging included.
Back issues available.

CONTENTS

ROLE OF KEYHOLE IN FORMATION OF DEEP PENETRATION IN A-TIG WELDING OF STAINLESS STEEL

B.E. PATON, K.A. YUSHCHENKO, D.V. KOVALENKO, I.V. KRIVTSUN, V.F. DEMCHENKO and **I.V. KOVALENKO**
E.O. Paton Electric Welding Institute, NASU, Kiev, Ukraine

Given are the results of experimental studies of size and shape of the weld pool in TIG and A-TIG welding of stainless steel of the 12Kh18N10T type (304H) using the surface arc with incomplete penetration. It is suggested that one of the causes of deep penetration in A-TIG welding is formation of a keyhole and associated change in intensity of Marangoni convection. Configurations of the free surface and bottom of the weld pool, which are characteristic of A-TIG welding, confirm this mechanism of deep penetration.

Keywords: TIG and A-TIG welding, arc, weld pool, penetration, keyhole, Marangoni convection, stainless steel

A-TIG welding (TIG welding over the layer of activating flux) is a simple and effective alternative to TIG welding, as well as to plasma, laser and electron beam welding. In A-TIG welding with the surface arc the penetration depth increases more than 3 times, compared with TIG welding. The A-TIG method allows square-groove welding of different metals in one pass using no filler wire, e.g. butt joints in steels of small and medium thickness (from 1 to 12 mm) can be made by one-sided welding, butt joints in steels from 6 to 25 mm thick can be made by two-sided welding, and root welds can be made by welding in groove with increased root face (4–6 mm). Furthermore, A-TIG welding provides welds of the consistent size and quality on steels of the same grades independently of cast to cast variations, and allows distortion and shrinkage of welded joints to be decreased [1–4].

Different hypotheses have been put forward recently concerning causes and mechanisms of an increased penetration depth in A-TIG welding, compared with the TIG process. The hypotheses offered can be merged into two groups:

- change in character and structure of hydrodynamic flows in the weld pool depending upon the direction of the Marangoni flow [5, 6], and growth of the role of ponderomotive (Lorentz) forces in formation of the flow of molten metal [7, 8];
- contraction of the arc due to electronegative elements present in an activating flux and its insulating effect, and an associated increase in the current density and, therefore, concentration of the thermal effect of the arc on the weld pool surface [2, 9–11].

As shown by our earlier studies of TIG and A-TIG welding of stainless steel 304H (using aerosol oxide activator PATIG S-A), increase in the arc current is accompanied by re-distribution of the effect of mechanisms of deep penetration (the first and second hypotheses) on the penetrating capacity of A-TIG welding. In particular, contraction of the arc turns out to be the most important factor in welding at low (100 A and below) currents. As the current is increased from 100 to 150 A, the effect of the arc contraction on the penetration depth and weld formation is mitigated more than twice in the total balance of mechanisms causing deep penetration in A-TIG welding.

Investigations of the process of penetration of base metal are usually conducted on the basis of analysis of the weld size (penetration depth, width and aspect ratio of the weld). At the same time, the issue of distortion of the free surface of molten metal, which, in our opinion, may have a substantial effect on weld formation, is underestimated in literature dedicated to A-TIG welding.

Based on analysis of experimental data on the surface geometry of the weld pool in TIG and A-TIG welding of stainless steel 304H with incomplete penetration, this study offers a hypothesis on the formation of a quasi-keyhole in A-TIG welding using the surface arc, and the role of this keyhole in intensification of convective heat transfer in molten metal, providing deep penetration.

Experimental results. Welding experiments were conducted on stainless steel 304H (0.006 % S, 0.006 % O) plates measuring 150 × 50 × 9 mm. A controlled uniform activator layer 5 mm wide and 20 μm thick was deposited on the plate surface prior to A-TIG welding. Thickness of the activator layer was controlled using the special thickness gauge TP-34 based on an eddy current converter. The following oxide compounds were used separately as activators: Al_2O_3, MgO, CaO, SrO, Cr_2O_3, MnO, CoO, Fe_2O_3, Ga_2O_3, In_2O_3, GeO_2, SnO_2, V_2O_5, MoO_3, TiO_2, and SiO_2.

The experiments were conducted using the TIG welding machine OB-2279 equipped with a thyristorised power unit VSVU-315.

The following welding parameters were used for the experiments: welding current — 100, 150 and 200 A, arc length — 1.5 mm (set distance from the tungsten electrode tip to the plate surface prior to welding), welding speed — 100 mm / min, shielding gas — argon, tungsten electrode (2 % Th) with a 3.2 mm diameter, 30° pointing angle, and 0.5 mm tip surface.

As it is difficult to control profile and measure size of the liquid pool during the welding process, the use was made of the following procedure. The arc was instantaneously extinguished during welding by switching off the power unit and stopping movement of a sample relative to the tungsten electrode. Shape of the solidified metal surface can be regarded in first approximation as a profile of the free surface of the liquid weld pool. Analysis of this shape and measurement of geometric sizes of its surface were made on macrosections of a sample cut both across the weld within the zone of the crater centre and along the weld.

Appearances of surfaces of the solidified weld pools in TIG and A-TIG welding are shown in Figure 1, *a*, *b*. Corresponding macrosections cut from the transverse and longitudinal sections of the welds are shown in Figure 2. To analyse profiles of bottom and free surface of the weld pool in a longitudinal section of the weld, we will use the common scheme of location of electrode with respect to the pool and its characteristic geometric size in TIG and A-TIG welding (Figure 3). Values of geometric parameters shown in this Figure for different welding conditions are given in the Table.

Comparing profiles of surfaces of the longitudinal and transverse sizes of the weld pools in TIG and A-TIG welding revealed the presence of substantial differences between them (see Figures 1 and 2, and Table). This seems to indicate to different penetration mechanisms characteristic of these welding methods. In particular, analysis of size and shape of the external surface of the solidified pools in TIG and A-TIG welding showed the following. The leading and tailing portions of the weld pool surface in A-TIG welding have a convex shape with a clearly defined characteristic recess (depression) near the crater centre (see Figures 1, *b* and 2, *b*, *d*), which is especially pronounced in the transverse section of the weld (see Figure 2, *b*). No such big recess is seen in TIG welding (Figures 1, *a* and 2, *a*, *c*). The depth of this recess increases with increase in the arc current when using all oxides investigated. At the same time, this depth at the identical values of the welding current differs for different oxides. Oxides can be ranked as follows as to the degree of increase in crater depth H_{cr} with simultaneous increase in penetration depth H_{pen}: Al_2O_3, MgO, CaO, SrO, Cr_2O_3, MnO, CoO, Fe_2O_3 — characterised by a lower penetration degree, and Ga_2O_3, In_2O_3, GeO_2, SnO_2, V_2O_5, MoO_3, TiO_2, SiO_2 — characterised by a higher penetration degree. Variations in H_{cr} and H_{pen} in the case of using three characteristic oxides (TiO_2, Fe_2O_3, Al_2O_3) are shown in Figure 4.

Analysis of longitudinal sections of TIG and A-TIG welds showed the following. Both in TIG and A-TIG welding, positions of points of the maximal sag (crater recesses) of the weld pool surface, $L_{H_{cr}}$, and maximal penetration depth, $L_{H_{pen}}$, are shifted to the tungsten electrode axis towards the tailing portion of the pool. In the case of A-TIG welding, this shift increases with increase in the welding current, and changes depending on the type of the oxide used. However, other conditions being equal, it is smaller in A-TIG welding than in TIG welding. Figure 5 schematically shows the results of analysis at I_w = 200 A.

Experimental results and discussions. Analyse the above experimental results in terms of the probable mechanism of deep penetration in A-TIG welding. Having two factors causing distortion of the free surface of the weld pool, i.e. gas-dynamic pressure of the arc column and vapour recoil pressure, first we will consider the former. Motion of plasma of the arc column is known to occur under the effect of the rotation component of Lorentz force, which is centripetal (directed to the axis of the arc column) under the conditions of axial symmetry of the electromagnetic field in the arc column. In TIG welding, the diagram of distribution of magnetic pressure in height of the arc column has maximum near the cathode, where the current density is maximal. Therefore, the flow of plasma is formed in the arc column in axial direction (from cathode to anode). While interacting with the weld pool surface, this flow spreads to form the char-

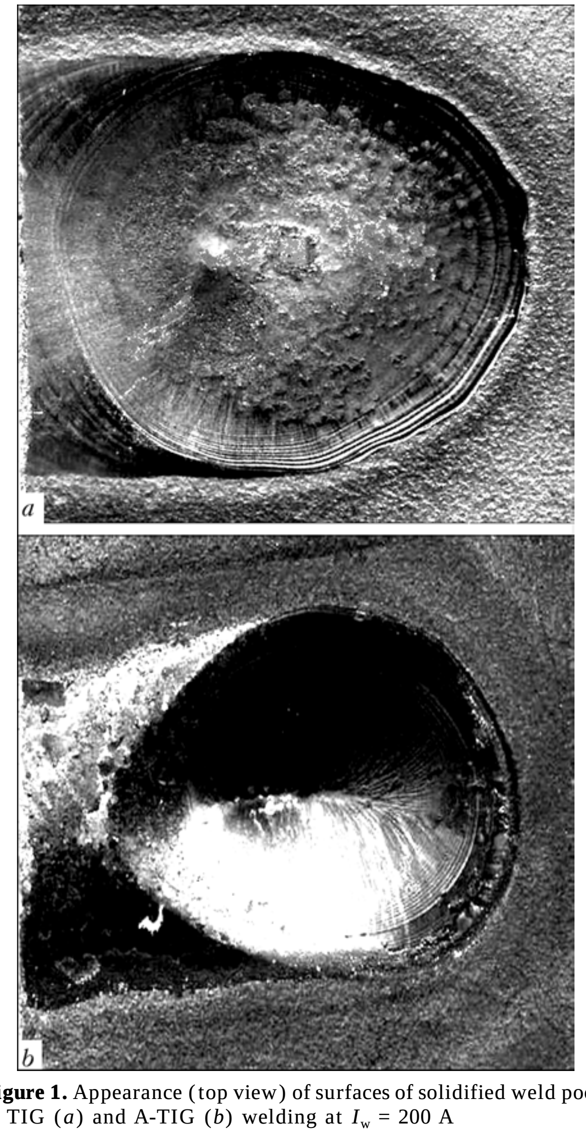

Figure 1. Appearance (top view) of surfaces of solidified weld pools in TIG (*a*) and A-TIG (*b*) welding at I_w = 200 A

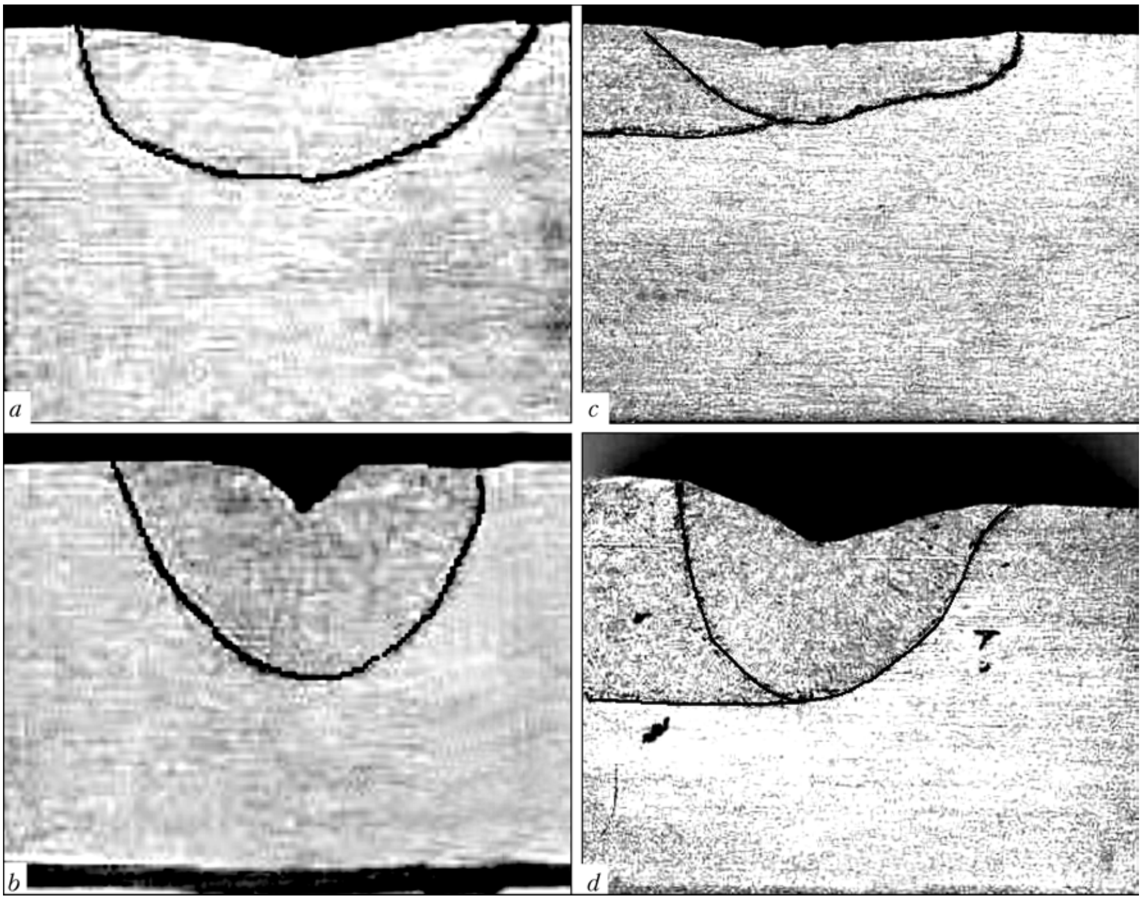

Figure 2. Transverse (*a, b*) and longitudinal (*c, d*) sections of solidified weld pools in TIG (*a, c*) and A-TIG (*b, d*) welding at I_w = 150 A

acteristic bell-shaped arc. Gas-dynamic pressure forming in the near-anode regions leads to certain distortion of the free surface of the weld pool.

The situation is different in the case of A-TIG welding. It is a common opinion that the arc contraction takes place in welding over the layer of an activating flux, which shows up as reduction in area of the anode spot to a size comparable with area of the cathode region. Distribution of current density in height of the arc column in this case has two maxima located near the cathode and anode. Distribution of the rotation component of Lorentz force is of a similar character, thus driving two opposite plasma flows directed from the cathode and anode to the middle (in height) part of the column. Their interaction results in a barrel-shaped plume with a maximal pressure at the point where the plasma flows collide. Therefore, the gas-dynamic pressure of the arc column is not a key factor that causes distortion of the free surface of the weld pool in A-TIG welding. Note that we may speak about the phenomenon of arc contraction in A-TIG welding only with a certain degree of conventionality, given that this term implies, first of all, a reduction in area of the anode spot.

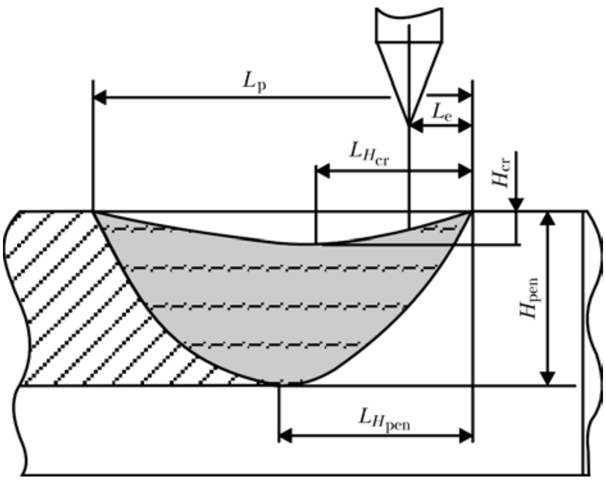

Figure 3. Schematic of measuring characteristic sizes of weld pools in TIG and A-TIG welding: L_p — pool length; L_e — distance from leading portion of the pool to electrode axis; $L_{H_{cr}}$, $L_{H_{pen}}$ — distances from leading portion of the pool to a point of maximal crater and penetration depths, respectively; H_{cr}, H_{pen} — crater and penetration depths, respectively

Consider two characteristic cases in analysis of the effect of arc contraction on the penetration depth. The

Welding parameters and geometric sizes of weld pools in TIG and A-TIG welding of steel 304H 9 mm thick

Welding method (oxide)	I_w, A	L_p, mm	H_{cr}, mm	L_e, mm	$L_{H_{cr}}$, mm	$L_{H_{pen}}$, mm	H_{pen}, mm
TIG	100	5.5	0.20	2.5	3.2	3.9	1.0
A-TIG (TiO_2)	100	4.5	0.50	1.6	2.1	3.0	2.2
TIG	150	8.2	0.35	3.0	5.5	6.7	2.5
A-TIG (TiO_2)	150	7.5	1.20	2.0	4.6	5.5	5.7
TIG	200	11.5	0.50	3.6	9.5	10.0	3.1
A-TIG (TiO_2)	200	9.0	1.50	2.5	8.0	7.7	6.2

pool of a small cross section is formed in A-TIG welding at low (up to 100 A) currents. The surface tension force generated in this case, which is proportional to the radius of curvature of the surface, prevails over the pressure of the vapour recoil reaction, this hampering distortion of the free surface of the weld pool. Therefore, the main factor that determines penetration of base metal in welding at low currents is transfer of heat from the overheated region located near the anode spot deep into metal, according to the mechanism of heat conduction and convection developing in the field of bulk forces (Lorentz and Archimede forces).

At increased (from 100 to 200 A) currents, the effect of the arc contraction and associated local increase in temperature of the weld pool surface within the anode spot cannot provide such a high increase in the penetration depth as that taking place in A-TIG welding. In our opinion, to increase the penetration depth in this case, it is necessary not only to overheat the sub-surface metal layer, but also to ensure conditions for distortion of the free surface of the melt to move the heat source closer to the pool bottom (similar to welding using high power density heat sources, such as laser and electron beam welding [13, 14]). In the case of a small area of the free surface of the weld pool, this distortion is hampered by a high level of surface tension forces. These conditions can be realised in intensive evaporation of metal from the weld pool surface due to the reaction of recoil of the expanding vapour jet and decrease in the surface tension factor of the melt in the overheated region. It is very likely that a corresponding increase in density of the heat flow at the anode, caused by the arc contraction, can ensure local overheating and evaporation of molten metal, and lead to a substantial distortion of the weld pool surface and formation of the quasi-keyhole [15].

As found by experimental studies [16], the density of the heat flow is $1\cdot10^4$ W / cm^2 and higher as a result of the arc contraction in A-TIG welding at a welding current of 200 A. It is reported [14] that to provide intensive evaporation of metal its surface should be heated by a heat source with the heat flow density in the heating spot equal to about $1\cdot10^5$–$1\cdot10^6$ W / cm^2. Although the heat flow density in the anode spot in A-TIG welding is lower than that achieved with beam welding methods (arc power is distributed over the free surface of the weld pool in a spot of a much bigger size, compared with a conventional focal spot). However, in our opinion, this density may be sufficient to provide overheating of the melt surface to a temperature close to the boiling point and higher. This causes intensive evaporation of metal of the weld pool, and its free surface is distorted under the effect of the vapour recoil reaction to form a crater and keyhole [16], where the processes of scattering and condensation of vapours take place, similar to those occurring in narrow and deep keyholes formed in electron beam and laser welding, although in A-TIG welding they are not that pronounced. In this respect, A-TIG welding at increased currents takes an intermediate position between the arc and beam welding methods.

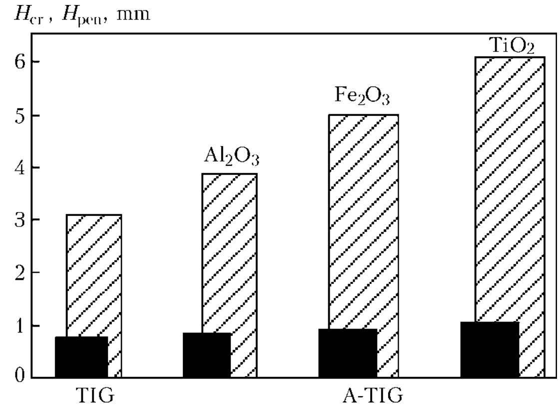

Figure 4. Effect of TIG and A-TIG welding processes using different oxides on the depth of crater H_{cr} (black region) and penetration H_{pen} (dashed region) of weld pools at I_w = 200 A

The data on the penetrating capacities of TIG and A-TIG welding, shown in Figure 4, evidence that increase in the penetration depth in A-TIG welding is much bigger than the maximal sag of the free surface. Therefore, because of a local effect, deep penetration in A-TIG welding cannot be attributed only to deepening of the heat source (anode spot) and its movement closer to the weld pool bottom. It seems highly probable that there exists also some other mechanism that provides this penetration.

To further study the mechanism of deep penetration in A-TIG welding, consider the Marangoni convection driven by the capillary surface force generated by gradient of the surface tension factor over the weld pool surface. In contrast to TIG welding, where the capillary force is directed opposite to the temperature gradient, i.e. from centre to periphery of the weld pool, in A-TIG welding the capillary force acts in the opposite direction as a result of activation of the free surface of the melt [5, 6]. This capillary force drives the melt flow in a sub-surface layer of the weld pool, which in A-TIG welding is directed towards the heat centre of the free surface of the pool (towards the anode spot). If the free surface of the weld pool is distorted insignificantly, the melt flows directed to the weld pool centre towards each other loose their momentum. As a result, the downward flow of the

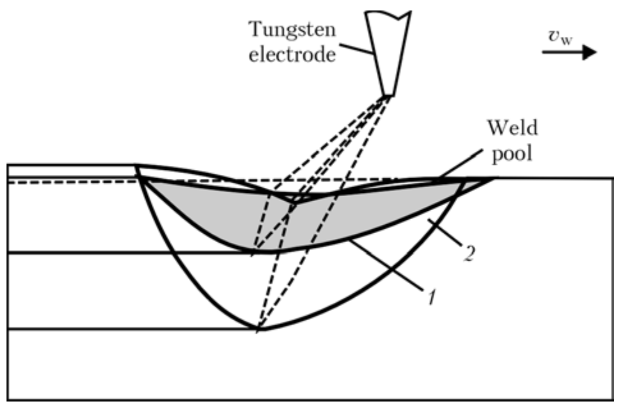

Figure 5. Schematic diagram of longitudinal sections of solidified weld pools in TIG (*1*) and A-TIG (*2*) welding at I_w = 200 A

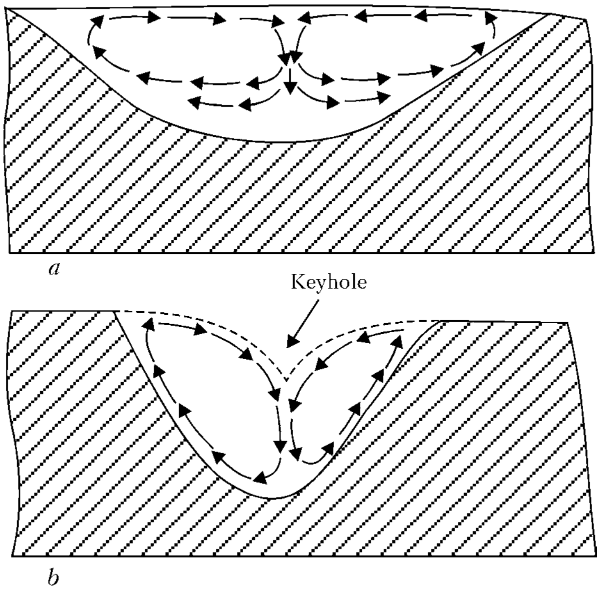

Figure 6. Schematic of Marangoni convection in the case of flat (*a*) and distorted (*b*) surface of the weld pool

melt becomes of low intensity (Figure 6, *a*), and the formed vortex flow localised in upper portion of the weld pool has a limited effect on the penetration depth. Hydrodynamic situation in the weld pool substantially changes in the case of a keyhole formed on the pool surface as a result of the vapour recoil reaction. In this case, the melt flows moving along an inclined surface of the keyhole will meet at angle $\alpha \approx 45°$ (or, probably, higher). As a result of hydrodynamic interaction of these flows, their momenta sum up to form an intensive downward jet flow (Figure 6, *b*), which can effectively transport overheated metal to the pool bottom, thus providing a substantial increase in the penetration depth. Therefore, the keyhole can be regarded as a geometric factor of activation of the Marangoni flow, which enhances the downward flow of the overheated melt to the weld pool bottom. Near the pool bottom, this flow turns towards the side walls of the weld pool. The barrel-shaped cross section of the weld seen in some experiments is most probably related to the fact that the return flow of the melt retains the temperature sufficient for incipient melting of side edges.

The suggested mechanism of deep penetration in A-TIG welding requires further investigations to precisely determine the current density in the anode spot and shape of the free surface of the weld pool, and fix the actual profile of the quasi-keyhole during the welding process. Mathematical modelling of 3D heat and mass transfer processes and hydrodynamics of the weld pool, allowing for interaction of mass and capillary forces, distortion of the free surface of the weld pool, evaporation and convection of the material, as well as peculiarities of arcing under the A-TIG conditions, is also of an undoubted interest. The model of such a structure will make it possible to quantitatively estimate the role of the keyhole and Marangoni convection in formation of deep penetration in A-TIG welding.

CONCLUSIONS

1. Characteristic crater with a recess (depression) is formed on the free surface of the weld pool near its centre in A-TIG welding. As the arc current is increased, this recess becomes narrower and more elongated in the longitudinal section of the weld, which is usually the case of welding using high power density heat sources resulting in formation of a keyhole, and the crater and penetration depth increases when using all oxides under consideration.

2. Both in TIG and A-TIG welding, positions of points of a maximal sag of the weld pool surface and maximal penetration depth were found to shift with respect to the tungsten electrode axis towards the tailing portion of the pool. In the case of A-TIG welding, this shift is smaller than in TIG welding, other conditions being equal.

3. It is suggested that hydrodynamic interaction of the melt flows driven by the surface tension gradient under conditions of a distorted free surface of the weld pool (A-TIG welding at high currents) leads to formation of an intensive downward flow, which transports overheated metal from the anode spot to the pool bottom, thus providing a substantial increase in the penetration depth.

1. Yushchenko, K.A., Kovalenko, D.V., Kovalenko, I.V. (2001) Application of activators for TIG welding of steels and alloys. *The Paton Welding J.*, **7**, 37–43.
2. Savitsky, M.M., Kushnirenko, V.N., Olejnik, O.I. (1999) Peculiarities of TIG welding with activating fluxes (A-TIG process). *Avtomatich. Svarka*, **12**, 20–26.
3. Lucas, W., Howse, D. (1996) Activating flux — increasing the performance and productivity of the TIG and plasma processes. *Weld. and Metal Fabr.*, **1**, 11–15.
4. Lucas, W. (2000) Activating flux — improving the performance of the TIG process. *Ibid.*, **2**, 7–10.
5. Heiple, C.R., Roper, J.R., Stagner, R.T. et al. (1983) Surface active element effects on the shape of GTA, laser and electron beam welds. *Welding J.*, 62(**3**), 72–77.
6. Tanaka, M., Shimizu, T., Terasaki, H. et al. (2000) Effects of activating flux on arc phenomena in GTAW. *Sci. and Techn. of Weld. and Joining*, 5(**6**), 397–402.
7. Ostrovsky, O.E., Kryukovsky, V.N., Buk, B.B. et al. (1977) Effect of activating fluxes on penetrability of welding arc and power concentration in anode spot. *Svarochn. Proizvodstvo*, **3**, 3–4.
8. Zamkov, V.N., Prilutsky, V.P. (2004) Theory and practice of TIG-F (A-TIG) welding (Review). *The Paton Welding J.*, **9**, 11–14.
9. Paton, B.E., Zamkov, V.N., Prilutsky, V.P. et al. (2000) Contraction of the welding arc caused by the flux in tungsten-electrode argon-arc welding. *Ibid.*, **1**, 5–11.
10. Lucas, W., Howse, D., Savitsky, M.M. et al. (1996) A-TIG — increasing the performance and productivity of the TIG process. *IIW Doc. XII-1448–96*.
11. Lowke, J., Tanaka, M., Ushio, M. (2004) Insulation effects of flux layer in producing greater weld depth. *IIW Doc. 212-1053–04*.
12. Yushchenko, K.A., Kovalenko, D.V., Kovalenko, I.V. (2005) Comparative analysis of TIG and A-TIG welding of stainless steel. *IIW Doc. 212-1088–05*.
13. Leskov, G.I., Trunov, E.N., Zhivaga, L.I. (1976) Shape, size and stability of keyhole in electron beam welding of metal. *Avtomatich. Svarka*, **6**, 13–17.
14. Arutyunyan, R.V., Baranov, V.Yu., Bolshov, L.A. et al. (1989) *Effect of laser radiation on materials*. Moscow: Nauka.
15. Paton, B.E., Yushchenko, K.A., Kovalenko, D.V. et al. (2005) Formation of quasi keyhole is a cause of deep penetration in A-TIG welding of stainless steel. *IIW Doc. 212-1085–05*.
16. Yushchenko, K.A., Kovalenko, D.V., Kovalenko, I.V. (2003) Investigation of peculiarities of A-TIG welding of stainless steels. *IIW Doc. 212-1047–03*.

EFFECT OF SCANDIUM ADDITIONS ON STRUCTURE-PHASE STATE OF WELD METAL IN ALUMINIUM ALLOY JOINTS AFTER HEAT TREATMENT

L.I. MARKASHOVA, G.M. GRIGORENKO, A.V. LOZOVSKAYA, O.S. KUSHNARYOVA and **V.E. FEDORCHUK**
E.O. Paton Electric Welding Institute, NASU, Kiev, Ukraine

Effect of heat treatment (ageing at 350 °C, 1 h) on changes in structure-phase composition of weld metal in 1460 alloy joints produced by argon-arc welding using Sv1201 and Sv1201 + 0.5 % Sc fillers is considered. It is shown that heat treatment leads to a considerable increase in volume fraction of fine phases, differing in morphology and phase composition. In metal containing no scandium, Al–Cu phases differing in copper concentration are formed, while Al–Li phases have a more complex structure due to inclusions of fine Al–Zr and Al–Cu phases. Complex phase precipitates of the lamellar (Al–Cu / Al_3Sc) and globular (Al--Li / Al–Zr, Al–Sc) types are formed in Sc-containing metal.

Keywords: welded joints, aluminium alloy, heat treatment, scandium, structure-phase transformations, dislocation density, composite phase precipitates

Aluminium-lithium alloys which relate to ageing alloys are characterised, as a rule, by a complex structure-phase state, which is caused in many respects by specifics of structure and phase transformations occurring during the technological cycle of their production and subsequent heat treatment.

Phase components of metals in general [1, 2], and those of aluminium alloys in particular, are known to play a specific role in changing different mechanical and service properties, such as strength, ductility, crack resistance, fracture toughness, resistance to cyclic loading, etc. [3, 4]. In a number of studies the effect of strengthening of Al–Li alloys is related, for example, to refining of grain structure [5], which is attributable to phase precipitates of the Al--Sc type. Other studies [6, 7] report that adding scandium to aluminium alloys provides strengthening due to refining of not only grains, but also directly particles of the α'-phase (Al_3Sc) formed during the ageing process. In this connection, to achieve optimal strengthening, it is suggested that the temperature range of ageing should be limited (300--350 °C), and holding time should be reduced from 6 to 1 h.

Investigation of the effect of temperature parameters of heating of the above ageing Al–Li alloys on changes in phase composition shows that the primary Al_3Sc particles do not dissolve in a temperature range of 450--500 °C [8]. However, weak super structural reflections are fixed, along with the characteristic signs of the primary Al_3Sc phases, which may be indicative of the presence of the δ'-phase (Al_3Li), although actually no phases of this type were detected [9, 10], which may be related to their fine size and low density of distribution in metal.

Also, it is thought that a peculiar feature of alloys of the Al–Li–Sc system is formation of phase precipitates of a composite type, having the form of two-layer particles that consist of a nucleus of the α'-phase (Al_3Sc) and shell of the δ'-phase (Al_3Li), which forms in heterogeneous nucleation of the latter at the interface of the Al_3Sc phase. As evidenced by a brief analysis of available literature data, these alloys are characterised by a wide variety of phase precipitates that experience complex transformations depending upon the temperature conditions of treatment, while the presence of such phase precipitates determines in many respects properties of the alloys.

As far as the welded joints in Al--Li alloys are concerned, as follows from [11], complexity of a technological process, which comprises welding (as a result of which the material acquires a non-equilibrium state) and postweld heat treatment, does not allow an unambiguous interpretation of the character of phase transitions in the weld metal and heat-affected zone.

Results of examinations of phase transformations in the weld metal immediately after welding are given in studies [12, 13], together with the data on variations in structure-phase composition of alloys depending upon the presence of scandium.

The purpose of this study was to examine structure-phase changes in the weld metal caused by subsequent (postweld) heat treatment, i.e. ageing.

Examinations were conducted on welds (heat treatment at 350 °C, 1 h) produced in alloy 1460 (Al–3 % Cu–2 % Li–0.08 % Sc) using fillers Sv1201 (Al–6.5 % Cu--0.25 % Zr–0.3 % Mn) and Sv1201 + 0.5 % Sc.

The examinations were carried out by the transmission electron microscopy methods using instrument JEM-200CX at an accelerated voltage of 200 kV. This examination method was chosen as the only possible one, allowing revealing the actually formed structures (sub-granular, dislocation) and phase precipitates at different stages of their formation.

Specimens for examinations were cut from the central part of the welds by electric spark cutting, successive mechanical and electrolytic thinning of the resulting washers with subsequent multiple ion thinning in the machine [14] with ionised argon flows.

Fine structure and distribution of phase precipitates in the bulk of grains and along the grain boundaries, character of precipitates of the eutectic type, and other peculiarities of structure-phase state of the weld metals differing in chemical composition, i.e. with and without scandium, were examined.

Intragranular structure of the weld metal produced by using the Sv1201 filler (without scandium) is characterised by a generally low dislocation density $\rho = 6\cdot10^{8}$–$2\cdot10^{9}$ cm^{-2}, as well as a non-uniform distribution of crystalline lattice defects. Some local increase in the dislocation density was fixed in the phase precipitate formation zones (Figure 1, *a*–*c*).

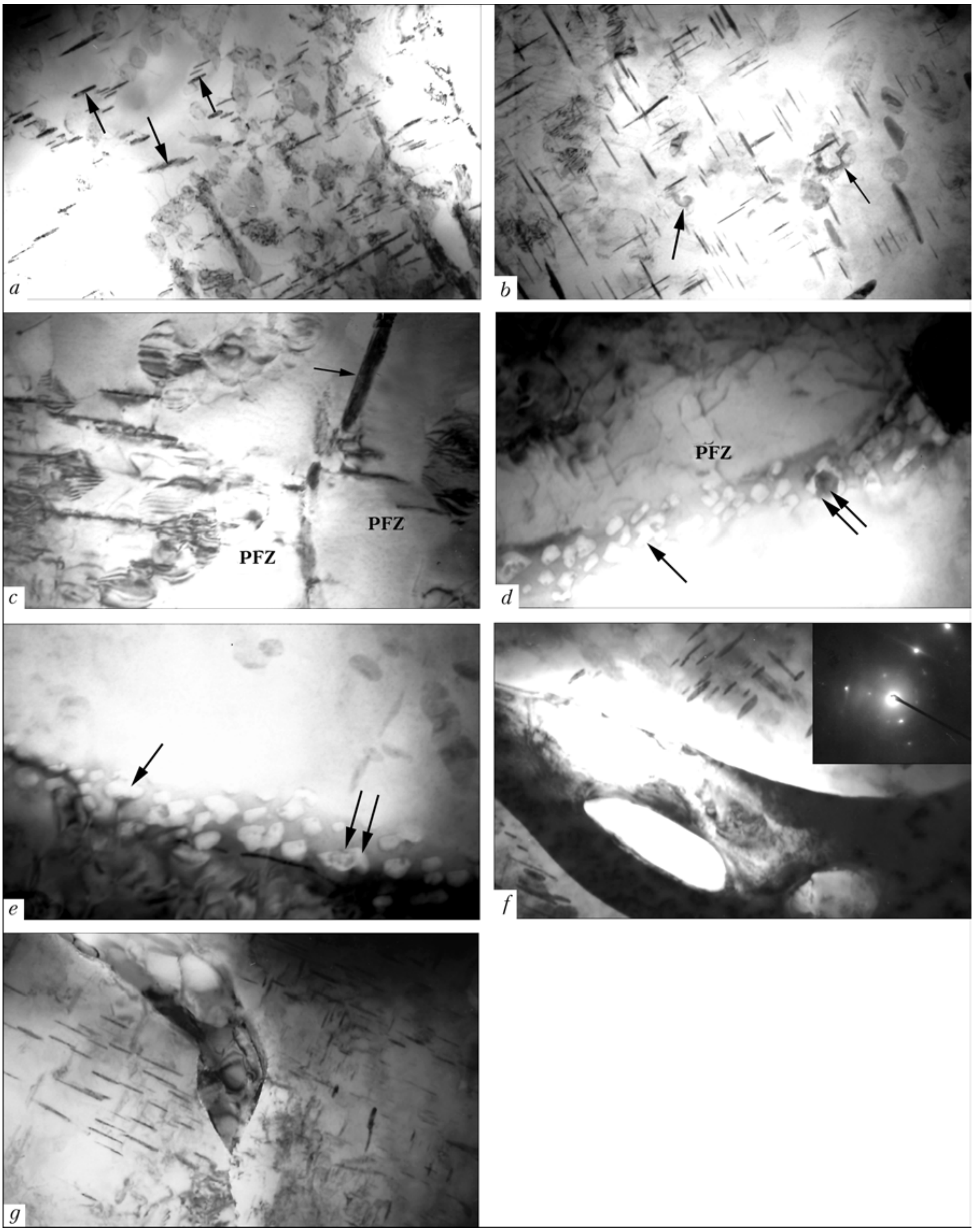

Figure 1. Phase precipitates and fine structure of weld metal on aluminium alloy 1460 (Al–Cu–Li) after heat treatment (ageing at 350 °C, 1 h): *a*, *b* — distribution of θ′-phases (Al_2Cu) and lithium δ′-phases (Al_3Li) in the bulk of grains (single arrows — lamellar θ′-phases, double arrows — β′-phase (Al_2Zr), ×20,000 (*a*); lithium δ′-phases, ×30,000 (*b*)); *c* — decrease in density of distribution of θ′- and δ′-phases in boundary zones free from phase precipitates (PFZ), ×30,000; *d*, *e* — dense clusters of lithium phase (single arrows) along the intergranular boundaries; δ′-phases of the composite type (double arrows), ×50,000; *f*, *g* — eutectic precipitates at grain boundaries, ×30,000 and ×20,000, respectively

The following can be distinguished in character of formation of intragranular phase precipitates. Phase precipitates of different sizes (coarse precipitates mostly of a globular shape with diameter $d_{p.p} \sim 1.5$–2.0 μm) were fixed in the bulk of grains. Formations of this type are, as a rule, a complex conglomerate consisting mainly of the θ′-phases (Al_2Cu) with inclusions of the β′-phases (Al_3Zr). Phase precipitates of the other type are of a much smaller size and have a more diverse morphology: rod-type (lamellar) precipitates $l \sim 0.1$–0.5 μm long and $h \approx 0.01$–0.03 μm thick, as well as globular precipitates with $d_{p.p} \approx 0.10$–0.15 μm (see Figure 1, *a*–*c*). Precipitates of the lamellar type are the θ′-phase (Al_2Cu). Growth of phase precipitates of this type occurs due to coalescence of growing fine lamellae of the θ′-phases (Figure 1, *b*, *c*). It should be noted that precipitation of the θ′-phases occurs at fine particles of either β′-phases (Al_3Zr) (Figure 1, *a*), or δ′-phases (Al_3Li) (Figure 1, *b*). The latter is indicative of the fact that particles of the composite type may have not only globular, but also irregular geometric shape.

Structure of intergranular boundaries and grain-boundary interlayers markedly changes compared with that formed immediately after welding (Figure 1, *d*, *e*). Thickness of interlayers of this type after heat treatment (350 °C, 1 h) is $h \approx 0.25$–0.35 μm. Differences in phase composition of grain-boundary precipitates (GBP) were also fixed. For example, isolated Li-containing phase precipitates can be clearly seen in some cases in GBP. These precipitates have different morphology, mostly globular and elongated shape. They are (0.05–0.15) × (0.40–0.50) μm in size and 0.05–0.10 μm in diameter. In other cases GBP are dense elongated lamellae, comparatively homogeneous in contrast, the composition of which corresponds to the θ′-phases (Al_2Cu) (Figure 1, *c*, marked by arrows).

Also fixed were GBP of a more complex composition, having the form of a composite consisting of formations that differ in contrast and, hence, in density of the phases (see Figure 1, *d*, *e*). Formations of this type are characterised by rather coarse sizes and consist primarily of Al–Li and Al–Cu phases of the AlLi and Al_2Cu types (0.5 × 1.0 μm). Less often are GBP with finer (0.05 × 0.10 μm) inclusions of the Al_3Zr phases.

Of special notice is the presence of grain-boundary precipitation-free zones (PFZ) with $h = 0.44$–0.60 μm, the dislocation density of which substantially decreases after heat treatment (Figure 1, *d*, *e*).

Characteristic type of eutectic formations in the weld metal after heat treatment is shown in Figure 1, *f*, *g*. As seen from the Figure, the eutectic consists of isolated phases and their conglomerates.

Structure of the heat treated weld metal containing 0.25 % Sc is characterised by the following. A large amount of phase formations was revealed in the bulk of grains and along their boundaries, that were substantially different in size, internal structure and morphology from those revealed in the weld metal containing no scandium.

Whereas the volume fraction of inclusions of coarse phases ($d \sim 1.5$–2.0 μm) having a composite structure was almost identical in both cases, the content of phase precipitates of medium ($d_{p.p} \sim 0.2$–0.5 μm) and finer sizes (hundredths of a micrometer) in the Sc-containing weld metal was markedly higher (Figure 2, *a*–*c*), the latter filling (or considerably reducing) PFZ adjoining the grain boundaries (Figure 2, *d*, *e*).

Examinations of the composition of phase formations show that phases of a rod or lamellar shape (it is likely that the difference in shape is associated with the location of phases with respect to the plane of a foil examined) are precipitates of the θ′-phases (Al_2Cu), which is proved by their micro diffraction reflections in transmission examination of thin foils. The θ′-phases have complex (composite) structure. Also the layers of a dark contrast were fixed (Figure 2, *b*–*e*), along with lamellae of a grey contrast, characteristic of the Al_2Cu phases. Micro diffraction analysis, combined with dark field image filming of individual components of the phases revealed the presence of the α′-phases (Al_3Sc), in addition to the Al_2Cu phases. Phases containing scandium were revealed also in composite precipitates located directly along the grain boundaries (Figure 2, *e*, *g*). Also, phases of other compositions, e.g. Li-containing phases, having the form of disks and squares not more than 0.1 μm in size (Figure 2, *d*), as well as Zr-containing phases (Al_3Zr) with $d \sim 0.04$ μm or less (Figure 2, *a*, *e*), were revealed among the ultra fine phases of the composite type.

As a rule, the Zr-containing phases are fixed at the centre of phases of other composition. It is likely that this is associated with the temperature range of nucleation of phases that form a composite.

In this case, such nucleation centres are most probably the Al_3Zr and Al_3Sc type phases, as they have the highest nucleation temperature [1]. Of special notice is the fact that the Zr-containing phases are finest of those characteristic of the material examined, and they precipitate comparatively uniformly in the bulk of metal. This may create conditions for subsequent uniform precipitation and growth of other phases.

Unlike eutectic zones in the as-welded metal, during postweld heat treatment the grain-boundary eutectics disintegrate to a considerable degree and decompose into isolated phase components (Figure 2, *g*, *h*), this leading to substantial refining of the isolated phase precipitates in the eutectic. In addition, some fine phase precipitates in the eutectic lose their clearly defined contours, and a segregation contrast forms around the phases. This fact points to the active processes of diffusion dissolution. The most stable of them seem to be the Li-containing phases.

Also, of notice are peculiarities of the dislocation structure of the weld metal in the case of using Sc-containing fillers. The heat treatment process leads to a substantial increase in the dislocation density in the

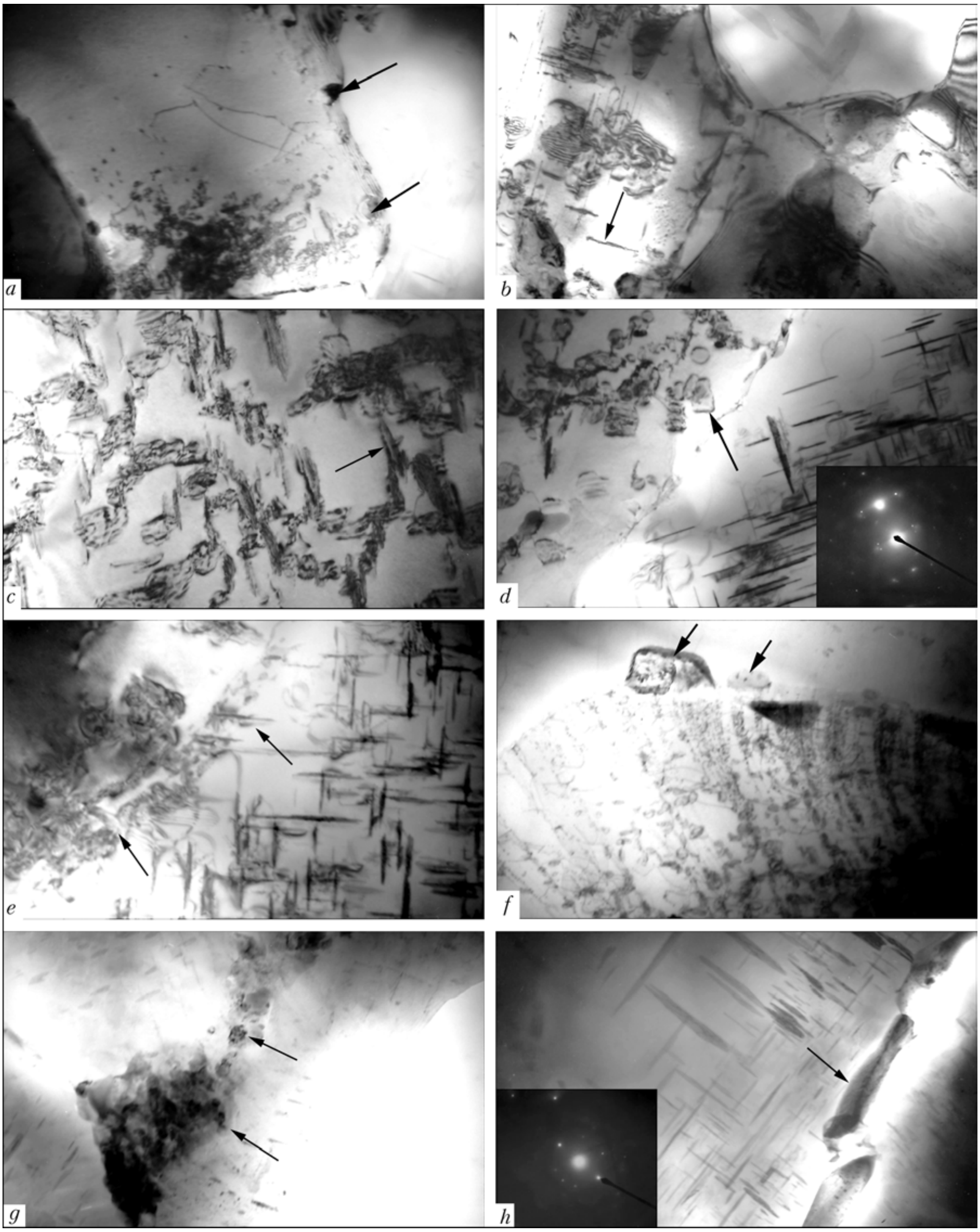

Figure 2. Microstructure of metal of welded joint in aluminium alloy 1460 (Al--Cu--Li) with 0.25--0.30 % Sc after heat treatment (ageing at 350 °C for 1 h): *a* — distribution of fine scandium phases (single arrows) along the boundaries and sub-boundaries; double arrows — β'-phase (Al_3Zr), ×15,000; *b, c* — distribution of composite θ'-phases (Al_2Cu) (arrows) and formation of cellular structure in the bulk of grains, ×20,000; *d, e* — distribution of scandium and lithium composite phases (arrows) within the zone of grain boundaries, ×30,000; *f* — coarse composite Al_3Sc-based phases at grain boundaries, ×30,000; *g, h* — loose (×30,000) and dense (×20,000) grain-boundary eutectics of composite type

weld metal. It is likely that this is caused by a considerable violation of coherency of lattice of the matrix and forming phase, and variation in the stressed state at the matrix–phase interface. The level of stresses in the region of decomposition (which is evidenced by a high local dislocation density) is much in excess of the level of elastic stresses characteristic of coherent bonds. The presence of scandium seems to activate metal in decomposition of solid solution during heat treatment.

The high dislocation density indicating to a highly non-equilibrium state of metal during decomposition of solid solution is also favourable for subsequent processes of redistribution of crystalline lattice defects, which shows up in formation of blocks, cells and subgrains, i.e. refining of sub- and grained structure.

Moreover, active re-distribution of the crystalline lattice defects is accompanied, as a rule, by re-distribution of chemical elements and even fine phases, which, in turn, enhances the processes of phase formation in metal. The phase formations of certain sizes may strengthen sub- and intergranular boundaries, which is also favourable for refining of structure.

Judging from the character of different types of forming dislocation configurations and smearing of phase contrast in locations of phase precipitates, it can be concluded that active changes in the dislocation structure of the boundaries, as well as composition and distribution of phase precipitates along these boundaries take place within the zone of intergranular boundaries. Li-containing phases, such as the δ′-phase (Al_3Li), remain at the boundaries. However, they are less in quantity, compared with metal containing no scandium (see Figure 2).

CONCLUSIONS

1. Size and composition of coarse phase formations hardly change during the heat treatment process, compared with those in the as-welded metal with or without scandium. Such phase precipitates are complex conglomerates based on the Al–Cu phase.

2. Individual binary phases of the Al–Sc type, differing in size, i.e. coarse, located along the grain boundaries, and finer, formed in the bulk of grains and within the boundary zones, normally free from precipitates, are fixed, thus compensating for the negative effect of PFZ.

3. Heat treatment was found to lead to a large increase in density of distribution of phases: fine ($d \sim 0.10$–0.15 μm) and ultra fine ($d \sim 0.05$–0.10 μm) phases differing in morphology (lamellar type phases based on Al_2Cu, and globular phases based on AlLi).

4. It is shown that phase composition of the forming precipitates is determined in many respects by the presence or absence of scandium: the lamellar type phases (Al–Cu) in metal containing no scandium additions are transformed into complex structures, differing in copper concentration; the globular type phases (Al--Li) become more complex due to inclusions of fine phases (Al–Zr and Al–Cu); and complex composite phase precipitates of the lamellar (Al–Cu / Al_3Sc) and globular (Al–Li / Al–Zr, Al–Sc) types are formed in the Sc-containing metal.

1. Gilman, D.G. (1972) *Strength and plasticity physics*. Ed. by L.K. Gordienko. Moscow: Metallurgiya.
2. Argon Ali, S. (1972) *Strength and plasticity physics*. Ed. by L.K. Gordienko. Moscow: Metallurgiya.
3. Furukawa, M., Berbon, P., Horita, Z. et al. (1997) Production of ultrafine-grained metallic materials using an intense plastic straining technique. *Materials Sci. Forum*, **233 / 234**, 177–184.
4. Tsenev, N.K., Valiev, R.Z., Obraztsov, O.V. et al. (1992) Mechanical properties of submicron grained Al–Li alloys. In: *Proc. of Int. Aluminium Conf*. (8–10 Oct., 1992, Germany).
5. Lowel, A.W. *Aluminium-scandium alloy*. Pat. 3 619 181 US. Int. Cl. CP. 75-138. Publ. 09.12.71.
6. Furukawa, M., Miura, Y., Nemoto, M. (1987) Temperature and strain rate dependences of yield stress of an Al–Cu–Li–Mg–Zr alloy. *Transact. of Jap. Inst. Metals*, **28**, 655–665.
7. Gufnghui, M., Huasyun, Yu., Delin, P. et al. (2000) Fraction and phase spacing of fibrous intermetallic S–Li–Al in hypoeutectic Al-–Li alloys by unidirectional solidification. *Metallofizika. Nov. Tekhnologii*, 22(**4**), 58–61.
8. Volkov, V.A. (1987) *Effect of alloying elements on processes of decomposition of Al–Li and Al--Sc alloys*. Syn. of Thesis for Cand. of Phys.-Math. Sci. Degree. Kiev.
9. Berezina, F.L., Volkov, V.A., Domashnikova, B.P. et al. (1987) Some peculiarities of decomposition of supersaturated hard Al–Sc system alloys. *Metallofizika*, 9(**5**), 43–45.
10. Gayle, F.W., Vander Sande, J.B. (1984) Composite precipitates in an Al–Li–Zr alloy. *Scripta Metallic Mater*., **18**, 473–478.
11. Seiichi, A., Michinori, O. (1992) Weldability of high-strength aluminium alloys in EBW. *Keikinzoku Yosetsu*, 30(**1**), 12–18.
12. Markashova, L.I., Grigorenko, G.M., Ishchenko, A.Ya. et al. (2006) Effect of scandium additions on structure-phase condition of weld metal produced by welding aluminium alloy 1460. *The Paton Welding J*., **1**, 16–23.
13. Markashova, L.I., Grigorenko, G.M., Ishchenko, A.Ya. et al. (2006) Effect of scandium additions on fine structure of weld metal in aluminium alloy 1460 welded joints. *Ibid*., **2**, 20--25.
14. Darovsky, Yu.F., Markashova, L.I., Abramov, N.P. et al. (1985) Preparation method for electron-microscopic examinations. *Avtomatich. Svarka*, **12**, 60.

TEMPERATURE AND GEOMETRICAL DIMENSIONS OF WELD POOL IN PLASMA-POWDER SURFACING

P.V. GLADKY[1], **A.V. PAVLENKO**[2] and **E.F. PEREPLYOTCHIKOV**[1]
[1]E.O. Paton Electric Welding Institute, NASU, Kiev, Ukraine
[2]Deloro Stellite, GmbH, Germany

The paper presents the results of an experimental study of temperature, mass and dimensions of the weld pool and deposited layer in plasma-powder and argon-arc consumable electrode surfacing.

Keywords: plasma surfacing, filler powder, weld pool, pool temperature, pool shape and dimensions, plasma-powder surfacing, argon-arc surfacing

Knowledge of liquid metal pool heat state, shape and dimensions in argon-arc and plasma-powder surfacing enables to control formation of layers of desired dimensions, as well as structure and properties of the deposited metal.

Many publications [1–7] were devoted to the problems of study of heat state and geometrical dimensions in applying different welding and surfacing methods, however information characterizing the pool stage in plasma-powder surfacing with filler powder feeding into the arc, is insufficient. At the same time this process compares favorably with most of other processes of surfacing (welding) in that it enables to independently feed the powder into the weld pool, whose enthalpy and quantity can be varied within a wide range [8].

In this work a technique of forced splashing off of the pool metal into the calorimeter in the process of surfacing and a modernized setup [9, 10] for its implementation (Figure 1) to study pool dimensions and average temperature, is used. In running the experiment platform *5* with specimen *3* is tentatively set in the working (horizontal) position. Surfacing is effected from the center to the edge of the specimen. After depositing a bead of a certain length, the platform with the specimen is released from the lock *8* mounted on frame *1*, and under the effect of the spring *7*, with high speed turns around its axis and hits a fixed stop *6*. During platform turn and partially at the hit moment, liquid metal of the pool under the influence of inertia forces splashes out and gets into calorimeter *2*. The arc is extinguished as the platform turns, while plasmatron *4* remains stationary. The time for pool metal transfer from the plate into the calorimeter is 0.08–0.13 s.

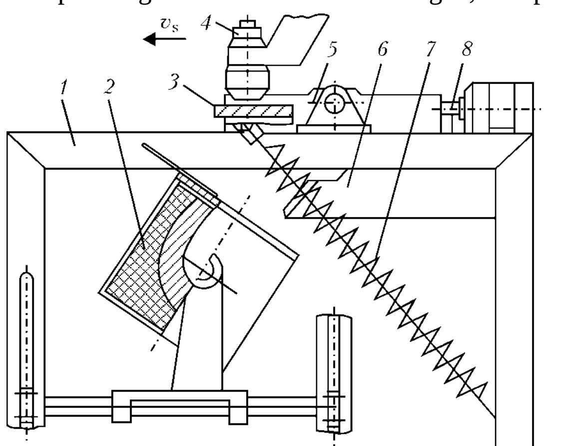

Figure 1. Diagram of the outfit for studying dimensions and average temperature of the weld pool (see the text for designations)

Setup measuring system, method of evaluation of enthalpy and average pool metal temperature are similar to those used in calorimetric studies of filler powder in [8]. Dimensions of the weld pool were evaluated from the crater formed as a result of metal splash-out. In so doing not all the metal gets into the calorimeter, some of it remains on the specimen surface as a roll. With regard for the heat content of the roll, average weld pool temperature is

$$T_{pool} = \frac{m_c T_c + m_r T_r}{m_c + m_r}, \qquad (1)$$

where m_r, T_r, m_c, T_c are the mass and temperature of the roll and metal getting into the calorimeter, respectively.

Temperature of the roll was estimated for each experiment run on the basis of the following assumptions. If the roll on the crater walls is very small, its temperature is close to the melting temperature. On the other hand, if all weld pool metal had remained on the specimen (in the roll), the roll temperature could have been equal to pool temperature. Dependence of roll temperature on its mass is assumed to be linear one:

$$\frac{T_r}{T_{melt}} = \left(\frac{T_{pool}}{T_{melt}} - 1\right)\frac{m_r}{m_{pool}} + 1, \qquad (2)$$

where m_{pool} is the weld pool mass, which can be approximately defined as

$$m_{pool} = m_c + m_r. \qquad (3)$$

In calculating the error in the measurement of enthalpy and average pool temperature, heat losses due to convection and radiation during transfer of metal into the calorimeter were taken into account; heat

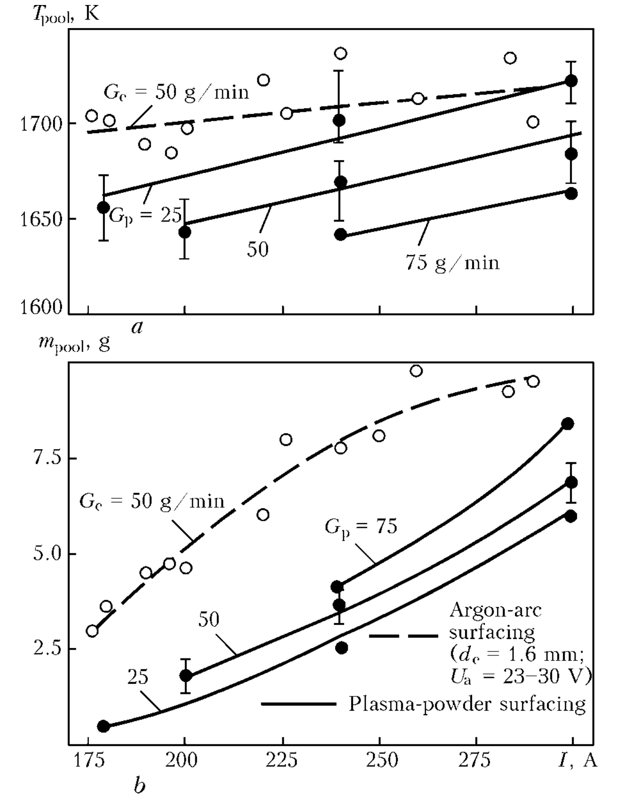

Figure 2. Average pool temperature (*a*) and mass (*b*) in plasma-powder and argon-arc consumable electrode surfacing

transfer from the pool into the base metal during turn of the platform with the specimen; heat accumulated in the pool metal layer remaining on the crater walls; amount of heat not measured with calorimeter because of the heating of the latter during the experiment. Heat losses because of the convection and radiation evaluated by method of [9] were 2.1 and 1.7 J / g, respectively. Amount of heat transferred by the liquid pool to the base metal during turn of the platform with specimen, calculated by heat conductivity Fourier equation, equals 5.7 J / g. Accounting of the heat accumulated in the layer of nonsplashed-out pool metal, reduces the value of specific heat content of the pool metal by 4 J / g. Amount of heat not measured by calorimeter because of the increasing temperature of the latter during the experiment was on the average

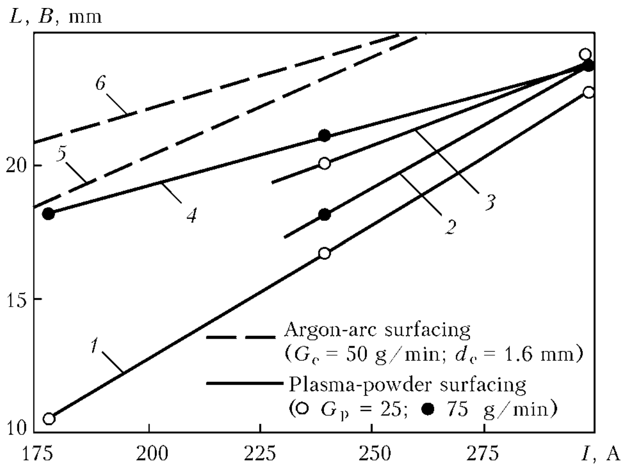

Figure 3. Effect of current on weld pool length *L* (*1, 2, 6*) and width of deposited bead *B* (*3–5*)

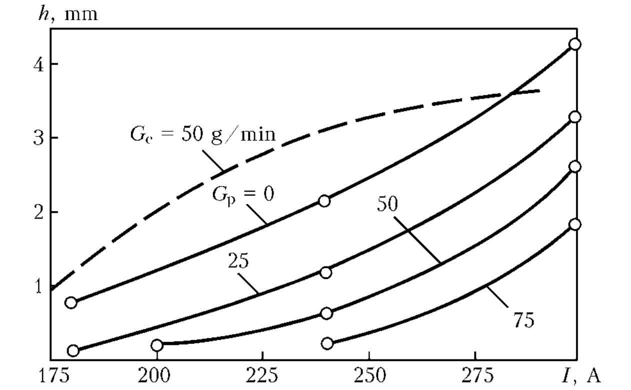

Figure 4. Dependence of depth of penetration of base metal on surfacing current in plasma-powder (solid line) and argon-arc consumable electrode (dashed line) surfacing

0.2 J / g. Average pool temperature measurement error was ± 24 K, that of weld pool mass ± 0.4 g.

Analyzed were also influence of arc current I, powder consumption in plasma surfacing G_p, consumption of electrode wire in argon-arc surfacing G_e, powder granulation d_p, rate of surfacing v_s, sway A and frequency of oscillations f of plasmatron on average temperature of pool metal T_{pool}, mass m_{pool} and length L of weld pool, width of deposited bead B, penetration depth h and area F, height of deposited bead H, area of weld pool surface F_{surf} (view in plan).

In order to exclude the effect of mixing of base and filler materials in surfacing on properties of liquid pool metal, base metal and additive powder of close chemical compositions were used, those corresponding to steel 10Kh18N10T.

Analysis of the measurement results shows that dimensions, mass and average pool temperature in plasma surfacing with filler powder are markedly lower than in the case of argon-arc surfacing with consumable electrode (Figures 2–4). Since comparison was carried out based on comparable conditions (in

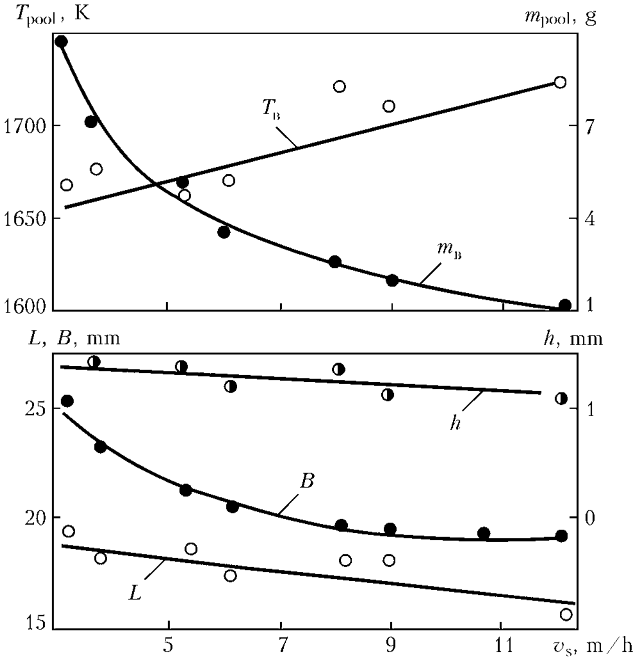

Figure 5. Effect of plasma-powder surfacing speed on characteristics of weld pool and base metal

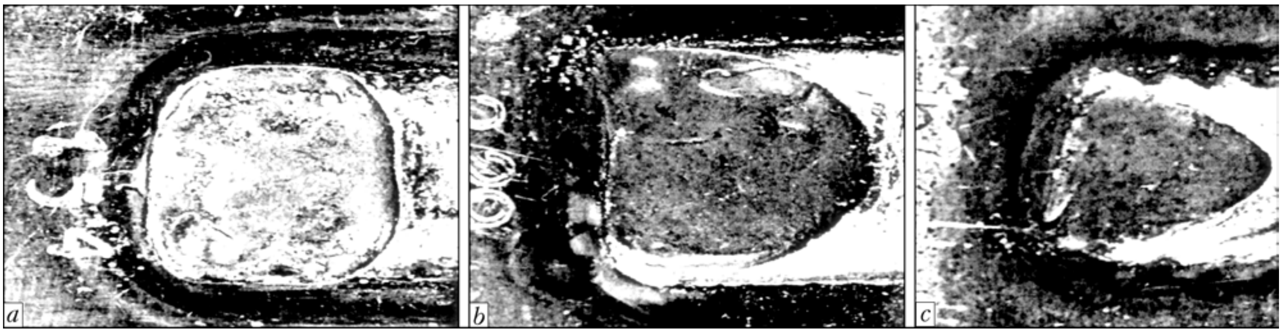

Figure 6. Pool shape at different speeds of plasma-powder surfacing: *a* — 3.8; *b* — 6.1; *c* — 12.1 m / h

terms of arc power and rate of feed of the filler material), the difference observed to a great extent is linked with heat state of the filler material getting into the weld pool.

In plasma surfacing with growing current (meaning also growing effective heat efficiency of the arc), weld pool, its heat content and average temperature increase.

With growing speed of transposition of the plasmatron, which is equivalent to the reduction of heat input, average weld pool temperature increases, and its mass and dimensions decrease (mainly due to its tail part) (Figures 5 and 6). With increasing amplitude of transverse oscillations of the plasmatron, average pool temperature remains practically unchanged, width of the bead sharply increases, with the same rate pool length decreases (Figure 7), while area of pool surface and depth of penetration of the base metal undergo small changes. Increase of oscillation frequency of the plasmatron causes intensified mixing of the liquid metal, and, as a result, growth of weld pool convective heat emission. With increasing frequency its temperature decreases a bit, depth of penetration of the base metal also decreases, other parameters remain almost unchanged.

Increased consumption of additive powder influences various parameters of the pool in an ambiguous way (Figures 4 and 8) — pool mass in so doing grows, its length and width remain practically unchanged, penetration depth and average weld pool temperature decrease.

Overall heat content of liquid metal pool increases as a result of more efficient use of the arc heat input.

Figure 9 shows dependence of pool temperature and dimensions on filler powder granulometric composition. With increasing average particle diameter average pool temperature decreases. Pool mass decreases slightly, whereas penetration depth of the base metal decreases significantly. The obtained results are unequivocally connected with decreased heating of the powder in the arc.

On the whole in the investigated range of parameters of surfacing 10Kh18N10T steel with powder, a comparatively small change of average weld pool temperature within 1640–1770 K range is established, which accounts for approximately $(1.01–1.08)T_{melt}$ of the filler powder or on the average $1.05T_{melt}$.

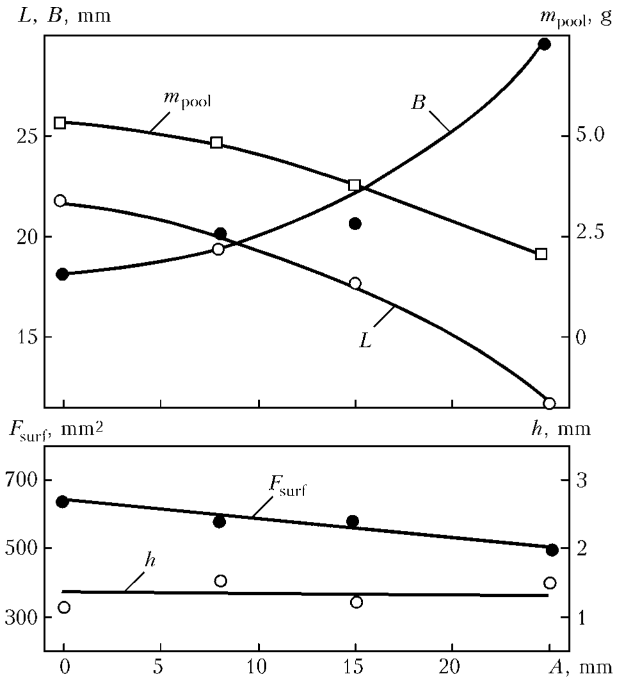

Figure 7. Effect of amplitude of oscillations of plasmatron *A* on properties of weld pool and base metal

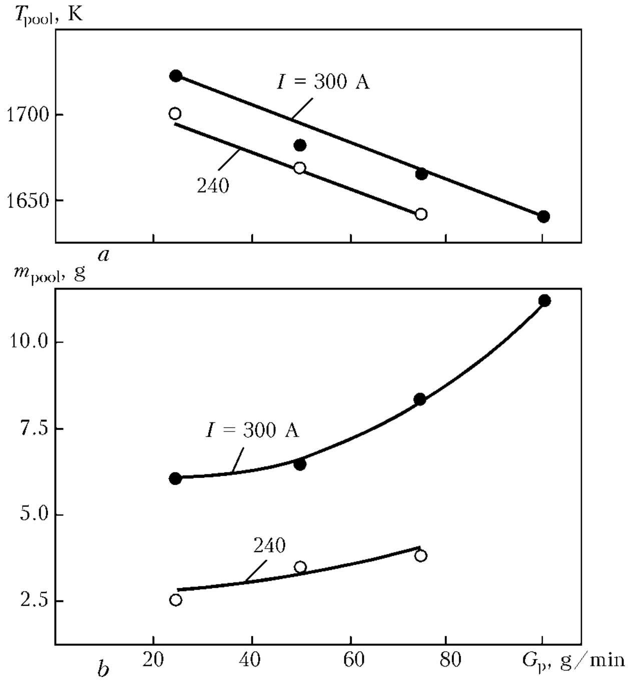

Figure 8. Average pool temperature (*a*) and mass (*b*) at different deposition rates and currents in plasma surfacing

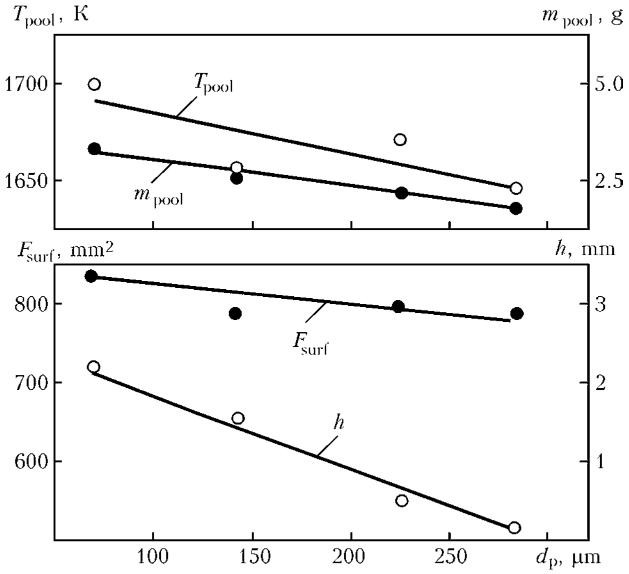

Figure 9. Effect of granulation of filler powder on weld pool and base metal characteristics

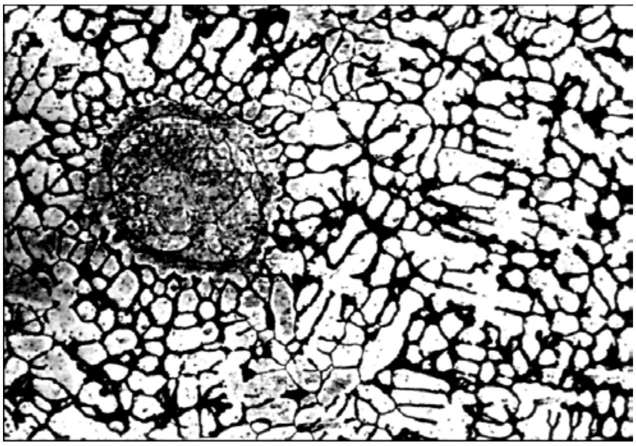

Figure 10. Microstructure of metal deposited with 10Kh18N10T powder (large unmelted powder particle is seen) (×250)

In comparing the results of previous studies of heating powder in arc [8, 11] and findings of this study, correlation of heat state of the additive powder and the pool parameters was established. Diminishing temperature of additive powder particles, as well as intensified feeding into the pool of powder heated to temperature lower than that of the pool, lead to decreased overheating of liquid metal and reduction of penetration of the base metal. Thus, capability to control heating of powder in plasma surfacing creates prerequisites for controlling shape and dimensions of the pool and solidification of the layer being deposited.

As shown above, the main trait of plasma-powder surfacing is feeding into the weld pool of filler powdered metal with particle diameter 80--300 μm. Small fractions flying through the plasma arc, get melted, while larger ones have time enough to get heated up to several hundred degrees and get into the weld pool in solid state. In the head section of the pool under the effect of plasma arc they get melted, but in the tail one they accelerate cooling, acting as microcoolers. In such a case a subcooling of the pool is observed — its average temperature decreases, and, which is rather important, also depth of penetration of the base metal. Unmelted large particles can become additional solidification centers. In practice unmelted particles of the additive metal are observed very rarely in the crystallized layer (Figure 10).

The degree of effect of particles of the filler material on the microstructure of the deposited metal must depend on the size (mass) of the particles, their shape and heating temperature, as well as on the fraction of large particles in the powder. Influence of the latter is similar to the effect of additive filler in the form of grit or granules fed into the weld pool during submerged-arc welding and some other processes [12, 13].

Formation of additional solidification centers makes the structure finer and imparts it a disoriented character, which can contribute to improvement of operational properties of the deposited metal.

CONCLUSIONS

1. Average weld pool temperature depends on arc current, speed of surfacing, size of particles and rate of feeding of filler powder. With accuracy adequate for calculations it can on the average be assumed equal to $1.05T_{melt}$ of that of the powder.

2. Values of main geometrical and thermal parameters of liquid metal pool in plasma surfacing with feeding of filler powder are significantly lower than similar values characterizing molten pool in argon-arc surfacing with a consumable electrode.

3. Depth of penetration of the base metal mainly depends on arc current, particle size and consumption of filler powder. Lesser compared to other methods penetration of base metal is due to the cooling of the head section of the pool with the powder melting in it.

1. Frumin, I.I., Pokhodnya, I.K. (1955) Study of weld pool mean temperature. *Avtomatich. Svarka*, **4**, 13--30.
2. Kopersak, N.I., Slivinsky, A.M., Dukhno, V.M. et al. (1973) Temperature condition of weld pool. *Ibid*., **7**, 1–3.
3. Kopersak, N.I., Slivinsky, A.M., Dukhno, V.M. et al. (1974) Effect of metal preheating on weld pool temperature. *Ibid*., **11**, 9--11.
4. Erokhin, A.A. (1982) Temperature field of molten metal pool in arc heating. *Svarochn. Proizvodstvo*, **2**, 16–17.
5. Dobrovolsky, I.P. (1982) Pool temperature field in arc heating. *Fizika i Khimiya Obrab. Materialov*, **5**, 49–52.
6. Dmitrik, V.V. (1999) Development of method for determination of temperature condition of molten pool metal. *Izvestiya Vuzov. Mashinostroenie*, **1**, 76–80.
7. Razmyshlyaev, A.D. (1999) Estimation of convection effect of molten metal on weld pool sizes in arc surfacing. *Avtomatich. Svarka*, **8**, 22--24.
8. Pavlenko, A.V., Gladky, P.V. (1990) Peculiarities of filler powder heating in plasma surfacing. *Ibid*., **1**, 33–37.
9. Dukhno, V.M., Slivinsky, A.M., Getmanets, S.M. et al. (1975) Experimental investigation of weld pool temperature condition. *Vestnik KPI. Series Mashinostroenie*, **12**, 107–109.
10. Dukhno, V.M., Slivinsky, A.M., Kotik, V.T. et al. *Device for determination of mean temperature in weld pool metal*. USSR author's cert. 472263. Int. Cl. G 01 K 7 / 02. Fill. 04.06.73.
11. Gladky, P.V., Pavlenko, A.V., Zelnichenko, A.T. (1989) Mathematical modeling of powder heating in arc during plasma surfacing. *Avtomatich. Svarka*, **11**, 17–21, 54.
12. Ivochkin, I.I. (1965) Suppression of columnar crystal growth by weld pool «freering» method. *Svarochn. Proizvodstvo*, **12**, 1–3.
13. Ivochkin, I.I., Malyshev, B.D. (1981) *Submerged-arc welding with additional filler metal*. Moscow: Strojizdat.

EVALUATION OF CRACK RESISTANCE OF WELDED JOINT METAL BASED ON THE RESULTS OF STANDARD MECHANICAL TESTS WITH REGARD FOR THE DIMENSIONS OF STUCTURAL ELEMENTS

V.S. GIRENKO, M.D. RABKINA and **S.V. GIRENKO**
E.O. Paton Electric Welding Institute, NASU, Kiev, Ukraine

An evaluation of static crack resistance (K_{1c}, δ_{1c}) of structural steels and their welded joints is proposed, based on standard mechanical testing and impact toughness of Charpy samples, allowing for the dimensions of structural elements. The developed approach allows for the difference in the deformation gradients in the tip of a crack-like defect and notch of a Charpy sample, which results in that the structural parameters, responsible for fracture initiation, are under different loading conditions depending on their dimensions.

Keywords: crack resistance, structural steels, welded joints, impact toughness, tough fracture, critical deformation, structural elements

Structural fracture mechanics consists of two lines of investigation:

• immediate determination of criteria of crack resistance based on the results of standard tests for impact toughness of Charpy samples, using other mechanical and metallophysical values [1--3];

• methods of evaluating fracture toughness based on the so-called master curve [4].

The first approach is used in evaluating crack resistance in conditions of plane deformation K_{1c}, δ_{1c}. In practice such conditions, with some restrictions, appear in development of surface or internal defects propagating deeper into structural elements. It has to be noted that for many structures, containing toxic and explosive substances the main limiting state, irrespective of subsequent fracture peculiarities, is depressurization. The other approach, beside simplification of testing methods, includes evaluation of fracture toughness with propagation of through cracks in structural elements of different thicknesses. It is sound practice to apply both approaches, since they complement each other. This work is dedicated to the development of the former one.

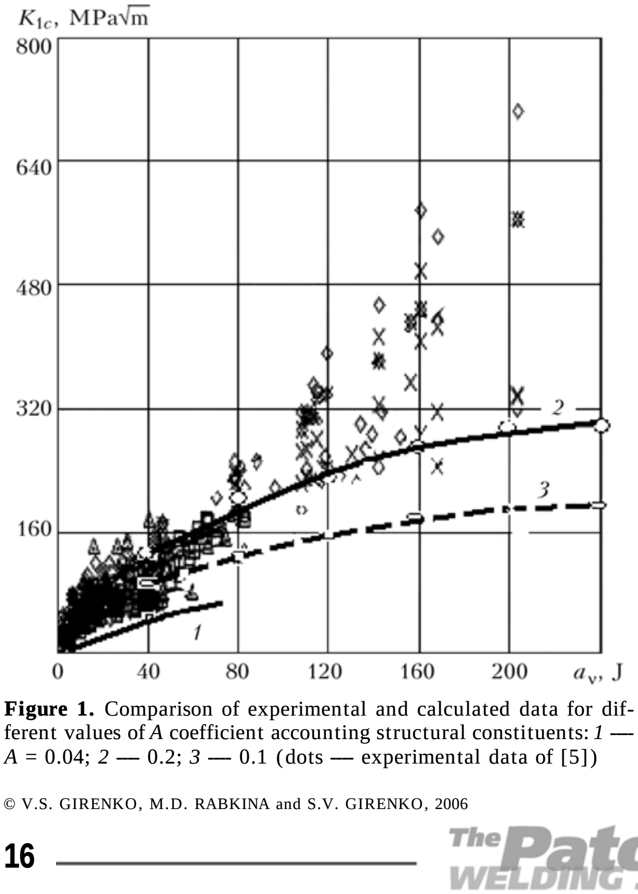

Figure 1. Comparison of experimental and calculated data for different values of A coefficient accounting structural constituents: *1* — A = 0.04; *2* — 0.2; *3* — 0.1 (dots — experimental data of [5])

In [1, 2] empirical dependences between values of fracture mechanics and impact toughness were considered. Detailed verification of these dependences (Figure 1, curve *3*) has proved their regularity, but has again stressed the observance of a big scatter of experimental data, which can be due to the following reasons:

• disturbance of plane deformation state, which, in its turn, is typical for high degrees of fracture toughness (see Figure 1);

• absence of distinct criteria in the notion of initiation of tough fracture, which includes many stages, beginning with formation of micropores and ending up with expansion of the main rupture;

• not quite adequate cutting out of Charpy samples with respect to full-scale samples used for immediate determination of K_{1c} value;

• contradiction arising as a result of applying methods of continuous medium mechanics in analyzing actual structural materials having various peculiarities in their structure.

This work represents an effort of an approximated analysis of the influence of the dimensions of structural elements on the determination of K_{1c} value based on the results of standard mechanical tests. Brief analysis of the problem in question was made in [6]; its prerequisites were described in [7, 8]. With some dimensions of structural elements abnormal discrepancy between impact toughness and K_{1c} value is observed. Such an abnormality, in the opinion of the authors of [6], is due to difference in gradients of stresses and strains at the tip of crack-like defect and the notch in Charpy sample. Accordingly, structural parameters responsible for fracture initiation depending on their dimensions, experience different loading conditions.

Initially analysis of relation between crack resistance and the work of fracture of Charpy samples was applied to static loading and ductile state of the material. Under such conditions fracture initiation is usually connected with critical value ε_f of local plastic deformations: $\varepsilon = \varepsilon_f$. Value ε_f determines conditions for fracture initiation both at the tip of the crack-like defect, and at the tip of the notch on Charpy sample, since for deformation criteria of tough fracture, weak dependence not only on the degree of voluminosity of the stress state, but also on the rate of loading is typical. It enables to relate crack resistance value δ_{1c} to bending angle of Charpy sample θ (corresponding to the beginning of tough fracture), and, consequently, to specific work of crack initiation a_{v}^{3}.

Using Neuber relation, according to which product of the coefficients of concentration of stresses and deformations in the non-linear domain equals square of the coefficient of elastic stresses ($K_\sigma K_\varepsilon = K_e^2$) , and, considering that for Charpy sample $K_e = 3.44$, one can write:

$$\frac{\sigma^{\max}}{\overline{\sigma}}\,\frac{\varepsilon^{\max}}{\overline{\varepsilon}} = 11.82, \tag{1}$$

where $\sigma^{\max}$ and $\varepsilon^{\max}$ are the local, and $\overline{\sigma}$ and $\overline{\varepsilon}$ are the average stresses and deformations.

In plane deformation true shift $\gamma = 1{,}5\varepsilon$ and, respectively for the material being hardened by the exponential law, the following relation is observed:

$$\sigma = \sigma_{\text{y}}\left(\frac{\varepsilon}{\varepsilon_{\text{y}}}\right)^{n} = \sigma_{\text{y}}\left(\frac{\gamma}{1.5\varepsilon_{\text{y}}}\right)^{n}, \tag{2}$$

where n is the coefficient of work hardening.

In bending of Charpy sample average shear deformation along each of the slip band is $\gamma \approx \theta / 2$, where θ is the bending angle. Therefore the dependence has the following form:

$$\left(\frac{\varepsilon^{\max}}{\varepsilon_{\text{y}}}\right)^{1+n} = 11.82\left(\frac{\theta}{2\cdot 1.5\varepsilon_{\text{y}}}\right)^{1+n}. \tag{3}$$

Taking into account that distribution of elastic stresses at some distance r from the tip of the notch having finite rounding radius ρ_0 is expressed by approximate dependence [9]

$$\sigma_{YY} = \sigma K_e\sqrt{\frac{\rho_0}{\rho_0 + 4r}}, \tag{4}$$

one can write the expression for determining plastic deformations ε at distance r from the tip of the notch in Charpy sample:

$$\left(\frac{\varepsilon}{\varepsilon_{\text{y}}}\right)^{1+n} = 11.82\,\frac{1}{1 + 4\,\dfrac{r}{\rho_0}}\left(\frac{\theta}{3\varepsilon_{\text{y}}}\right)^{1+n}. \tag{5}$$

From expression (5) bending angle of Charpy sample is determined, which accounts to the initiation of tough fracture. Usually dimensions of a structural element in analyzing conditions of fracture are considered in the following way: distance r from the tip of the crack to the point of stress or deformation determination, is assumed to be equal to specific size r^*. With regard for this, connection between critical bending angle of Charpy sample θ_c, corresponding to the initiation of tough fracture and critical value of local plastic deformations is expressed as

$$\left(\frac{\varepsilon_f}{\varepsilon_{\text{y}}}\right)^{1+n} = 11.82\,\frac{1}{1 + 4\dfrac{r^*}{\rho_0}}\left(\frac{\theta_c}{3\varepsilon_{\text{y}}}\right)^{1+n}. \tag{6}$$

Stresses and deformations within plastic zone near the tip of crack-like defect is described as follows:

$$\sigma = \sigma_{\text{y}}\left(\frac{R}{r}\right)^{\frac{n}{1+n}}, \quad \varepsilon = \varepsilon_{\text{y}}\left(\frac{R}{r}\right)^{\frac{1}{1+n}}, \tag{7}$$

where R is the size of the plastic zone.

Considering that with advanced plastic deformations under conditions of plane deformation state $\delta_1 \approx$ $\approx 2R\varepsilon_{\text{y}}$, it follows that

$$\left(\frac{\varepsilon}{\varepsilon_{\text{y}}}\right)^{1+n} = \frac{\delta_1}{2\varepsilon_{\text{y}} r}. \tag{8}$$

Considering critical values of deformations and dislocations, we obtain the following dependence:

$$\left(\frac{\varepsilon_f}{\varepsilon_{\text{y}}}\right)^{1+n} = \frac{\delta_{1c}^{\max}}{2\varepsilon_{\text{y}} r^*}, \tag{9}$$

where $\delta_{1c}^{\max}$ is the critical opening of crack tip at the moment of initiation of tough fracture.

Expression (9) represented as

$$\delta_{1c}^{\max} = 2r^*\varepsilon_{\text{y}}\left(\frac{\varepsilon_f}{\varepsilon_{\text{y}}}\right)^{1+n} \tag{10}$$

reveals physical meaning of value $\delta_{1c}^{\max}$ in tough fracture — limiting elongation of a double-length structural element, which under otherwise equal conditions is the greater, the greater is the work hardening of the material.

Uniting expressions (6) and (10) we obtain the following dependence between critical bending angle of Charpy sample θ_c and strain value of crack resistance $\delta_{1c}^{\max}$:

$$\delta_{1c}^{\max} = 11.82\varepsilon_{\text{y}}\left(\frac{2r^*}{1 + \dfrac{4}{\rho_0}\,r^*}\right)\left(\frac{\theta_c}{3\varepsilon_{\text{y}}}\right)^{1+n} = 23.64\varepsilon_{\text{y}}\beta\left(\frac{\theta_c}{3\varepsilon_{\text{y}}}\right)^{1+n}. \tag{11}$$

Designating structural parameter as $r^* / \left(1 + \dfrac{4}{\rho_0}\,r^*\right) = \beta$, and with regard for that for Charpy samples $\rho = 0.25$, it is possible to directly establish connection between $\delta_{1c}^{\max}$ and specific work of tough crack initiation in a Charpy sample a_{v}^{3}.

In the absence with the material of pronounced work hardening ($n \to 0$),

$$a_v^3 = \frac{M_{w.y}\theta_c}{t(B-l)} = \frac{B-l}{4} 1.25\sigma_y\theta_c, \quad (12)$$

where l is the notch depth; $(B - l)$ is the size of the weakened section; t is the sample thickness; $M_{w.y}$ is the bending moment at overall yielding of the weakened section.

To make allowance for the influence of work hardening, which can be substantial with steels of low and medium strength, it is necessary to assume yield stress depending on the bending angle of Charpy sample:

$$M_{w.y}(\theta) = \frac{t(B-l)^2}{4} 1.25\sigma_y \left(\frac{\theta}{3\varepsilon_y}\right)^n. \quad (13)$$

In so doing specific work of initiation of a tough crack at $(B - l) = 8$ mm is

$$a_v^{\varsigma} = \frac{1}{t(B-l)} \int_0^{\theta_c} M_{w.y}(\theta) d\theta = \quad (14)$$

$$= (B-l)1.25 \frac{\sigma_y}{4} \int_0^{\theta_c} \left(\frac{\theta}{2 \cdot 1.5\varepsilon_y}\right)^n d\theta = 7.5 \frac{\sigma_y\varepsilon_y}{(1+n)} \left(\frac{\theta_c}{3\varepsilon_y}\right)^{1+n}.$$

Uniting expressions (11) and (14), we obtain the following dependence (without account of work hardening):

$$\delta_{1c}^{max} \cong 3\beta \frac{a_v^{\varsigma}}{\sigma_y}, \quad (15)$$

with account of work hardening

$$\delta_{1c}^{max} \cong 3(1+n)\beta \frac{a_v^{\varsigma}}{\sigma_y}. \quad (16)$$

Consider dependence between specific work of propagation of a tough crack in the Charpy sample a_v^{pr} and strain value of crack resistance δ_{1c}^{max}. As a criterion of material resistance to the development of a tough crack, critical angle of crack opening can be used. The fact that the angle is practically constant with crack growth substantially eases the analysis.

With three-point bend connection between opening of tip of stationary crack δ_1, sagging of sample V and turning angle θ is determined by the following geometrical relationships:

$$\frac{\theta}{2} = \frac{V}{l_0} = \frac{\delta_1}{2r_0}, \quad (17)$$

where r_0 is the distance from the crack tip to the turning center; l_0 is the distance to the support.

Imagine that some small growth of the crack by value Δl has taken place. Let us designate opening of the crack in point corresponding to the initial position of its tip due to its growth as $\delta_1^{\Delta l}$. Accordingly

$$\frac{\theta^{\Delta l}}{2} \cong \frac{V^{\Delta l}}{l_0} \cong \frac{\delta_1^{\Delta l}}{2r_0^{\Delta l}}. \quad (18)$$

Using the results obtained before [10], one can write:

$$\frac{\theta^{\Delta l}}{2} \cong \frac{V^{\Delta l}}{l_0} \cong \frac{\Delta l \frac{\sigma_t}{\sigma_y} \frac{n}{(1-n)^2}}{2r_0^{\Delta l}}. \quad (19)$$

Coming now from the bent sample with crack to notched Charpy sample, it has to be noted that initial stages of fracture development proceeding from the notch and the crack, can have some differences, but further on the processes become identical. It enables to apply dependences similar to the previous one, to analyze development of tough fracture in Charpy sample.

Value $r_0^{\Delta l}$ can be evaluated based on the results of numerical analysis of [11]: with changing ratio of the crack length (including notch length) to the sample width from 0.3 to 0.8, its value varies from $0.45(B - l)$ to $0.43(B - l)$. Coefficient of constraint of plastic deformations varies within a wider range $L = 1.23$–1.29; $L_{av} = 1.26$ [11]. For simplicity one can assume that turning center is located in the middle of the h wide section, weakened by growing crack. Dependence (19) for infinitely small value of θ can be represented as

$$d\theta = 2 \frac{\sigma_t}{\sigma_y} \frac{n}{(1-n)^2 h} dh. \quad (20)$$

Based on the detailed analysis one can consider that maximum loading at the stage of fracture propagation is determined by weakening of the section and work hardening of the material reached by the moment of tough crack initiation. Bending moment in tough crack initiation, when sample bending angle θ assumes the θ_c value, can be determined in the following way:

$$M^{max}(\theta_c) = \frac{t(B-l)^2}{4} 1.26\sigma_y \left(\frac{\theta_c}{3\varepsilon}\right)^n. \quad (21)$$

Accordingly maximum bending moment performing work in tough crack initiation, is equal

$$M_p^{max}(h) = 1.26\sigma_y \left(\frac{\theta_c}{3\varepsilon_y}\right)^n \frac{th^2}{4}. \quad (22)$$

With regard for expressions (19) and (22) specific work of propagation of tough crack in a Charpy sample can be determined:

$$a_v^{pr} = \frac{1}{t(B-l)} \int_0^{\theta_c} M(\theta) d\theta =$$

$$= \frac{2\frac{\sigma_t}{\sigma_y} \frac{n}{1-n^2}}{t(B-l)} \int_0^{B-l} \frac{M_p^{max}(h)}{h} dh = \quad (23)$$

$$= \frac{\sigma_t}{\sigma_y} \frac{n}{(1-n)^2} 1.26\sigma_y \left(\frac{\theta_c}{3\varepsilon_y}\right)^n \frac{B-l}{4}.$$

Uniting (11) and (23), one can write

$$\delta_{1c}^{max} = 9.4\varepsilon_y\beta \frac{(1-n)^2}{n} \left(\frac{\theta_c}{3\varepsilon_y}\right) \frac{a_v^{pr}}{\sigma_t}. \quad (24)$$

Taking into account that bending angle θ_c is reached at loading close to the maximum one, when average yield stresses near tensile strength of material, and true deformations are $\varepsilon \approx \frac{n}{1-n}$, one can consider that

$$\frac{\theta_c}{3\varepsilon_y} \cong \frac{\gamma}{1.5\varepsilon_y} \cong \frac{\varepsilon_e}{\varepsilon_y} \cong \frac{n}{(1-n)\varepsilon_y}. \quad (25)$$

Then connection between crack resistance value σ_{1c}^{max} and specific work of tough crack propagation in Charpy sample can be expressed as

$$\delta_{1c}^{max} = 9.4\beta(1-n)\,\frac{a_v^{pr}}{\sigma_t}. \quad (26)$$

Without regard for the work hardening, dependence (26) assumes the following form:

$$\delta_{1c}^{max} = 9.4\beta\,\frac{a_v^{pr}}{\sigma_t}. \quad (27)$$

The results obtained enable to come to the final stage of analysis. Applied to materials with weak work hardening, connection between specific work of fracture at the «upper shelf» a_v^{max} and crack resistance value δ_{1c}^{max} with regard for expressions (15) and (27) has the following form:

$$\delta_{1c}^{max} = 2.3\beta\,\frac{a_v^{(s)}}{\sigma_y}. \quad (28)$$

Disregarding the influence of parameter n on final results (since this value is not rate-set in engineering practice, and its influence is negligible), the result can be written as:

$$\delta_{1c}^{max} \cong 3\,\frac{\beta}{\left(1+0.33\,\frac{\sigma_t}{\sigma_y}\right)}\,\frac{a_v^{max(s)}}{\sigma_y}. \quad (29)$$

The above analysis was conducted as applied to static loading, which in dependences (28) and (29) is stressed through assigning to value a_v^{max} of symbol s. It was assumed that all basic physical-mechanical values contained in dependence (29) (δ_{1c}^{max}, σ_y, σ_t, $a_v^{max(s)}$) were obtained in the same conditions. Consequently, they should characterize metal properties under similar loading rates and, naturally, at temperatures providing fully tough fracture of both the sample with crack and the Charpy sample. Since criterion δ_{1c}^{max} is a value of static crack resistance of the material, values $a_v^{max(s)}$, σ_y and σ_t must also relate to static loading, which is reflected by index s. Such a requirement can be justified both from theoretical and engineering points of view in their relation to all mentioned mechanical values, but except for a_v^{max}. In determining the latter, impact loading is necessary, in the first place, for provision of state of plane deformation at all stages of deformation of Charpy sample. This does not play a decisive role in tough fracture, but is of principal importance for correct reproduction of conditions of ductile-brittle transition in plane-strained state. Besides, namely testing for impact toughness is a primary criterion in accepting materials for their employment.

In this way, in formula (29) it is necessary to retain static values of all mechanical properties, but except for $a_v^{max(s)}$ value, which must be corrected with regard for dynamic effects, in order to be able to apply it without substantial errors instead of impact toughness value.

Influence of the rate of loading growth on specific work of fracture of a Charpy sample can be characterized by coefficient D:

$$D = b\,\frac{a_v^{max(s)}}{a_v^{max(d)}}, \quad (30)$$

where $a_v^{max(s)}$ is the specific work of tough fracture of Charpy sample under static loading; $a_v^{max(d)}$ is the impact toughness obtained in testing Charpy sample in temperature range corresponding to «upper shelf»; b is the dimensionless proportionality coefficient.

Analysis of experimental data pertaining to steels with different work hardening properties shows that coefficient D is practically directly proportional to ratio σ_y / σ_t. Value b varies from 0.75 to 1. With regard for this, dependence (29) can be finally written down in the following form (with $b = 1$ and $\delta_{1c} = \frac{K_{1c}^2\,(1-\nu^2)}{2E\sigma_y}$):

$$\delta_{1c} = 3\,\frac{\beta\,\frac{\sigma_y}{\sigma_t}}{\left(1+0.33\,\frac{\sigma_t}{\sigma_y}\right)}\,\frac{a_v}{\sigma_y}, \quad (31)$$

$$K_{1c} = \sqrt{6\beta\,\frac{E}{1-\nu^2}\,\frac{1}{\left(1+0.33\,\frac{\sigma_t}{\sigma_y}\right)}\,\frac{\sigma_y}{\sigma_t}}\;a_v, \quad (32)$$

where $\beta = \frac{r^*}{1+\frac{4}{\rho_0}\,r^*}$.

Application of formulae derived using deformation criteria is possible not only within temperature range of the «upper shelf», but also at that of transition temperatures, where micro-ductile constituent is also present [11, 12]. Besides, such a possibility follows from the results of [1–3, 5, 6], since for most structural materials not having structural defects, stable correlation between values K_{1c}, δ_{1c} and impact toughness of Charpy samples is observed. It can consequently be stated that plastic deformations constriction in both cases is practically similar, and respectively, in testing for impact toughness, conditions of ductile-brittle transition, typical for plane-strained state in the crack zone under static loading, are reproduced.

The formulae obtained (31), (32) require some additional correction. Dependence (10) leads to the following result: with decreasing dimensions of structural elements r^* under otherwise equal conditions strain value of crack resistance δ_{1c} approaches zero, which contradicts physical sense. Taking into account the results of [13], it expedient to use the notion of effective crack sharpness. The point is that to form the most adverse deformation and stress fields near the crack tip, some blunting of it is required. Respectively, the seat of fracture is situated at some distance x from the defect tip, whereas fracture toughness at the «lower shelf» of its temperature dependence is

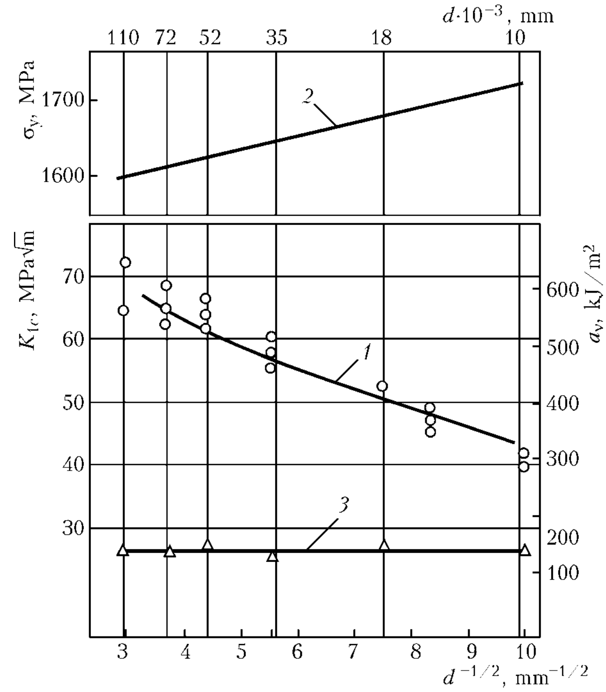

Figure 2. Comparison of experimental and calculated data on values K_{1c}, σ_y, a_v at different dimensions of structural elements: curve *1* — calculated K_{1c} values; *2, 3* — respectively experimental values of σ_y and a_v; circles — experimental K_{1c} values

limited to a certain level, which has to be taken into account in constructing mathematical models. In this connection it is expedient to assign the following form to the calculated structural parameter β:

$$\beta = \frac{x + r^*}{1 + \frac{4}{\rho_0} r^*}. \qquad (33)$$

For high-strength steels zone radius is $x \cong 0.01$ mm. For low-strength materials this value can be a bit higher (up to 0.05 mm).

To check the obtained results it is expedient to use experimental data of [6]. Their comparison with K_{1c} values calculated by the formulae (32) and (33) at $x = 0.01$ mm, is shown in Figure 2. One can see that the agreement of the results is quite satisfactory.

Consider potential role of structural peculiarities of the materials in scatter of experimental data shown in Figure 1. Taking into account unavailability of full information on physical-machanical properties of steels in [5], only formal limit boundaries of calculated values K_{1c} can be determined. For this purpose, it is expedient to represent dependence (32) in the following form:

$$K_{1c} = \sqrt{A \frac{E}{1 - \nu^2} a_v},$$

where

$$A = 6\left(\frac{x + r^*}{1 + 16r^*}\right)\left(\frac{\sigma_y/\sigma_t}{1 + 0.33\frac{\sigma_t}{\sigma_y}}\right); \quad x = 0.01 \text{ mm}.$$

Assuming minimum size of a structural element $r^* = 0.01$ mm, with maximum work hardening ($\sigma_y / \sigma_t = 0.6$) we obtain $A \approx 0.04$.

Evaluating the least conservative dependence K_{1c} on a_v, we assume $r^* = 0.1$ mm with ratio $\sigma_y / \sigma_t = 1$. Here $A \approx 0.2$. Empirical value of coefficient A in [1] equals 0.1–0.157.

Shown in Figure 1 approximate solution with minimum A value provides conservative evaluation for the whole range of scatter of experimental data. At the same time curve *2* describes upper boundary of this scatter in a satisfactory way. Data lying above this curve are explained by disturbance of plane deformation state in evaluating K_{1c} criterion.

Concluding this study, one can note that irrespective of a number of approximate assumptions, evaluation of the influence of greatness of structural parameters on the interrelation between crack resistance values K_{1c} and impact toughness of brittle high-strength steels appeared to be quite acceptable. Analysis of possible boundaries of scatter of experimental results also yields satisfactory results. It has to be stressed at the same time that when dealing with low-strength steels with high fracture toughness, the picture of initiation of both tough and quasi-brittle cracks must be different. In such cases fracture initiation in the field of maximum strains and stresses is due to cracking of a number of structural elements. Within the framework of the above analysis this changes the idea of not only the dimensions of a complex structural element, but also of *x* parameter. It is accordingly to be expected that more ductile structural elements much be less dependent on the dimensions of structural elements than as it follows from Figure 2. Such an assumption corresponds to existence of stable relations between K_{1c} and a_v for many relatively ductile structural materials. The above approach can be used in particular in technical diagnostics of welded structures.

1. Girenko, V.S., Dyadin, V.P. (1985) Relationships between impact toughness and fracture mechanics criteria δ_{1c} and K_{1c} of structural steels and their welded joints. *Avtomatich. Svarka*, **9**, 13–20.
2. Girenko, V.S., Dyadin, V.P. (1986) Relationships between impact toughness and fracture mechanics criteria δ_{1c} and K_{1c} of structural steels and their welded joints. *Ibid.*, **10**, 61–62.
3. Girenko, V.S. (1995) Some approaches to evaluation of static crack resistance of metallic materials and welded joints. *Ibid.*, **9**, 74–77.
4. *ASTM Standard Test Method E 1921--97*.
5. Phaal, R., Macdonald, K.A., Brown, P.A. (1993) Correlation between fracture toughness and Charpy impact energy. *TWI*, 5605(**71**).
6. Panasyuk, V.V., Romaniv, O.M. (2001) Charpy and fracture toughness data: limitations and advantages in evaluation of the embrittlement of metals. In: *Proc. of Charpy Centenary Conf. ESSIS* (Poitiers, Paris, Oct. 2–5, 2001). Vol. 2.
7. Romaniv, O.N., Kryskiv, A.S., Tkach, A.N. (1978) On some cases of different structural sensitivity to impact toughness and fracture toughness. *Fiziko-Khimich. Mekhanika Materialov*, **6**, 64–71.
8. Romaniv, O.N., Tkach, A.N., Gladky, Ya.N. et al. (1976) Application of overheating in quenching to increase the crack resistance of high-strength steels. *Ibid.*, **5**, 41–48.
9. Tettelman, A.S., McEvily, A.J. (1967) *Fracture of structural materials*. New York.
10. Girenko, V.S., Dyadin, V.P. (1990) Correlation of crack resistance characteristics of materials and welded joints with the results of standard mechanical tests. *Avtomatich. Svarka*, **6**, 1–4.
11. Shiratori, M., Miyoshi, T., Manushita, X. (1986) *Computational fracture mechanics*. Moscow: Mir.
12. Romaniv, O.N. (1981) Structural fracture mechanics as a new prospective tendency in problem of metal fracture. *Fiziko-Khimich. Mekhanika Materialov*, **100**, 28–44.
13. Malkin, J., Tetelman, A.S. (1971) Relation between K_{1c} and microscopic strength for low alloy steels. *Eng. Fracture Mech.*, **3**, 151–167.

ON NEURAL NETWORK APPLICATION FOR WELDED JOINT QUALITY CONTROL IN UNDERWATER WELDING

I.O. SKACHKOV[1], **A.E. PIRUMOV**[1], **S.Yu. MAKSIMOV**[2] and **E.A. PRILIPKO**[2]
[1]NTUU «Kiev Polytechnic Institute», Kiev, Ukraine
[2]E.O. Paton Electric Welding Institute, NASU, Kiev, Ukraine

Artificial neural networks have been used to asses the quality of underwater welded joints with four types of fit-up defects: edge misalignment, change in part-to-torch distance, change in the gap between the parts and presence of tack welds. The efficiency of neural network application for the above types of defects is shown, except for a change in the edge gap.

Keywords: underwater welding, non-stationary disturbances, weld metal, quality control, electrical parameters, neural networks

The main problem in welded structure fabrication is reproducibility of welded joint quality in the entire batch of products of one-type. The most widely accepted method to solve this problem is optimizing the mode parameters and minimizing the level of technological disturbances. Table models relating the quality indices with the welding parameters allow producing welded joints with quality parameters not inferior to the limit admissible ones by the respective standards or specifications. However, at increase of the requirements to the welded joint, determined by the design features of the product and presence of disturbances, application of such models cannot always provide the required quality. Elimination of the influence of disturbances is simply impossible in view of the diverse nature of their origin.

In underwater welding the process of weld formation is influenced by a whole range of non-stationary disturbances. For instance, it is impossible to eliminate the probability of appearance of disturbances, resulting from the impact on the man of such environmental factors as poor visibility, current and high pressure. In this connection, quality control of welded joints, which often are supercritical, becomes highly important.

In most of the cases, however, quality control of a welded joint made by wet underwater welding, is performed by external inspection, or in case of pipeline repair, by tightness testing of the joint by excess pressure. Application of universally accepted hardware in a water environment involves great technical difficulties. In view of that development of an objective control technology, simple to implement and reliable in operation is the most urgent goal. Such a technology should ensure control of the quality of weld formation in real time or directly after completion of welding, and not require immersion of either the equipment or control operator under the water.

Information required for evaluation of welded joint quality, can be obtained by analysis of the physical parameters of the welding arc, including electrical parameters [1]. Use of the latter requires minimum hardware means and usually does not increase the weight or overall dimensions of the working components of welding machines. In addition, the welding arc is practically intertialess. For underwater welding the possibility of measuring the welding parameters from the support vessel is particularly attractive.

The essence of the technology of quality control of the welded joint by the electrical parameters of the arc consists in comparing the shape of oscillograms of current and arc voltage with the change of quality indices along the weld length. As most of the defects in the latter nucleate at the stages of weld pool formation and solidification, the condition of one of the electrodes should reflect the features of running of this process. However, presence of both artificial and natural feedbacks hinders interpretation of the shape of oscillograms for determination of welded joint quality, as absolute values of deviations in oscillogram shape are minor. Thus, it is necessary to assess the shape of the curve of current and voltage over a certain period of arcing, and detect deviations which are essential from the viewpoint of weld formation.

In view of the huge number of unpredictable and unchangeable disturbing factors, the process of underwater arcing can be regarded as stochastic. Determination of weld quality can be performed by separation of the oscillogram fragments into groups, corresponding to certain defect types. Thus, the problem of quality control by the electrical parameters of the arc is reduced to clusterization problem. It should be also taken into account that the electric arc (irrespective of arc welding process) has a natural non-linearity. The workpiece being welded also has a significant non-linearity, as its thermophysical and electrical properties depend on temperature. Arc power sources also are predominantly non-linear systems. Thus, the problem of clusterization of sequences formed by a non-linear stochastic system should be solved.

Any disturbances invariably lead to changes of electrode spot fluctuations, and, therefore, affect the electrical parameters of the arc. As these fluctuations are of a random nature, it is rational to analyze their influence by statistical estimates. The most acceptable estimate, allowing adequate assessment of the fluc-

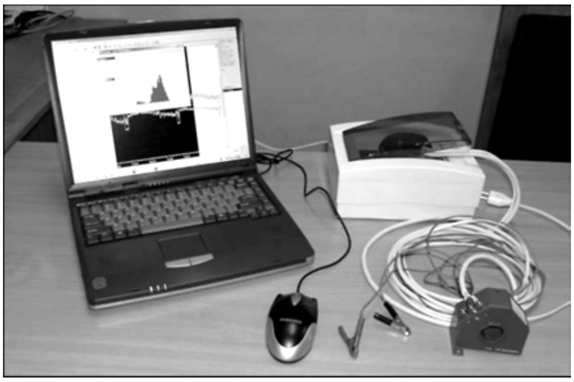

Figure 1. Appearance of the information-measurement system

tuation intensity of the electrode spots when solving the posed problems, is dispersion of the recorded values of welding current and arc voltage.

One of the modern methods of solving the problem is use of neural networks. Selection of this mechanism of data clusterization is determined, first of all, by such features of neural networks as their capability of generalization and tolerance to various interferences. The body of mathematics and software for simulation of artificial neural networks on personal computers are sufficiently well-developed and accessible.

The purpose of this work consisted in determination of the possibility of evaluation of the efficiency of neural network application as a tool for remote monitoring of the quality of wet underwater welding.

Experiments were conducted for the case of wet underwater automatic arc welding. Samples from low-carbon structural sheet steel 10 mm thick with a standard V-shaped groove, were butt welded, using PPS-AN2 flux-cored wire, developed and manufactured at the E.O. Paton Electric Welding Institute. Welding unit of ASUM-400 type was used as the power source. Experiments were conducted in fresh water in a special high pressure chamber under the conditions equivalent to immersion to 10 m depth.

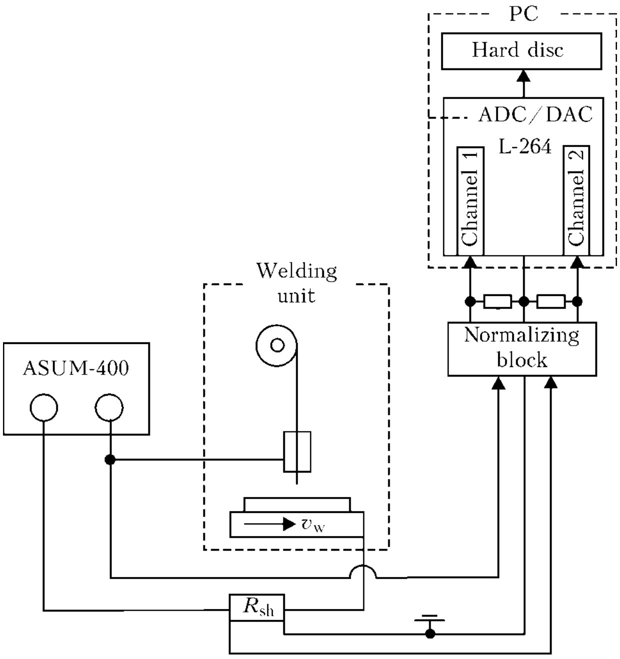

Figure 2. Functional diagram of the welding unit

Current and arc voltage were recorded using information-measurement system (IMS) based on a personal computer, analog input module E-140 manufactured by L-Card Company, Russia, as well as current and voltage sensors of LEM Company, Switzerland, the operation of which is based on Hall effect. The used sensors ensure nomalizing and galvanic decoupling of the input signal. Developed IMS (Figure 1) enables continuous analysis and saving on electronic carriers the values of parameters recorded during the entire welding cycle, and processing the obtained information.

Analog-digital converter frequency of 10 kHz per channel is selected on the basis of published data from [2] and our own preliminary experiments. To increase the measurement accuracy measures were taken to protect the measuring circuits from electromagnetic noise, such as application of twisted pairs, mounting resistors at ADC input (Figure 2) to reduce the influence of the common-mode interference, etc. [3]. In view of the need to perform control from the water surface, arc voltage was measured at the power source terminals (Figure 2). Data recording and processing was performed using File Recorder v.3.2 program from a specialized package Power-Graph v.3.2, compatible with the L-Card products, under the control of Windows XP operating system. The program environment menu enables adjustment of each input ADC channel by entering the data sampling rate and input signal level.

Welded joint quality was evaluated on the basis of four types of disturbances, which impair the quality characteristics of the weld, and are the most often encountered in welding, namely misalignment of the welded part edges, change of the torch-to-part distance, variation of the gap between the parts, and presence of tack welds.

To conduct the experiments each sample was assembled as follows: the initial and final parts of the joint were made with a good quality, and the middle part had the respective defect. Figure 3 gives the schematics of the experimental samples and their photos.

Analysis of current and voltage oscillograms during performance of preliminary experiments and evaluation of the properties of the used equipment led to the conclusion that the welding current is the most informative parameter, as the power source has a flat volt-ampere characteristic, thus making the voltage signal non-informative, in connection with its small variation. Primary processing of the derived signal (elimination of noise using a digital filter) allowed increasing its information level.

Primary processing of the recorded data is followed by their breaking up into blocks, which are approximate multiples of the length of the oscillation period of the instantaneous values of welding current signal, which is attributed to the drop transfer of electrode metal, and is determined by spectral analysis of the data sample. The length of the block was equal to 1000 values, corresponding to the time of 0.1 s.

Thus, for each experiment a matrix of $1000 \times N$ size was obtained, where N is the number of blocks equal to $T / 1000$ (T is the total number of recorded data). Calculation of selective dispersions for each block yielded a vector of $1 \times N$ dimension, which was

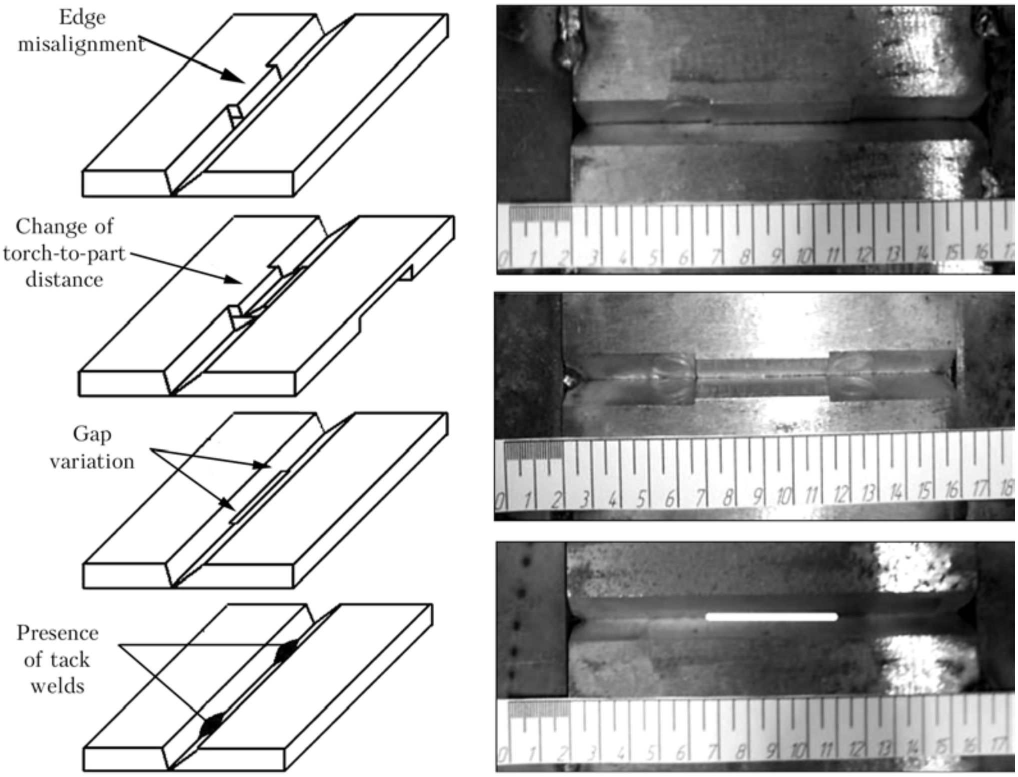

Figure 3. Schematic image and photos of experimental samples with artificially introduced disturbances

redistributed so that the obtained set of these values corresponded to the time of welding performance. The final matrix has the dimension of $10 \times (N / 10)$.

External inspection of the weld and cross-sections of macrosections cut out of it, revealed the good and poor quality regions for further teaching of the neural network.

Fragments of arc parameter oscillograms were clusterized using well-known neural networks — Kohonen map with an ordered arrangement of the neurons and network of type learning vector quantization (LVQ). Both the networks belong to self-organizing ones. Clusterization was conducted by the feature of absence (class 1) or presence (class 2).

Artificial neural network requires teaching for its operation [4], which consists in entering the learning data sample — a set of observations, containing the studied object features. One of the most serious problems in network teaching consists in that in many cases not the noise which should be minimized is actually minimized. This is determined both by the limited volume of the learning sample, and the nature of the data in it. However, increase of the volume of the learning sample may lead to the overlearning phenomenon and the network loosing the most important quality of generalization. In this connection, a mandatory check for overlearning was conducted, using a check sequence, not included into the learning one. When the learning and check sequences were formed, algorithms were additionally used, which allowed revealing and eliminating the errors of measurement due to various interference.

The same learning sequence with 66 blocks was used for both types of the applied networks. The dimension of object matrix for LVQ network was 2×66, as just the presence of a defect was classified. Values for the learning sequence were selected from each experiment. Kohonen map had two neurons, LVQ network had ten neurons in the first layer, and two in the second. The number of neurons of the first layer corresponds to the length of the input vector, that of the second — to the number of classes, into which the input vector is divided. Teaching of LVQ network was conducted during 2000 cycles with 0.001 step.

Checking of the neural network for determination of the accuracy of defect detection was performed by entering into the trained neural network the entire data sequence recorded for each experiment. Error of the network operation was assessed in a sequence, the data from which were not used in teaching. Estimates of the network operation errors are summarized in the Table.

Results of neural network operation on evaluation of the studied sample quality are given in Figure 4. The bars in the diagrams show the presence of defects in the respective weld sections.

Analysis of the obtained data shows that the neural networks quite successfully reveal three out of four artificially introduced assembly defects — edge misalignment (Figure 4, *a*), variation of torch-to-part distance (Figure 4, *b*), and presence of tack welds

Error parameters of neural networks at defect identification

Kind of disturbance	Total number of blocks	Error of network operation, %	
		Kohonen map	LVQ
Edge misalignment	70	15.7	18.6
Variation of torch-to-part distance	60	13.3	13.3
Presence of tack welds	60	16.6	50.0
Gap variation	60	21.6	83.3

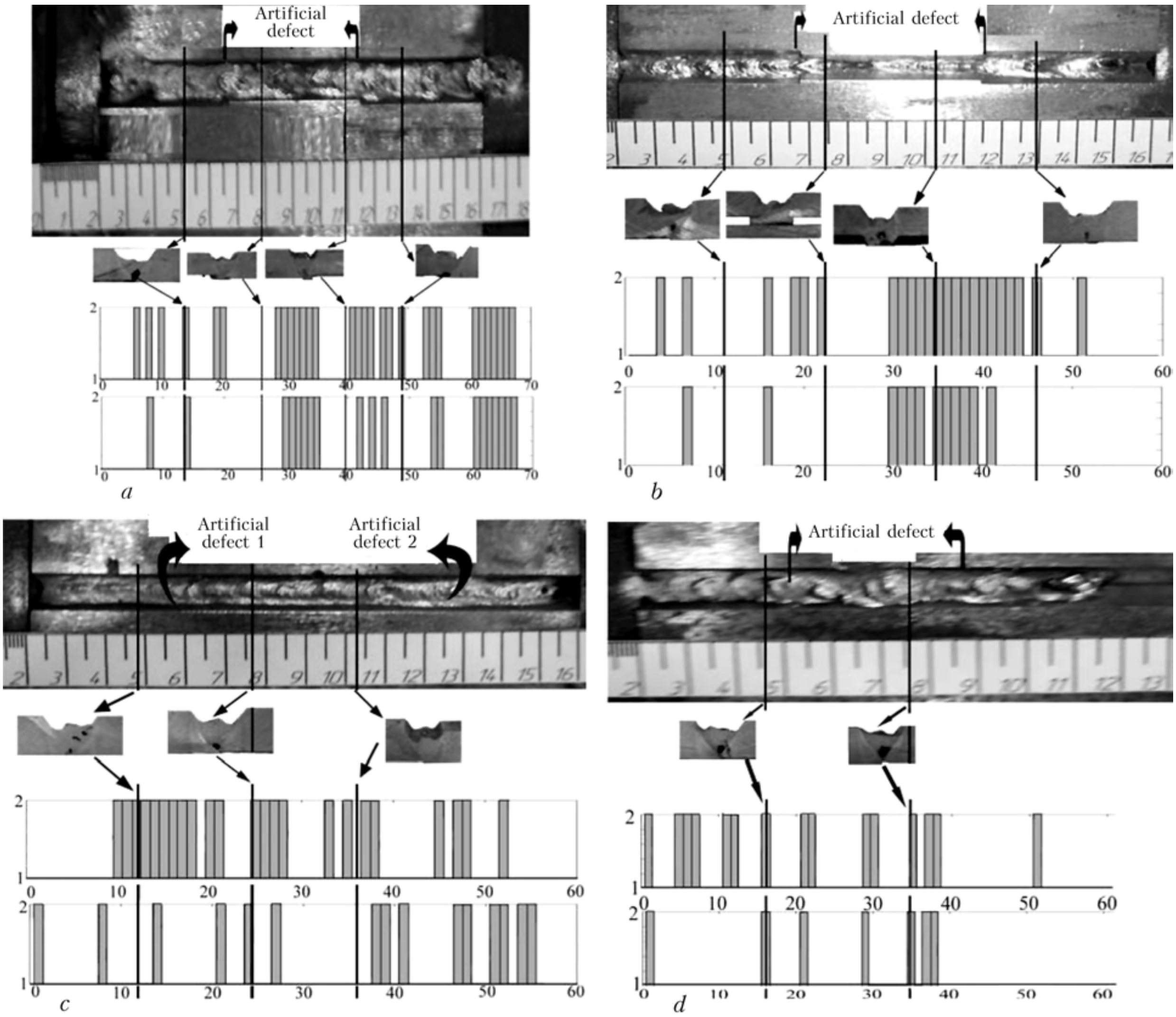

Figure 4. Detection of defects in samples, which are due to edge misalignment (*a*), variation of part-to-torch distance (*b*), use of tacks (*c*) and variation of the gap (*d*)

(Figure 4, *c*). Inaccurate defect detection at the start of its appearance is attributable to unchanged electrical parameters during this period of time, as well as instability of the process during the entire experiment. The error of tack weld detection is associated with the inertia of the process of the arc self-regulation and their small influence on the electrical parameters of the arc. Note the fact of revealing the weld inner defects (slag flowing-in, and lack-of-fusion of the edges), which is seen from the photos of the presented sample sections. The neural networks turned out to be the least sensitive to a step-like change of the gap between the edges (Figure 4, *d*).

Performed investigations demonstrated the basic possibility of applying the artificial neural networks for evaluation of welded joint quality in wet underwater welding. The main advantage of this method is the possibility of its remote application, i.e. placing the instrumentation on the support vessel deck. Increasing the accuracy of network operation is quite real, but requires studying the features of the physical processes, running in the arc at formation of various kinds of defects. Use of neural networks with feedbacks for self-improvement of the systems of weld formation quality monitoring is believed to be promising.

CONCLUSIONS

1. Conducted evaluation showed the principal possibility of applying the artificial neural networks for monitoring the quality of welded joints in wet underwater welding. They allow revealing both the defects of welded joint fit-up, and inner defects of underwater welds (slag flowing-in and lacks-of-fusion).

2. Welding current signal can be the information parameter. Obtained data on the signals need preliminary processing to eliminate the noise and increase the information content of the signal.

3. Proceeding from the obtained error of neural network operation, it is rational to use Kohonen maps in further operation.

1. Zhao, D.B., Chen, S.B., Wu, L. et al. (2001) Intelligent control for the shape of the weld pool in pulsed GTAW with filler metal. *Welding Res.*, **11**, 253–260.
2. Adolfsson, S., Bahrami, A., Bolmsjo, G. et al. (1999) On-line quality monitoring in short-circuit metal arc welding. *Ibid.*, **2**, 59–72.
3. Denisenko, V., Khalyavko, A. (2001) Protection from disturbances of sensors and connecting wires of industrial automation systems. *Sovrem. Tekhnologii Avtomatizatsii*, **1**, 68–75.
4. Medvedev, V.S., Potyomkin, V.G. (2002) *Neural networks: Matlab 6*. Moscow: Dialog-Mifi.

LASER WELDING AND FORMABILITY STUDY OF TAILOR-WELDED BLANKS OF DIFFERENT THICKNESS COMBINATIONS AND WELDING ORIENTATIONS*

C.H. CHENG[1], **L.C. CHAN**[1], **C.L. CHOW**[2] and **T.C. LEE**[1]
[1]Hong Kong Polytechnic University, China
[2]University of Michigan-Dearborn, USA

Tailor-welded blanks (TWBs) are tailor-made for different complex component designs by welding multiple metal sheets with different thicknesses, shapes or strengths prior forming. However, the forming performance of an intrinsic TWB is critically related to its own structures and designs, such as the thickness combination, as well as the location and orientation of weldment. In this study, a 2 kW Nd:YAG laser were used to butt-weld approximately 180 samples of stainless steel (AISI 304) TWBs with different dimensions (from 12.7 to 165.1 mm in width), thickness combinations (1 / 1, 1 / 1.2, 1 / 1.5, 1.2 / 1.2, 1.2 / 1.5 and 1.5 / 1.5 mm) and welding orientations (0°, 45° and 90°). Subsequently, Swift forming tests were carried out to study the forming performance of those TWBs. It was found that the formability of TWBs critically related to the quality of weld was very much affected by the welding parameters of the Nd:YAG laser. Also, the effects of different thickness combinations on the formability of TWBs were investigated through the constructed forming limit diagrams (FLDs). The results showed that the thinner part of TWBs dominated the majority of deformation similar to the FLD of the parent metal. The effects of different welding orientations on the forming performance of TWBs were examined from the failure analysis.

Keywords: *laser welding, tailor-welded blanks, stainless steel, welding orientation, thickness combinations, formability, forming limit*

The use of tailor-welded blanks (TWBs) has increased in practice in the automotive industry and it is being introduced to other potential industrial applications, such as electrical goods, package and construction markets [1]. As TWBs are usually tailor-made for different components, the forming performance of the TWBs is a major concern for the industry which implements TWBs in their production. In recent years, researchers have analyzed the forming performance of steel TWBs using different tests. Saunders and Wagoner [2] have identified two failure modes of TWBs and indicated that the press formability of TWBs related to the changing deformation patterns depended on the differential strength of TWBs. Heo et al. [3] indicated that a higher thickness strain distribution led to a larger movement of weld line during deep drawing. Also, Chan et al. [4] claimed that the formability of TWB decreased against the increase of the thickness ratio of a TWB. Thus, in this paper, an effective laser welding process of stainless steel (AISI 304) TWBs with different welding orientations and thickness combinations is presented, while the effects of welding orientation and thickness combination on the formability of TWBs are investigated.

Laser welding of TWBs. In this study, AISI 304 stainless steel TWBs were butt-welded using a 2 kW Nd:YAG laser. Three stainless steel sheets with thicknesses of 1.0, 1.2 and 1.5 mm were used to produce approximately 180 samples of TWBs having different welding orientations (0°, 45° and 90°) and thickness combinations (1 / 1, 1 / 1.2, 1 / 1.5, 1.2 / 1.2, 1.2 / 1.5 and 1.5 / 1.5 mm). Before the laser welding, the edges of the specimens to be welded were milled and degreased to attain the clean edges without any burrs, contaminates, or oils. Each pair of specimens was assembled on a welding fixture for laser-beam alignment and specimen fit-up, as shown in Figure 1. After exhaustive welding trials, the optimal welding parameters of TWBs for each thickness combinations were identified. In accordance with the British Standards EN ISO 13919-1 and 15614-11, the weld integrity was examined with respect to the conditions of weld surface and cross-sectional weld profile, while the general mechanical properties of the TWBs were measured using the tensile test.

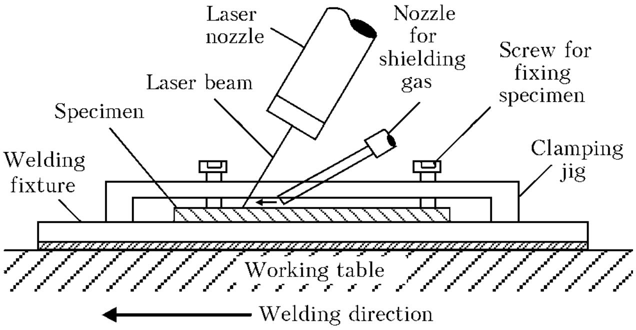

Figure 1. Schematic diagram of the welding

*This paper was presented at the Second Int. Conference on Laser Technologies in Welding and Materials Processing (Katsiveli, Crimea, Ukraine, May 23–27, 2005) and was published in the Proceedings of the Conference (Kiev: PWI, 2005, pp. 167--170).

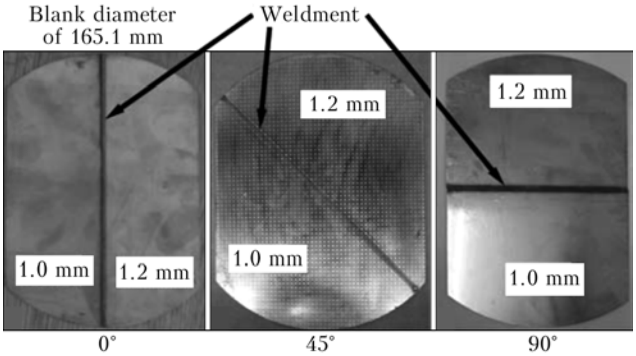

Figure 2. TWBs with different welding orientations

Optimal welding parameters TWBs for different thickness combinations

Thickness combination, mm	Laser power, W	Welding speed, mm / s	Focus position	Argon flow rate, l / min
1.0 / 1.0	1100	27	Surface	20
1.2 / 1.2	1000	23		
1.5 / 1.5	1100	15		
1.0 / 1.2	1000	25	Surface of thicker base metal	
1.0 / 1.5	1100	20		
1.2 / 1.5	1100	15		

Formability test of TWBs. The formability of those produced TWBs was studied using the Swift forming test. Forming limit diagrams (FLDs) were constructed by the major and minor strains measured from the TWB specimens with different widths, whilst the forming behavior and the failure modes of the TWBs were also investigated. The effects of every welding orientation and the thickness ratio were analyzed accordingly. Despite different orientations, almost all the welds were located in the center of TWBs, as shown in Figure 2. A forming tester with a hemispheric punch (50 mm in diameter) was used, while a large blank-holding force of 100 kN was applied to control the material flow. In order to balance the thickness difference within a TWB, tailor-made spacers were designed and applied during the test.

Results and discussion. *Results of laser welding.* After exhaustive trials, AISI 304 stainless steel TWBs with different welding orientations (0°, 45° and 90°), thickness combinations (1 / 1, 1 / 1.2, 1 / 1.5, 1.2 / 1.2, 1.2 / 1.5 and 1.5 / 1.5 mm) and specimen widths (from 12.7 to 165.1 mm) were produced using the 2 kW Nd:YAG laser (see Figure 2). The optimal sets of welding parameters for welding TWBs with different thickness combinations are listed in Table. It is apparent that the optimal welding parameters can be obtained by only varying the welding speed according to the total thickness of base metals on both sides of TWB, whereas a lower welding speed is employed for a thicker material. Meanwhile, the laser power could be fixed within a narrow range from 1000 to 1100 W. For all thickness combinations, the laser beam was focused on the joint of the top surface of the specimen or the thicker base metal, while argon gas with a flow rate of 20 l / min was used for shielding.

Figures 3 and 4 show, respectively, the weld surface and the cross-sectional weld profile obtained from a TWB (1.2 / 1.5 mm) welded using a set of the optimal parameters. The weld surface was found clean and continuous throughout the entire length of the TWB without any observed cracks or porosity, while an acceptable weld profile was attained without any defect such as underfill, undercut or weld-sagging. The tensile properties of the TWBs with different thickness combinations of transversal welds were evaluated using subsize specimens of TWBs. The tensile test was carried out under a constant cross-head speed of 1 mm / min until the initiation of localized necking.

As shown Figure 5, most failures were typically found in the base metal rather than the weld or the heat-affected zone (HAZ), indicating that the acceptable welds, as well as the quality TWB, can be obtained using such welding parameters. The stress-strain curves of the TWBs were measured as shown in Figure 6. The curves *1*, *2* and *3* showed that the TWBs with similar thickness combinations (1 / 1, 1.2 / 1.2 and 1.5 / 1.5 mm) possessed similar stress and strain values as those of their base metals. However, for the TWBs with different thickness combinations (1 / 1.2, 1 / 1.5 and 1.2 / 1.5), a larger difference in

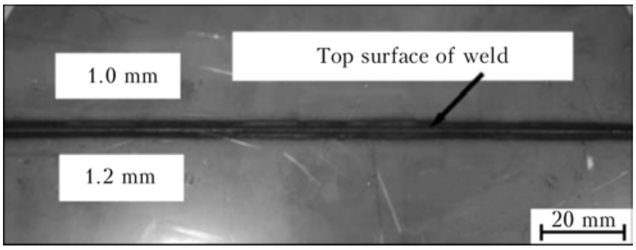

Figure 3. Weld surface of TWB produced under optimal parameters

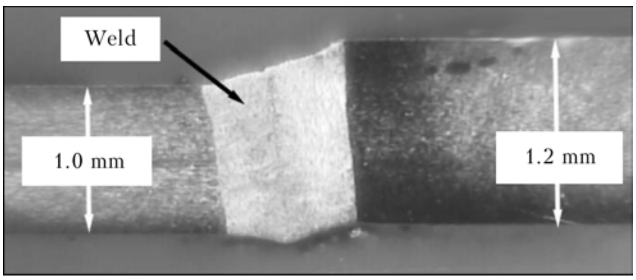

Figure 4. Cross-sectional weld profile of TWB produced under optimal parameters

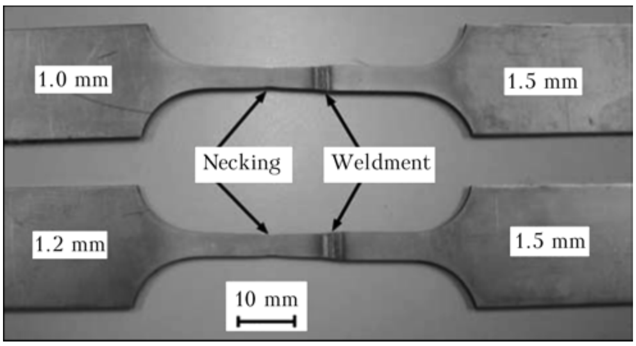

Figure 5. Some results of tensile test for TWBs

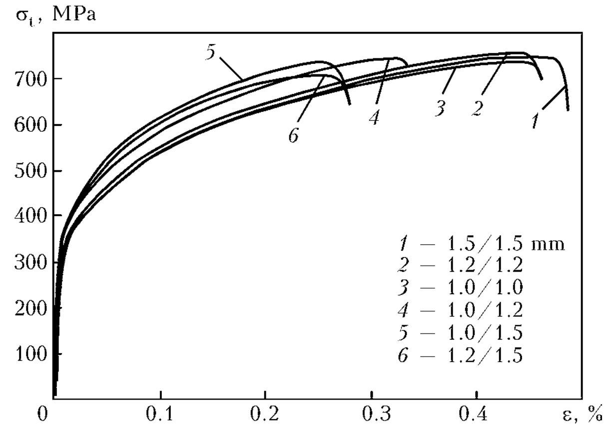

Figure 6. Tensile curves for TWBs with different thickness combinations

thickness with the TWB resulted in lower strain values (curves *4–6* in Figure 6). This was because the deformations of TWBs were predominated by the thinner base metals (see Figure 5).

Results of formability test. Swift forming tests were carried out to study the forming behavior of the TWBs, as well as their formability. Figure 7 shows the formed TWBs (thickness combination of 1 / 1.2 mm) with different welding orientations. It

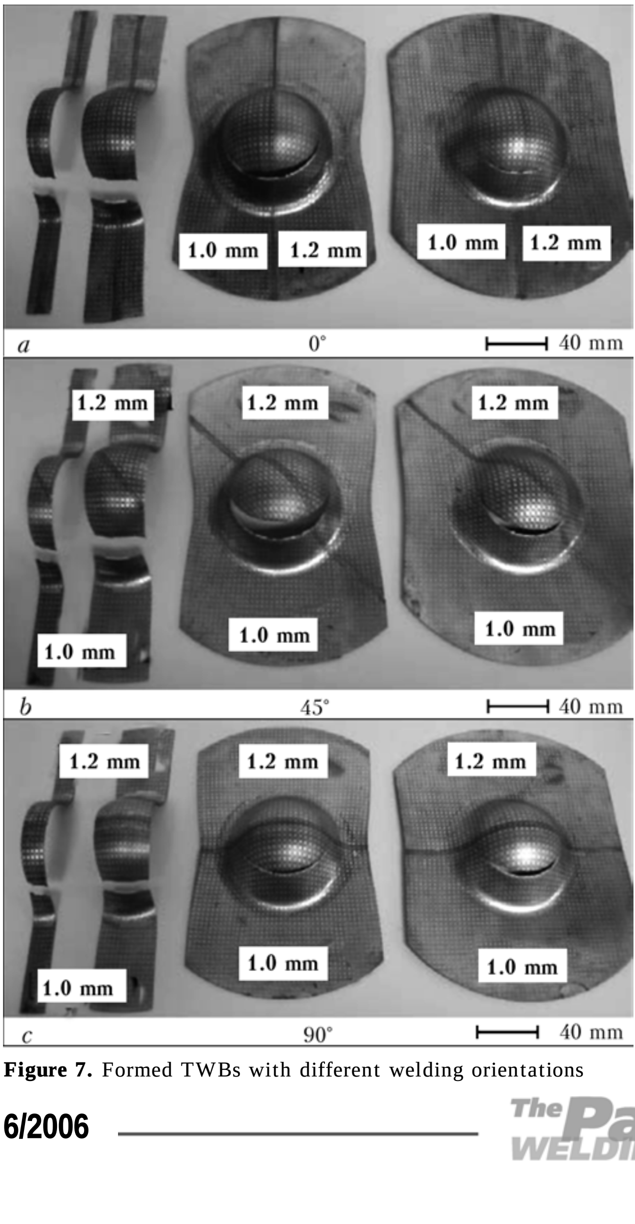

Figure 7. Formed TWBs with different welding orientations

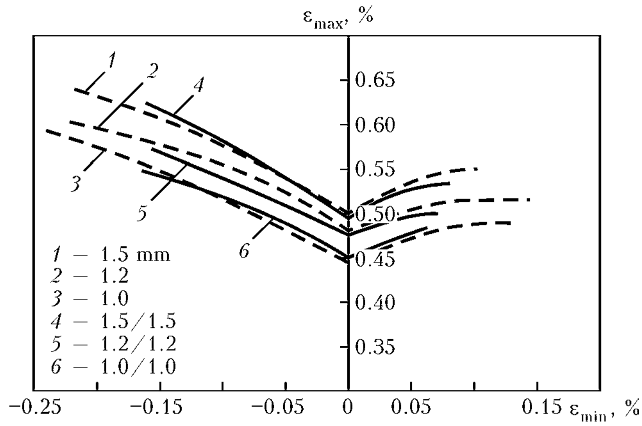

Figure 8. FLDs of stainless steel TWBs with similar thickness combinations and for welding orientation of 90°

was found that the locations of failures for all the TWBs with different welding orientations were similar, and all the failures propagated perpendicular to the major loading direction. Failures of TWBs with 45° and 90° welding orientations (Figure 7, *b*, *c*) were found to occur in their thinner base metal away from the weld, while failures initiated at the weld of the TWBs with 0° orientation (Figure 7, *a*). Thus, the quality welds with different orientations may be concluded to have insignificant effect on the forming behavior and the failure mode of TWBs as the failures mainly occur in the thinner base metals perpendicular to the major loading direction.

In order to study the formability of the TWBs, their FLDs were constructed by measuring the major and minor strains of circular pre-printed grids on the surface of TWBs. Figures 8 and 9 show, respectively, the FLDs of TWBs (welding orientation of 90°) with both similar and different thickness combinations. Comparing to the FLDs of base metals (see dotted curves), the TWBs with similar thickness combinations possessed the similar formability as their corresponding base metals. This revealed that the weldments with 90° orientation to the major loading direction had slight effect to the TWBs with similar thickness combinations. Most of the failures in TWBs with different thickness combinations (see Figure 7, *c*) located in the thinner base metal so that similar FLDs were obtained as those of their thinner base metals.

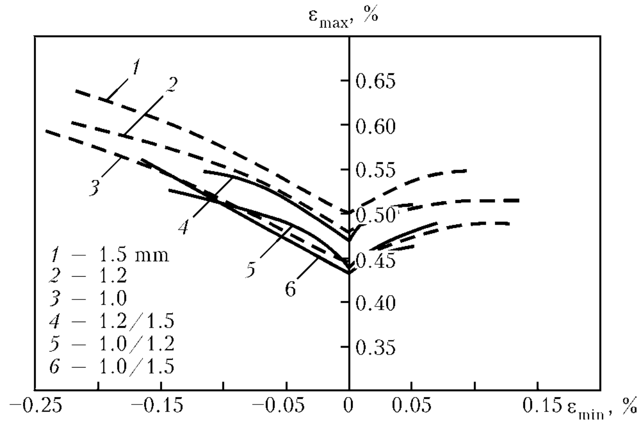

Figure 9. FLDs of stainless steel TWBs with different thickness combinations and for welding orientation of 90°

CONCLUSIONS

In this study, AISI 304 stainless steel TWBs with different welding orientations and thickness combinations were produced using a 2 kW Nd:YAG laser. Optimal set of welding parameters for different thickness combinations were identified based on the weld integrity and the tensile properties of the TWBs. On the other hand, similar failure modes were observed on the TWBs with different welding orientations. Once the quality weld is attained, failure generally occurs in the thinner base metal of TWB similar to the FLDs of their corresponding thinner base metal. One may also conclude that the FLD alone was not able to reveal any meaningful limit strain data of TWB made of different thickness combination.

Acknowledgment. The work described in this paper was partially supported by grants from the Research Grants Council of the Hong Kong Special Administrative Region, China (Project No. PolyU 5178 / 01E) and the Research Committee of the Hong Kong Polytechnic University (Project No. G-T906).

1. Pallett, R.J., Lark, R.J. (2001) The use of tailored blanks in the manufacture of construction components. *J. Materials Proc. Technology*, **117**, 249–254.
2. Saunders, F.I., Wagoner, R.H. (1996) Forming of tailor-welded blanks. *Metallurgical and Materials Transact. A*, **27A**, 2605--2615.
3. Heo, Y., Choi, Y., Kim, H.Y. et al. (2001) Characteristics of weld line movements for the deep drawing with drawbeads of tailor-welded blanks. *J. Materials Proc. Techno-logy*, **111**, 164–169.
4. Chan, S.M., Chan, L.Ñ., Lee, T.C. (2003) Tailor-welded blanks of different thickness ratios effects on forming limit diagrams. *Ibid.*, **132**, 95--101.

BASICS AND APPLICATIONS OF LASER-GMA HYBRID WELDING*

C. THOMY and **T. SEEFELD**
BIAS GmbH, Bremen, Germany

A basic requirement for exploiting the specific advantages of laser-GMA hybrid welding is a comprehensive, fundamental understanding of the interactions of the two sub-processes laser welding and GMA welding, as their synergetic interactions significantly contribute to the advantages of hybrid welding. However, for an effective as well as efficient industrial application, a thorough analysis of the requirements of the specific applications and the industrial environment is a prerequisite. Thus, within this paper, after an overview on hybrid welding, some interaction phenomena between the sub-processes are given a closer look. Based on these considerations, two applications (laser-GMA hybrid welding in pipe production and in welding of extruded aluminium profiles in the railway industries) are discussed.

Keywords: laser welding, hybrid welding, steel, aluminium, sheet materials, welding speed, thickness, outlook

Among others, the hopes for a reduction of investment and operating costs, decreasing cycle time and improving product quality are often the driving forces for developing and applying innovative welding processes such as laser-GMA hybrid welding. This welding process is generally characterised by the combination of laser beam welding and GMA welding in one common process zone (melt pool and plasma) and was first investigated in the 1970s [1]. Among the advantages commonly associated with hybrid welding is a significant process stabilisation, higher achievable welding speeds especially compared to arc welding, lower tolerance requirements compared to laser welding and, in some cases, improved weld properties.

Exploiting these advantages, a variety of application potentials arises, in special in welding of thicker steel materials [2--5]. Due to the laser powers required for these sheet thicknesses, up to now mainly CO_2-lasers (typically with beam powers exceeding 8 kW) have been applied for these tasks.

In contrast, for welding of aluminium alloys in sheet thicknesses normally used in the automotive industries, the beam powers delivered by today's Nd:YAG-lasers (accepting some restrictions considering welding speed) suffices. Consequently, due to the easy beam delivery (fibres instead of mirror systems as for CO_2-lasers) and certain process properties, Nd:YAG-laser-GMA hybrid welding is often applied [6]. Moreover, the development of commercially available hybrid welding systems is currently focussing on Nd:YAG-laser-GMA hybrid welding.

However, Nd:YAG-laser-GMA hybrid welding is (due to the comparably low laser powers) normally re-

*This paper was presented at the Second Int. Conference on Laser Technologies in Welding and Materials Processing (Katsiveli, Crimea, Ukraine, May 23–27, 2005) and was published in the Proceedings of the Conference (Kiev: PWI, 2005, pp. 203--206).

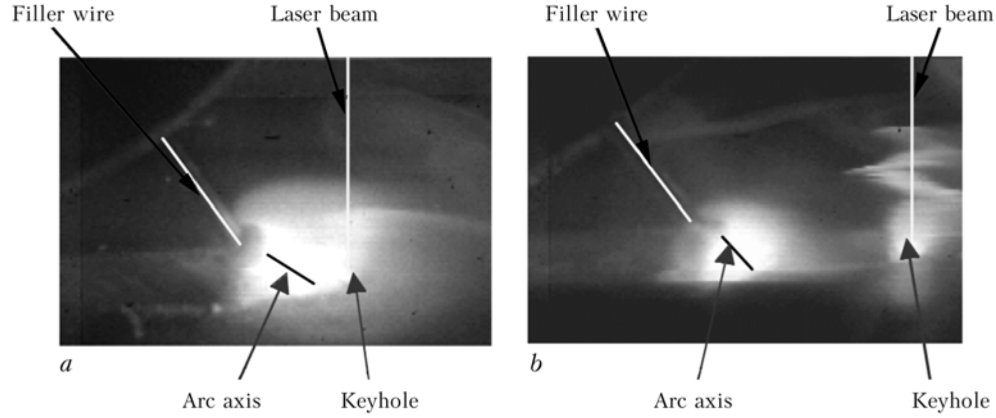

Figure 1. Influence of the laser beam on the arc at laser–arc distance of 3 (*a*) and 9 (*b*) mm

stricted in view of sheet thickness and consequently not capable of covering the complete range of thicknesses encountered, e.g. in welding of extruded aluminium profiles for railway structures. Thus, there is a demand for higher and easily deliverable beam powers which may be answered by the high-power fibre laser.

Interaction phenomena in laser-GMA hybrid welding. To be able to fully exploit the benefits arising from the combination of a gas-metal arc and a laser beam to a hybrid welding process, a wide variety of parameters have to be optimized in view of the specific demands of the task. However, as these parameters (e.g. laser power or welding voltage) often significantly interact, a fundamental understanding of these interactions is required.

The mutual interaction between laser beam and GMA becomes obvious if high-speed videos of the process are analysed. Taking the position of the arc axis, on the one hand, for a laser–arc distance of 9 mm, no arc deviation is observed (Figure 1).

Consequently, it does not seem to be justified to talk of hybrid welding for such a process distance. Rather, it has to be expected that for this spatial arrangement, the advantages of hybrid welding resulting from process interactions are reduced to the effects of temperature field modifications. On the other hand, for a laser–arc distance of 3 mm, i.e. for a «real» hybrid welding process, the arc axis is significantly deviated towards the keyhole, and a common process plasma is formed. Comparable observations can be made for the influence of the beam power applied, so the optimisation of the relation of laser power to arc power may be of significance, too.

Taking the example of CO_2-laser-GMA hybrid welding of steel, the interactions of laser beam and GMA were given a closer look. Within these experiments (P_L = 4–9 kW, welding speed v = 1.8 m / min, U = 19–30 V, wire feed rate — 9 m / min, Ar + He shielding gas) it was established that both increasing arc power P_{GMA} and increasing laser power P_L contribute to a significant reduction of short-circuiting frequency and thus greatly influence the mode of metal transfer (Figure 2).

CO_2-laser-GMA hybrid welding in pipe production. In order to implement CO_2-laser-GMA hybrid welding on an existing production unit for longitudinally and continuously welding stainless steel linepipes by the help of an 8 kW CO_2-laser, a welding head (Figure 3) integrating both sub-processes was developed, built and tested by BIAS, paying special attention to the thermal loads resulting from continuous welding times of several hours. These loads are not only due to the arc, but also due to the laser plasma and back-reflections of the laser beam.

During the production tests, a welding speed of 1.2 m / min was achieved for pipelines up to ∅ 273 × 8 mm (steel 12Cr–4.5Ni–1.5Mo) using laser powers up to 7 kW and arc powers up to 8 kW. This welding speed means an increase in processing speed of more than 300 % compared to conventional arc welding processes. It was not limited by the welding process itself but rather by the restrictions of the forming unit. Considering quality, 100 % X-ray testing (DIN EN 25817 C) demonstrated that the produced welds were 100 % defect-free according to the company's requirements in view of cracks, pores and other imperfections. Figure 4 shows a cross-section of a pipe ∅ 273 × 5 mm.

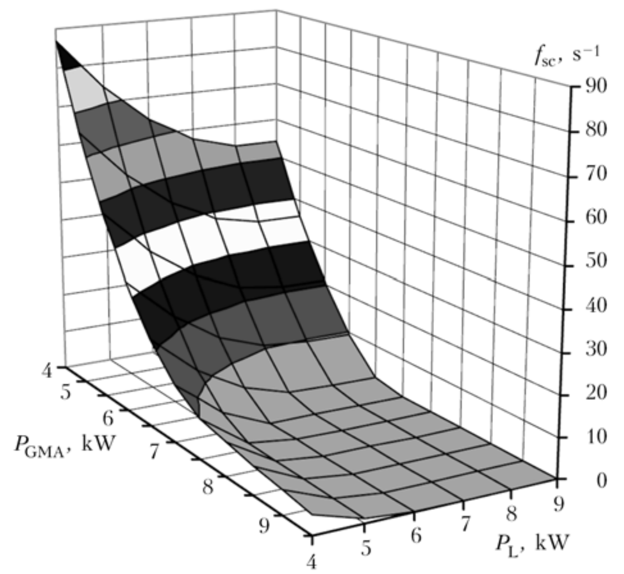

Figure 2. Influence of laser power P_L and arc power P_{GMA} on short-circuiting frequency f_{sc}

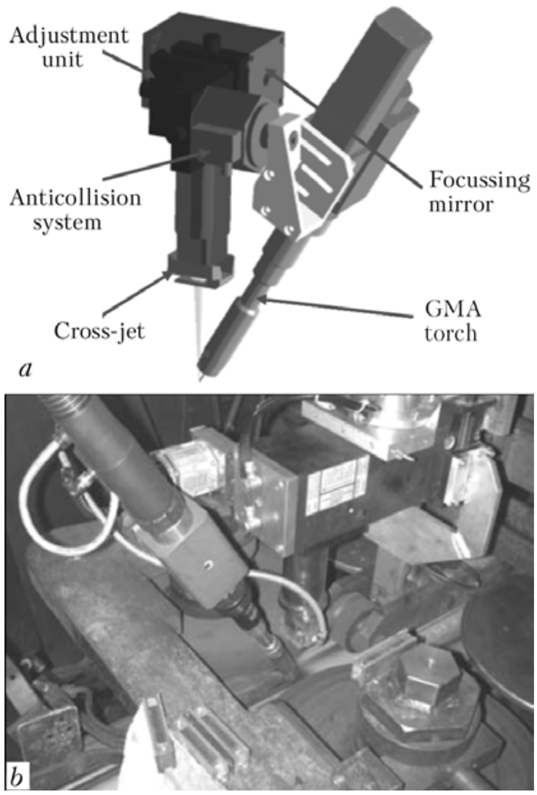

Figure 3. Design (*a*) and industrial application (*b*) of CO_2-laser-GMA hybrid welding head

From this application, it became obvious that, if hybrid welding is integrated in production systems mainly designed for arc welding processes, the welding speed is often not the critical factor for reducing cycle time. Rather, new bottlenecks in operations before or after welding (such as handling processes) arise, making additional efforts necessary to be able to fully exploit the benefits of hybrid welding.

Solid-state laser-GMA hybrid welding of railway structures. One of the central targets of the study on Nd:YAG-laser-GMA hybrid welding of extruded aluminium profiles was the production of test panels. The roof segment displayed in Figure 5 is a prototype section of the roof of the ICN train produced from six extruded aluminium profiles (AlMgSi0.7, t = 3 mm, filler wire AlSi12) with a length of 2 m. No special clamping devices were used. With a laser power of 4 kW at workpiece and an arc power of the pulsed

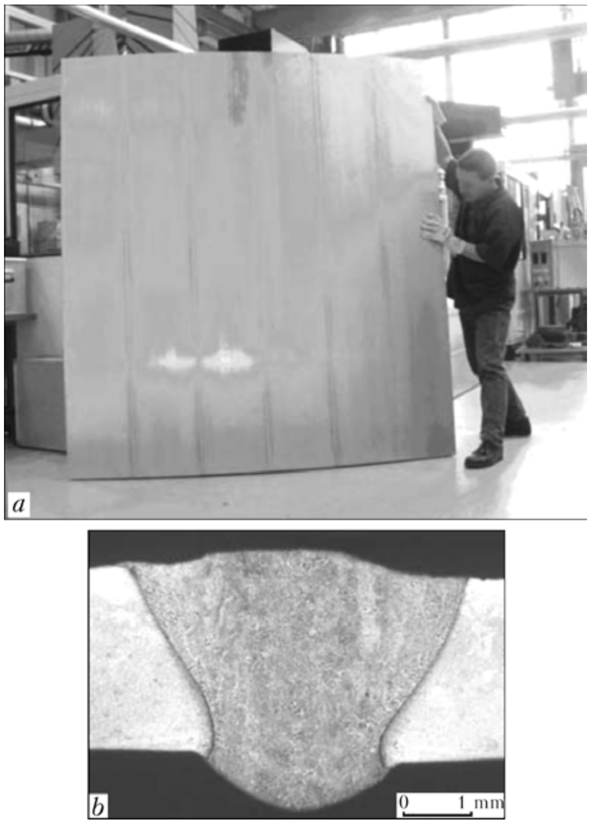

Figure 5. Roof segment of the ICN train (*a*) and weld cross-section (*b*)

GMA of 3.65 kW, a welding speed of 4 m / min was achieved.

It was demonstrated that Nd:YAG-laser-GMA welding is a feasible process especially in view of the requirements considering gap bridging. Consequently,

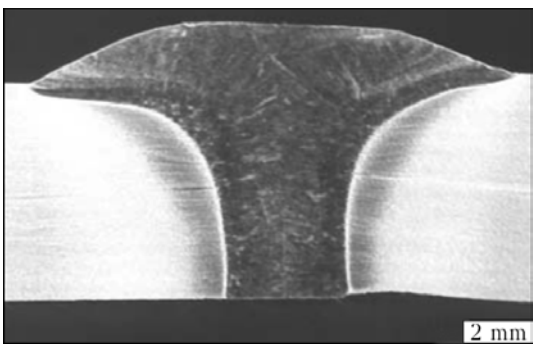

Figure 4. Cross-section of pipe ∅ 273 × 5 mm of 12Cr–4.5Ni–1.5Mo steel

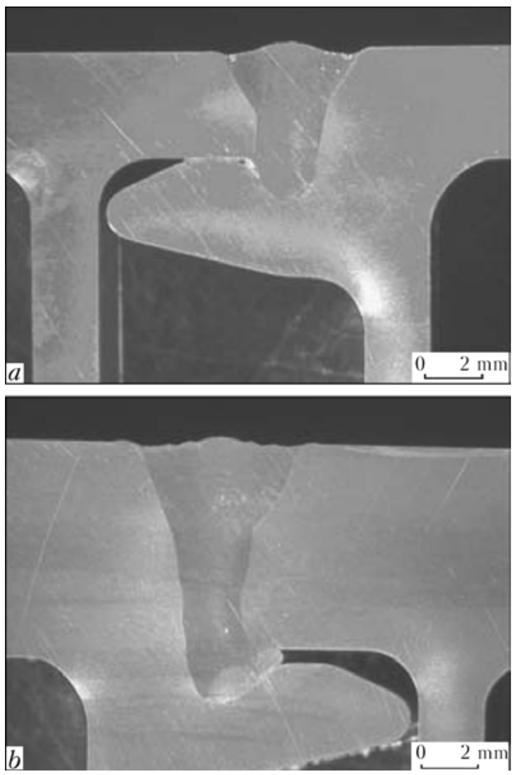

Figure 6. First IPG fibre laser-GMA hybrid welds on EN-AW 6008 alloy with wall thickness of 4 (*a*) and 8 (*b*) mm

special efforts considering seam preparation, clamping technology or gantry precision are not required. Moreover, compared to pure GMA welding, Nd:YAG-laser-GMA welding allows a significant increase in welding speed, which is associated with a reduction of seam volume and total heat input (up to 85 %), thus resulting in a considerably lower distortion [7].

To surpass the limitations imposed by a laser power restricted to 4 kW, an IPG fibre laser of the 10 kW class was applied to hybrid welding, too. Figure 6 shows two first results obtained on EN AW 6008 (wall thickness 4 and 8 mm, respectively) with filler wire AlSi5. Welding speed was 6 m / min in all cases with laser power up to 10.5 kW for the 8 mm material.

The process was very stable and weld quality was acceptable. Further optimisation might result in even higher welding speeds especially for a wall thickness of about 4 mm. These results have been rated so promising that further tests to pre-qualify fibre laser-GMA hybrid welding for this application are scheduled.

CONCLUSIONS

It is safe to say that laser-GMA hybrid welding in its various forms especially considering the type of laser has found and will find numerous interesting industrial applications. However, for a successful industrial implementation of laser-GMA hybrid welding a deepened understanding of the process, as well as an exact analysis of both the welding process and the production system, is required. In special, the significant increase in welding speed has to be considered.

Recently, the high-power fibre laser enhances the application potentials of hybrid welding, as it combines the easy beam handling of the Nd:YAG-laser with the power of the CO_2-laser and possesses numerous other specific advantages such as a high efficiency and a small footprint. Consequently, this laser can be applied to tasks where lasers have not been considered previously, thus increasing the potential application fields for hybrid welding, too.

Acknowledgements. The authors are particularly grateful to the European Commission «Development of Advanced Joining Technologies for Supermartensitic Stainless Steel Line Pipes — JOTSUP» (GRD1-1999-10278)) as well as to the Bremer Innovationsagentur GmbH (funding on behalf of the Senator fur Wirtschaft und Hafen der freien Hansestadt Bremen (AMST P2)) and the BMBF (project Leichter: 13N7460-5) and the Deutsche Forschungsgemeinschaft DFG (Gottfried-Wilhelm-Leibniz-Programm, VO530/7) for funding considerable parts of the work presented.

1. Steen, W.M., Eboo, M. (1979) Arc augmented laser welding. *Met. Constr.*, 11(**7**), 332–333, 335.
2. Wieschemann, A. (2001) *Entwicklung des hybrid-und hydraschweissverfahrens am beispiel des schiffbaus*. Aachen: Shaker.
3. Thomy, C., Sepold, G., Seefeld, T. et al. (2002) Industrial implementation of laser / GMA welding and mechanical properties of the welds. In: *Proc. of Supermartensitic Stainless Steels Conf.* (Brussels), 147–155.
4. Kaierle, S., Dahmen, M., Bongard, K. et al. (2002) Hybridschweissen von Oeltanks — ein innovativer Fuegeprozess. In: *Proc. of Grosse Schweisstechnische Tagung* (Nurnberg), 207–209.
5. Miebach, R., Lembeck, H. (2003) Die neue Fertigung der Meyer-Werft-Laserhybridschweissen als Kerntechnologie. In: *Proc. of Grosse Schweisstechnische Tagung* (Berlin), 187–192.
6. Staufer, H., Helten, S. (2003) Laser-Hybridschweissen fur neuartige Leichtbaukonzepte im Automobilbau. *Ibid.*, 175–180.
7. Harlfinger, N. (2003) *Laserstrahlgeschweisste Leichtbaustrukturen im Schienenfahrzeugbau. Verbundprojekt Innovativer Leichtbau durch energiereduziertes Fuegen mit Lasersystemen neuester Generation (LEICHTER)*. VDI-Technologiezentrum, 61–68.

MECHANICAL PROPERTIES OF PLASMA WELDED JOINTS ON ALUMINIUM-LITHIUM ALOYS

T.M. LABUR, A.A. GRINYUK and **A.G. POKLYATSKY**
E.O. Paton Electric Welding Institute, NASU, Kiev, Ukraine

Comparative analysis has been performed of mechanical joints in high-strength aluminium alloys 1420 and 1460 made by plasma and nonconsumable electrode argon-arc welding, using batch-produced welding wires SvAMg63 and Sv1201 at alternating-polarity asymmetrical current. It is shown that the strength and fracture toughness of the welds in off-centre tension of specimens strongly depend upon the thermo-physical parameters of welding.

Keywords: plasma welding, aluminium-lithium alloys, welded joints, weld metal, mechanical properties

Development of aerospace engineering products of new modifications with more efficient tactical-technical and economic parameters makes higher demands of the properties of materials and their welded joints. Use of aluminium alloys of Al–Mg–Li (1420 alloy) and Al–Cu–Li (1460 alloy) alloying systems allows reducing the structure weight by 8 to 15 % due to a high specific strength and higher modulus of elasticity. A feature of the alloys is a multicomponent composition and strengthening phase inclusions, located in parallel to the rolling direction. Under the conditions of process heating, including welding processes, these alloys are prone to embrittlement [1, 2].

Arc welding processes are the most readily adaptable to fabrication and most widely used methods of producing permanent joints on Al–Li alloys. A wide use of the nonconsumable electrode provides a higher density of weld metal compared to consumable electrode welding, which has a higher efficiency. Traditional processes of welding by alternating sinusoidal current are characterized by a relatively low penetrability. Use of asymmetrical current of alternating polarity with a square wave and low-frequency modulation causes a periodical deepening of the weld pool, thus facilitating metal degassing and reducing the quantity of pores and oxide film inclusions in the weld metal.

Use of helium as a shielding gas in nonconsumable electrode DCSP welding promotes an increase of the arc thermal power, this increasing the penetration depth and welding speed. Process implementation requires a high accuracy of the part preparation and fit-up, as well as sophisticated equipment for its control. In addition, helium increases the cost of technological operations.

To increase the welding speed, provide the weld quality and reduce the distortions, it is necessary to use high power density heat sources. One of these sources can be the constricted arc, which is «squeezed» by a gas flow blown through a special nozzle. The plasma welding process represents further development of the nonconsumable electrode welding process. Inert gas supplied through the nozzle with a small orifice, constricts the electric arc running between the tungsten electrode and the workpiece.

In welded joints produced by various processes of arc (consumable and nonconsumable electrode) and electron beam welding, formation of a non-uniform structure and metal softening in the HAZ [3] are observed, which is due to metal overheating during the thermal cycle of welding. The latter leads to development of inhomogeneity in the welded joint by the content of alloying elements and impurities due to their segregation along the grain boundary, formation of brittle intergranular interlayers from oversaturated phases, particularly on the fusion boundary, where the interlayers form a dense fringe around the grains. The associated increase of stress concentration facilitates crack initiation by phase cracking or violation of the contact with the matrix, this lowering the indices of strength and toughness of welded joints in Li-containing alloys and operational reliability of welded structures as a whole. In this connection, it is rational to assess the mechanical properties of welded joints of Al–Li alloys made by plasma welding, and compare them with the results, obtained in regular nonconsumable electrode argon-arc welding.

Experimental procedure. Plasma welding of alloys 1420 and 1460 mm 4 and 3 mm thick on a backing with the forming groove was performed with alternating polarity asymmetrical square wave current. Plasmatron was moved by welding head ASTV-2M at the speed of 36 m / h. To increase the resistance of the plasmatron tungsten electrode, welding was performed with a longer duration of straight polarity current period. Duration of reverse polarity current running was selected to be minimum admissible one for an effective cathode breaking up of the oxide film. The ratio of the time of current running at the straight and reverse polarity was 3:1. Experiments were performed using a plasma welding set-up based on the equipment of Fronius, Austria. It includes PT 450-02 WZ power source, filler wire feed mechanism KD 4000, PMW 350 plasmatron and welding control system FPA 2003. Power source allows adjustment of welding current in a broad range of 10 to 450 A with the frequency of polarity variation of 40 to 240 Hz. Frequency of alternating polarity current was equal to 100 Hz. PMW 350 plasmatron ensured a stable formation of the high-temperature plasma jet. Diameter of the plasma-forming nozzle was selected to be minimal (3.2 mm), proceeding from the condition of prevention of double arcing. Nozzle channel diameter was calculated by the following formula $d_n \geq 1 +$

Table 1. Modes of plasma and argon-arc welding of aluminium-lithium alloys by alternating polarity asymmetrical current

Alloy grade	v_w, m / h	I_w, A	Q_m, l / min	v_f, m / h
Argon-arc welding				
1460	14	200	--	82
1420	12	200	--	75
Plasma welding				
1460	36	180	0.1	123
1420	36	200	0.2	142

+ $0.01I_w$, where d_n is the nozzle diameter, mm; I_w is the welding current, A.

Argon-arc welding by alternating polarity asymmetrical square wave current was performed using MW 450 power source of Fronius, Austria, and ASTV-2M welding head, at the speed of torch displacement of 12 to 14 m / h. Modes of plasma and argon-arc welding are given in Table 1.

Welding wires SvAMg63 and Sv1201 of 1.6 mm diameter were used as the filler material. Aluminium sheets and filler wires were subjected to chemical etching before welding, and the sheet edges were additionally mechanically scraped to not less than 0.1 mm depth.

The influence of various processes of welding high-strength Al–Li alloys 1420 and 1460 on the physico-mechanical properties of weld metal was studied, including strength, hardness and fracture toughness indices. Tests were conducted at uniaxial and off-center tension [4].

Testing by uniaxial tension was performed using flat standard samples, and testing by off-center tension — using 36 × 57 mm samples 3 mm thick with a sharp notch of 11 mm depth and 0.1 mm radius at its tip. The straining rate at testing welded joint samples was 2 mm / min ($3.3 \cdot 10^{-5}$ m / s). During testing the load-deformation diagram was recorded by the oscillograph, which fixed the practically important moments of crack initiation and propagation in the studied sample up to its complete fracture. The diagram not only provides a quantitative estimate of the stress intensity during sample deformation at off-center tension, but also determines the time of the stage of a stable metal flowing and work done by it at individual stages of propagation of a crack, formed at welded joint fracture.

Conditions of testing at off-center tension met the technical requirements of GOST 25.506. Experimental results were obtained at testing five samples, using an all-purpose machine RU-5 and calculation of the initial data.

The results of testing at off-center tension were used to determine the values of nominal stress σ_t, and critical coefficient of stress intensity K_c, as well as specific work of crack initiation J_c and propagation (SWCP) [4, 5]. J_c values were evaluated by calculation of the function of deformation energy variation, depending on the crack length, using Merkle--Corten relationship [5].

Analysis results were compared with the data on the nature of variation of the fracture profile, which was obtained using a scanning electron microscope JSM-840 with a system of microanalyzers Analitik Link — 860 / 500 Obtek (at accelerating voltage of 15, 20, 30 kV). Such an integrated approach allowed revealing the structural features of weld formation in plasma and nonconsumable electrode argon-arc welding.

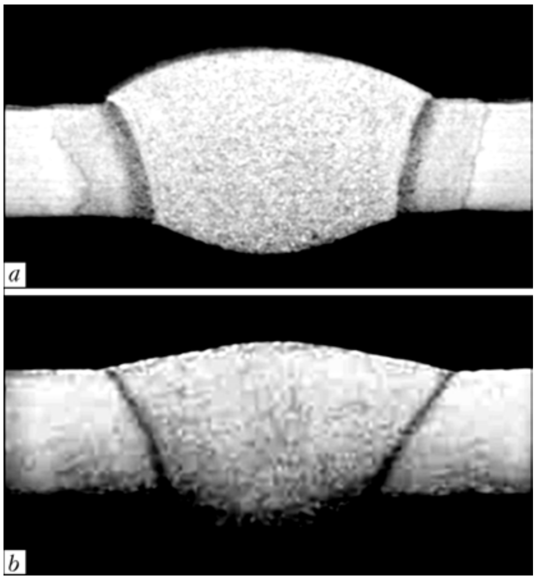

Figure 1. Transverse macrosections of joints of alloy 1460 3 mm thick made by plasma (*a*) and nonconsumable electrode argon-arc (*b*) welding with filler wire Sv1201: *a* — v_w = 36; *b* — 14 m / h

Results and their discussion. High specific power of the plasma flow and level of temperature in the metal section, where the active heated spot is located, promote increase of the constricted arc penetrability and depth of its immersion into the weld pool melt, this allowing the process speed to be increased, compared to the regular nonconsumable electrode argon-arc welding by 2 to 3 times at the same values of current (Figure 1). A smaller heat input into the base metal leads to a certain shortening of the extent of the HAZ and lower degree of softening of the welded joint (Figure 2). However, under the conditions of uniaxial tension the strength of welded joints and metal of welds produced both by argon-arc and plasma welding, are practically on the same level (Table 2).

At off-center tension of welded joints the indices of strength and fracture toughness of welds essentially depend on the welding process (Table 3). Various thermal conditions of heating and cooling rates of the metal accompanying the process of welded joint formation, lead to variation of the strength, ductility and fracture toughness properties of welds. Breaking stress σ_t in the metal of welds produced by argon-arc welding of alloy 1420 is equal to 289–320 MPa, and that of alloy 1460 is 278–306 MPa (Table 3). K_c values for welds of alloy 1420 are equal to 23--25, and

Table 2. Mechanical properties of welded joints of aluminium-lithium alloys at uniaxial tension produced by different welding processes

Alloy grade (sample thickness, mm)	Welding process	Filler grade	$\sigma_t^{w.j}$, MPa	$\sigma_t^{w.m}$, MPa
1420 (δ = 4)	Argon-arc	SvAMg63	328	322
	Plasma		330	316
1460 (δ = 3)	Argon-arc	Sv1201	308	252
	Plasma		302	261

Table 3. Indices of strength, fracture toughness and impact toughness of welded joints on aluminium-lithium alloys 1420 and 1460 at off-center tension

Alloy grade	Filler grade	σ_t, MPa	K_c, MPa$\sqrt{m}$	J_c	SWCP	KCV
				J / cm^2		
Argon-arc welding						
1420	SvAMg63	289--320 / 304	23–25 / 24	3.5--5.8 / 4.4	4.5–5.7 / 4.9	3.5--5.3 / 4.9
1460	Sv1201	278--306 / 293	25–27 / 26	5.8--7.2 / 6.5	5.3–6.1 / 5.7	6.7--7.1 / 7.2
Plasma welding						
1420	SvAMg63	379--428 / 401	25–35 / 30	6.3–10.2 / 7.4	5.3–7.5 / 6.4	4.4--7.9 / 5.9
1460	Sv1201	383--420 / 403	31–36 / 35	8.4--9.3 / 8.8	7.0–8.1 / 7.5	8.6–10.4 / 9.5

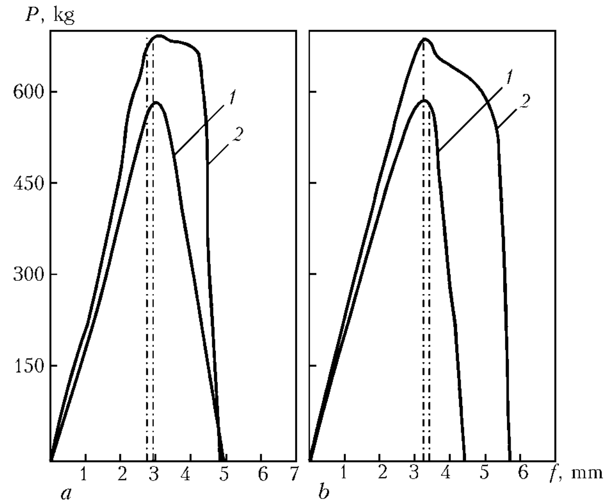

Figure 3. Diagrams of load-displacement P–f at testing under off-center tension of welded joint samples of alloys 1420 (*a*) and 1460 (*b*) made by argon-arc (*1*) and plasma (*2*) welding

those of alloy 1460 to 25--27 MPa$\sqrt{m}$. Smaller σ_t values, compared to those for alloy 1420, are, probably, due to the ability of copper, present in its composition, to lower the stability of the composition of oversaturated solid solutions and cause their more intensive decomposition at process heating, including welding heating [6, 7]. Welds of alloy 1460 are characterized by higher values of energy of crack initiation: J_c — 5.8–7.2, and SWCP — 5.3–6.1 J / cm^2.

Use of a concentrated heat source in plasma welding provides higher values of σ_t. Its value in welds of alloy 1420 rises to 379--428, and in welds of alloy 1460 — to 383–420 MPa. K_c value for welds of 1420 alloy increases up to 25--35, 1460 — to 31–36 MPa$\sqrt{m}$. Welds of alloy 1420 are characterized by values J_c = 7.4 J / cm^2, this being almost 2 times higher than in argon-arc welding. Values of SWCP and *KCV* also increase by not less than 30–50 %, when using plasma welding (Figure 3), this being promoted by formation of a fine-crystalline structure of welds. The thickness of the layer of crystals and intergranular spaces is 1.5 times smaller in welds made by plasma welding. Higher power of the heat source and rate of plasmatron displacement change the nature of weld metal solidification and promote development of its subdentritic structure.

Thus, higher quality characteristics of fracture toughness of welded joints on Al--Li alloys 1420 and 1460 are provided using the welding processes with a minimum heat input. The latter promotes formation of weld metal of a higher quality with a limited degree of metal softening in the HAZ and lower susceptibility of Al--Li alloys to embrittlement. A higher fracture resistance of weld metal provides a high level of performance and reliability of welded joints in structures.

In conclusion it may be noted that energy concentration and high temperature of the active heated spot of the plasma jet promotes an increase of weld penetration depth, this allowing increase of the speed of plasma welding 2 to 3 times, compared to regular argon-arc welding. High values of specific power of the constricted arc and welding speed ensure a shortening of the extent of the arc HAZ and lowering of the degree of welded joint softening.

The strength level of welded joints and metal of the weld produced by argon-arc and plasma welding under the conditions of uniaxial tension are identical. At testing for off-center tension, when the sample is simultaneously under tension and bending, the nominal fracture stress increases by 30 to 35 % only in the case of plasma welding.

The values of fracture resistance (σ_t, K_c, KCV) were determined for welded joints of Al–Li alloys, which were made by plasma welding with alternating polarity asymmetrical square wave current. Increase of the strength and fracture toughness of welds at off-center tension in plasma-welded joints provides convincing proof of the fact that application of this process in permanent joints can provide the required performance and reliability of structures from these alloys.

1. Kogut, N.S., Labur, T.M., Ishchenko, A.Ya. (1990) Crack resistance of high-strength aluminium alloys and their welded joints. *Fiziko-Khimich. Mekhanika Materialiv*, **3**, 122–123.
2. Ryazantsev, V.I. (2005) Welded structures of aluminium alloys with lithium. *Aviats. Promyshlennost*, **2**, 32--41.
3. Labur, T.M., Bondarev, Andr.A., Lozovskaya, A.V. et al. (2001) Influence of welding process on fracture resistance of joints in aluminium-lithium alloys 1420 and 1460. *The Paton Welding J.*, **7**, 11--15.
4. (1976) *Fracture*. Ed. by G. Libovits. Vol. 6: Metal fracture. Moscow: Mir.
5. (1986) *Static strength and fracture mechanics of steels*. Ed. by V. Dal, V. Anton. Moscow: Metallurgiya.
6. Fridlyander, I.N., Chuistov, K.V., Berezina, A.L. et al. (1992) *Aluminium-lithium alloys. Structure and properties*. Kiev: Naukova Dumka.
7. Rokhlin, L.L., Dobatkina, T.V., Muratova, E.V. et al. (1994) Aluminium alloys containing lithium, copper, magnesium. *Izvestiya AN SSSR. Metally*, **1**, 113–118.

SINGLE-PASS ARC WELDING OF THICK METAL USING EMBEDDED ELECTRODE

G.V. KUZMENKO[1], **V.G. KUZMENKO**[1], **V.I. GALINICH**[1], **V.V. OTROKOV**[2] and **M.A. LAKTIONOV**[2]
[1]E.O. Paton Electric Welding Institute, NASU, Kiev, Ukraine
[2]Sumy M.V. Frunze SPA, Sumy, Ukraine

Welding methods commercially applied to join heavy metal sections have been analyzed. The advantages of introducing the electrode metal into a gap prior to welding are noted, and the possibility of providing a stable arcing in gaps less than 2 mm in size is shown. It is suggested that the extra filler metal should be introduced through channels in plate electrodes to compensate for the filler metal deficit developing during weld formation. A new method is offered for automatic single-pass arc welding of heavy metal sections, called embedded-electrode electric arc welding. Technical-economic characteristics of the new welding process are compared with those of the available processes, and examples of its application for welding different grades of steels are given.

Keywords: electric arc welding, thick metal, plate electrode, narrow gap, site welding

Both single-pass (electroslag welding and arc welding with forced formation), and multipass (submerged-arc and gas-shielded) technologies are used in welding thick metal. Single-pass welding processes are characterized by a high efficiency, but quite often do not provide the required level of mechanical properties of the welded joint due to overheating of the metal of the weld and HAZ. Multipass welding processes provide a high level of mechanical properties of the welded joint, but at the expense of a significant lowering of process efficiency. The probability of formation of such defects as lacks-of-fusion and slag inclusions, is quite high. Processes of narrow-gap welding of thick metal have become developed lately. However, the required accuracy of introducing the electrode wire into the deep and narrow gap makes much more stringent requirements of welding equipment, and makes the welding technique more complicated [1–5].

In addition to the above examples of application of the known technologies for welding thick metal, many researchers also suggested engineering solutions, in which electrode metal was introduced in the form of plates into the gap before welding. Unlike the universally-accepted practices (when the electrode metal is fed in the form of wire outside the gap), such a technique offers certain advantages in terms of reducing the welding gap, simplifying the welding equipment and technique. In [6] it is suggested to introduce a plate electrode with a coating into the gap and clamp it between the edges to be welded, then strike the arc between the electrode tip and parts being welded, which, moving independently over the electrode tip should melt the entire groove. The disadvantage of this process is the absence of compensation of electrode metal deficit, which develops as the weld is formed.

For welding of metal up to 40 mm thick the «tunnel» welding process is known [7], according to which a coated consumable nozzle of an oval section is introduced into the gap, through which a steel strip is additionally fed, which compensates the deficit of electrode metal in the gap. The authors believe that this welding process is suitable for making short welds in all the positions in space, this, however, requiring additional application of forming backing and flux for shielding the welding zone.

In a US patent [8] it is proposed to perform the automatic arc welding of thick square-butt joints, using a plate electrode introduced into the groove, the electrode thickness being 2.4–7.9 mm, and the width being approximately equal to the thickness of the plates being welded. Upwards welding is performed in the vertical position. Plate electrode has a comparatively thin (0.25–1.25 mm) ceramic coating, characterized by dielectric properties. In assembly for welding the electrode with the coating completely fills the gap between the edges being welded along its entire length. To produce a weld, corresponding to the part dimensions, the electrode length should be by 10–25 % greater than that of the butt joint being made, and its feed should be performed during welding. To prevent liquid metal pouring out, the gap is closed by copper water-cooled shoes on both sides. It is proposed to apply the coating on the plate electrode by the method of dipping, spraying or applying glass fabric.

I.V. Zuev [9] suggests using a stationary consumable plate electrode of the appropriate profile for welding thick metal, which is introduced into the gap before welding. He correlates the welding modes with the values of excess pressure of molten metal vapours, velocity of sound propagation in the metal, electrode cross-section and Gruneizen dimensionless coefficient. I.V. Zuev with his colleagues [10] also studied the nature of arc displacement in arc welding of metals by a stationary consumable electrode. The disadvantages of the above process are absence of recommendations on stabilization of arcing in a narrow gap and impossibility of performing welding of extended welds

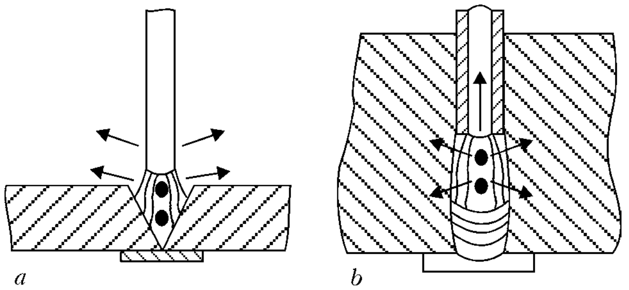

Figure 1. Schematic of arcing in an open (*a*) and closed (*b*) space of the groove

because of the electrode metal deficit developing during the groove filling.

Although the suggested welding processes have not been accepted by industry for various reasons, we believe all of them have a rational element of the use of a plate consumable electrode, pre-introduced into the gap between the edges being welded. If we assume that the welding process ensures a stable arcing and uniform-successive melting of the plate electrode with a reliable melting of the groove edges, such a welding process can be successfully used for permanent joining of metal of a considerable thickness. The plate electrode introduced into the gap, will have the function of a device assigning a certain «program» of the arc independent motion. This allows eliminating its displacement along the groove, which is used in many of the existing processes of electric arc welding. A positive factor of such a technique is the possibility of a more complete use of the arc heat due to its running in a closed space of the gap, comparable by its width with the arc column dimensions (Figure 1). This, as well as the developed cross-section of the electrode results in a high efficiency of its melting (Figure 2) [11], and, consequently, limitation of vapour formation can be anticipated, by lowering the weld pool temperature [12] compared to similar arc welding processes using a wire electrode.

The possibility of conducting the welding process with preliminary filling of the groove by electrode metal is determined by reliability of electrical insulation of the electrode from the parts being welded in the initial condition and during welding, as well as stability of arcing in a narrow gap. These conditions may be provided due to selection of the respective composition of the insulating coating, including components forming a flow of gas, vapour and slag at

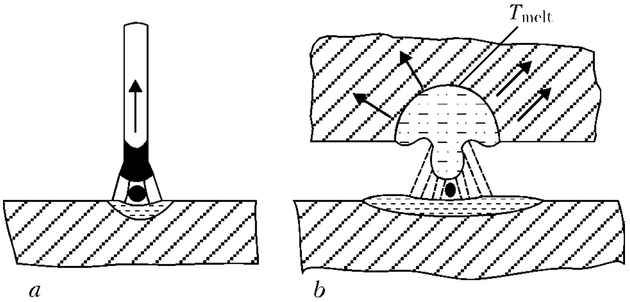

Figure 2. Schematics of melting of electrode metal when using wire (*a*) and plate (*b*) electrodes

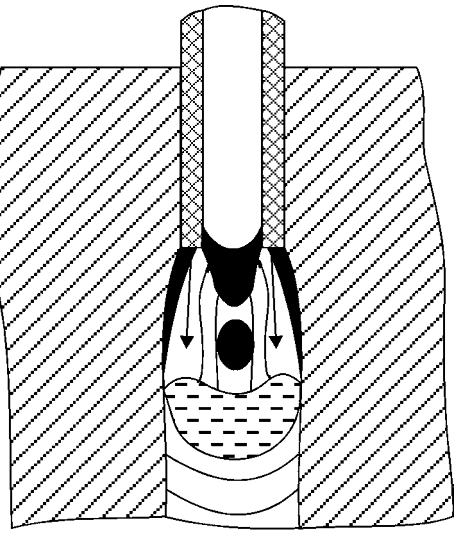

Figure 3. Schematic of stabilization and shielding of an electric arc in a narrow gap at its running at the end face of a plate insulated electrode due to the impact of gas, vapour or slag (shown by arrows)

heating, which ousts the arc from the edges being welded (Figure 3).

To evaluate the effectiveness of such a mechanism of arc stabilization, we conducted experimental welding of two plates from low-carbon steel (Figure 4). Dimensions of the surfaces being welded were equal to 100 × 150 mm, the gap being 2 mm, and 2 mm thick plate electrode was covered by a thin (0.2 mm) layer of insulating material (capacitor paper, polyterafluorinethylene) characterized by decomposition of gaseous products at heating. The electrode was clamped between the ground surfaces of the samples and connected to the welding current source of VDU-1201 type. An arc was excited between the electrode tip and plates being welded, which, moving over the electrode tip remelted it in a successive fashion.

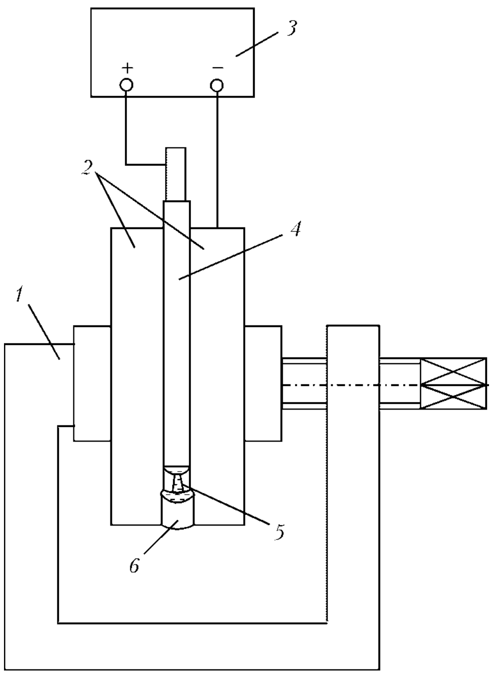

Figure 4. Schematic of butt welding of plates with 1.5 mm gap: *1* — clamp; *2* — parts being welded; *3* — current source; *4* — plate electrode; *5* — electric arc; *6* — weld

Figure 5. View of a butt joint after embedded-electrode electric arc welding (gap of 1.5 mm)

This way it was possible to obtain a welded joint (Figure 5) with a very narrow (about 2 mm) weld. However, the welded joint quality turned out to be unsatisfactory, because of the limited capabilities of metallurgical action on the weld metal. It was not possible to eliminate weld porosity or hydrogenation, using the above insulating materials. In addition, even in the case of application of a very thin coating, electrode metal deficit invariably increased in the gap as the electrode was melted, resulting in defects in the form of cavities or lacks-of-fusion in the weld metal. Therefore, the thickness of electrode core was further increased to 4--6 mm, this allowing making longitudinal channels in it for feeding additional electrode metal. A ceramic coating 0.8–1.5 mm thick was used as the insulating material, with oxides, fluorides and carbonates, as well as the required deoxidizers, added to it in the required proportion. This allowed simplifying the requirements to the quality of edge preparation and fit-up, ensuring a reliable insulation of the electrode and actively influencing the metallurgical processes in the weld pool.

The above published data and results of our research allowed suggesting a new method of single-pass narrow-gap arc welding, which was called embedded-electrode electric arc welding (Figure 6) [13, 14].

The essence of this welding process is as follows. The parts to be welded without edge preparation are assembled with a certain gap, into which an insulated consumable electrode with a core in the form of a plate of the width equal to the part thickness, is introduced. The core has longitudinal channels, through which filler wires or strips are fed during welding to compensate for metal deficit. The groove to welded up is closed by forming coverplates on both sides. The arc is excited at the lower tip of the embedded electrode and moving over its end face, runs in a space, limited by the edges of the parts being welded and forming coverplates surfaces. Under the impact of the heat generated by the arc, heating and melting of the electrode, filler metal and edges of parts being welded occurs, which results in formation of a weld. Despite an erratic displacement over the electrode tip, the arc provides its stable and uniform heating (Figure 7).

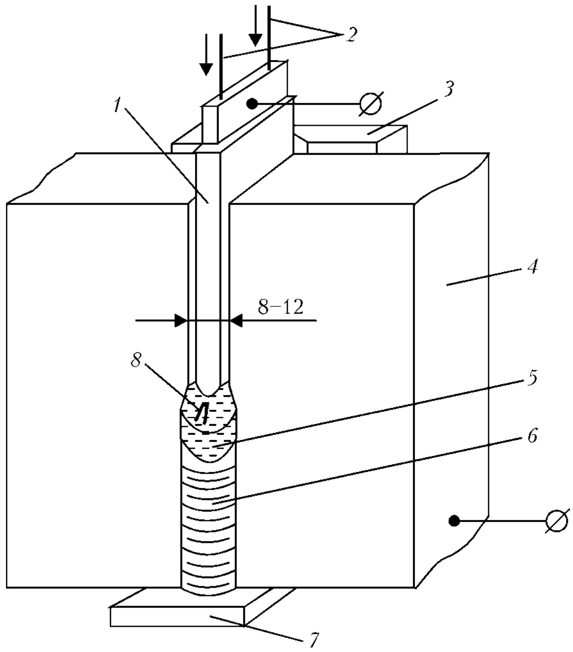

Figure 6. Schematic of embedded-electrode electric arc welding: *1* — embedded electrode; *2* — filler wire; *3* — forming backing; *4* — item welded; *5* — weld pool; *6* — weld; *7* — backing; *8* — arc

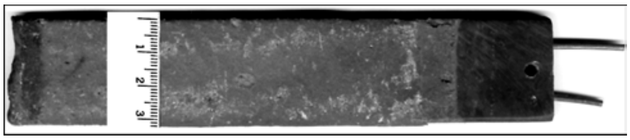

Figure 7. View of surface-melted end face of embedded electrode in arc welding of 30 mm metal (thickness of electrode metal part — 6 mm, coating — 1.2 mm)

This effect can be explained, proceeding from Steenbeck principle [15], according to which, the arc mainly runs in those regions, where conditions are in place for its functioning at minimum voltage. One of the main factors stimulating arc displacement over the electrode tip, is increase of the distance between the electrode tip and the weld pool as a result of electrode melting.

Table 1. Comparative indices of various welding processes

Parameter	Embedded-electrode arc welding	Electroslag welding	Arc welding with forced formation
Metal thickness, mm	20–100	20–200	12–60
Gap, mm	8–12	20–40	12–25
Voltage, V	24–30	36–55	28–48
Welding current, A	400–1000	400–1200	300–700
Welding speed, m / h	2–8	0.5–2.2	1–7
Specific welding time, s / cm^2	1–5	2.3--20	2.4–13
Specific energy content, kJ / cm^2	25–50	100–400	40–150
Specific material content, g / cm^2	6.3–9.4	15.7–31.4	9.4–19.6

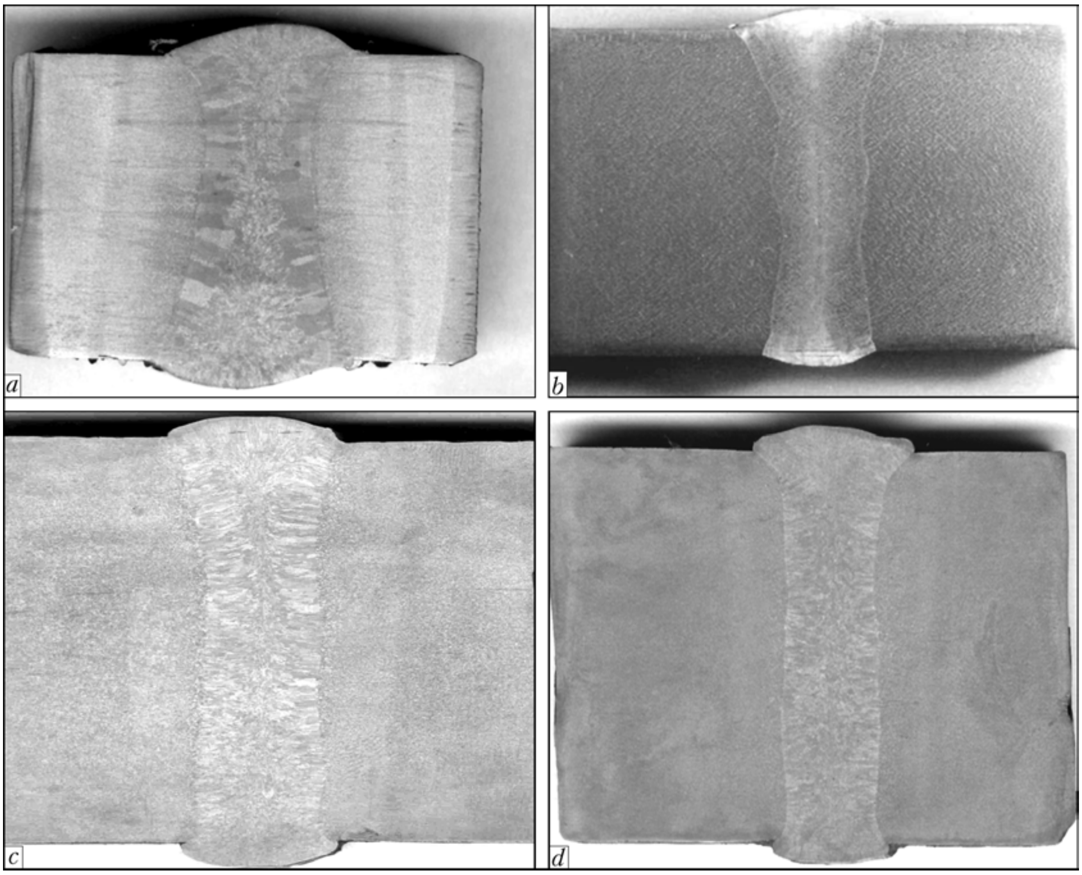

Figure 8. Macrosections of joints produced by embedded-electrode arc welding (single-pass) on 10KhSND steel 30 mm thick (*a*), 08Kh17N13M2T steel 38 mm thick (*b*), 09G2S steel 60 mm thick (*c*) and St3sp 60 mm thick (*d*)

With this welding process, the gap between the edges is equal to 8–12 mm at part thickness of 20–100 mm due to application of an embedded plate electrode, this providing a sufficiently high process efficiency (total coefficient of melting of the electrode and filler metal is equal to 22 g / (A·h)) and moderate

Table 2. Composition and mechanical properties (average values) of the metal of weld on different steel types

Steel grade (thickness, mm)	Fraction of elements, wt.%						
	C	Si	Mn	Cr	Ni	Mo	Cu
10KhSND (20)	0.08	0.52	1.14	0.32	1.10	0.41	0.28
10KhSND (30)	0.09	0.44	1.19	0.29	1.21	0.46	0.26
St3sp (30)	0.13	0.37	0.98	0.11	0.07	0.04	–
St3sp (50)	0.11	0.35	0.92	0.09	0.12	0.07	–
09G2S (60)	0.09	0.52	1.69	0.24	0.09	0.21	–
08Kh17N13M2T (38)	0.04	0.82	0.97	19.00	12.10	1.86	–

Table 2 (cont.)

Steel grade (thickness, mm)	Mechanical properties of weld metal (average values)						
	σ_y, MPa	σ_t, MPa	δ_5, %	*KCU*, J / cm^2		*KCV*, J / cm^2	
				– 40 îÑ	– 60 îÑ	+ 20 îÑ	– 20 îÑ
10KhSND (20)	415	585	28	–	–	126	82
10KhSND (30)	410	590	27	–	–	105	78
St3sp (30)	365	490	29	78	–	–	–
St3sp (50)	362	485	39	86	–	–	–
09G2S (60)	390	570	28	101	75	–	–
08Kh17N13M2T (38)	320	565	38	–	> 360	–	–

specific heat input (25--50 kJ / cm^2). Table 1 gives the indices of the new welding process.

We tried out embedded-electrode electric arc welding in joining samples from low-carbon (St.3), low-alloyed (09G2S, 10KhSND, 16G2AF) and high-alloyed corrosion-resistant (08Kh18N10T, 0817N13M2T) steels 20 to 100 mm thick. Experiments showed that the suggested welding process features a high reliability and allows making welds on steels of the studied thickness practically without defects such as cracks, lacks-of-fusion, pores and slag inclusions (Figure 8).

The welds have mechanical properties not inferior to those of the base metal. Even at the testing temperature of –60 °C the metal of a weld made on low-alloyed steels, is characterized by a high (70–80 J / cm^2) impact toughness, despite the minimum alloying level (Table 2).

In our opinion embedded-electrode arc welding will become widely applied in fabrication of thick-walled (20--100 mm) welded structures with relatively short (up to 1000 mm) welds due to their cost-effectiveness and simplicity of the used equipment. It can become an alternative to the traditional welding processes.

CONCLUSIONS

1. A new process of embedded-electrode automatic single-pass arc welding of 20–100 mm thick metal is proposed, which is conducted in the vertical position of the parts being welded and is mainly designed for welding short (up to 1000 mm) welds, also in site.

2. Application of a plate consumable electrode with an insulating coating allows reducing the gap between the parts being welded to 8--12 mm, which results in a considerable improvement of the technical-economic indices of the process of metal welding.

3. Compensation of electrode metal deficit in welding can be ensured both by a gradual (as it melts) feeding of a plate electrode to the weld pool, and entering wires or plates through its channels.

4. Correspondence of the dimensions of insulated plate electrode to the gap dimensions and features of arcing (Steenback principle) at the plate electrode tip determine the «program» of its independent displacement in a narrow gap, providing a uniform melting of the edges of the parts being welded and formation of a tight weld. It eliminates the need for application of special devices for electrode displacement along the butt and considerably simplifies the used equipment.

1. Serenko, A.N., Patrikeev, A.O., Shaferovsky, V.A. et al. (1985) Technical-economical comparison of different welding methods of metal plates. *Svarochn. Proizvodstvo*, **12**, 3–5.
2. (1980) *Electroslag welding and cladding*. Ed. by B.E. Paton. Moscow: Mashinostroenie.
3. Lebedev, V.K., Kakhovsky, N.I., Savchenko, V.S. et al. (1977) Shielded-gas welding of low-carbon high-strength steel joints into narrow groove. *Avtomatich. Svarka*, **5**, 1–5.
4. Kasatkin, B.S., Tsaryuk, A.K., Levenberg, N.E. et al. (1984) Technological features of submerged-arc narrow-gap welding of large thick medium-alloy steels. *Ibid.*, **7**, 41--44.
5. Tereshchenko, V.I., Libanov, A.V. (1987) *Selection and application of welding methods in manufacturing of structures*. Kiev: Naukova Dumka.
6. Pashenko, F.F. *Method of electric arc welding*. USSR author's cert. 53628. Int. Cl. B 23 K 09 / 09. Fill. 16.06.37. Publ. 31.08.38.
7. Iio, K., Osakato, A., Kobayashi, K. et al. (1974) Development of a new method of tunnel arc welding. *Kobe Steel Eng. Repts.*, 24(**3**), 93–99.
8. Cable, H.E. *Electrodes for welding and the like*. Pat. 3646312 USA. Int. Cl. B 23 K 35 / 22. Publ. 29.02.72.
9. Zuev, I.V. *Method of electric arc welding of intricate shape products and device for its realization*. Pat. 2115521 RF. Int. Cl. B 23 K 9 / 173 9 / 10. Publ. 20.07.98.
10. Zuev, I.V., Kubarev, V.F., Bushma, V.O. et al. (1994) Narrow-gap arc movement in a stationary consumable electrode arc welding of metals. *Tekhnologiya. Prikladn. Fizika*, **3**, 3–7.
11. Razmyshlyaev, A.D., Bagryansky, K.V., Nesterenko, K.A. (1972) Heat content of drops in arc surfacing. *Svarochn. Proizvodstvo*, **5**, 15–16.
12. Malikin, V.L., Frumin, I.I. (1977) Mean temperature of weld pool in submerged-arc surfacing by strip electrode. *Avtomatich. Svarka*, **6**, 25–28.
13. Kuzmenko, V.G., Kuzmenko, G.V. *Method of consumable electrode arc welding and electrode for its realization*. Pat. 2219021 RF. Int. Cl. B 32 K 9.14, 35 / 36. Publ. 20.12.2003.
14. Kuzmenko, V.G., Kuzmenko, G.V. *Method of consumable electrode arc welding and electrode for its realization*. Pat. 68361 Ukraine. Int. Cl. B 23 K 9 / 2. Publ. 16.08.2004.
15. Leskov, G.I. (1970) *Electric welding arc*. Moscow: Mashinostroenie.

IMPROVEMENT OF QUALITY OF DEPOSITED METAL IN PLASMA-MIG CLADDING OF ALUMINIUM ALLOYS

V.V. CHIGAREV, K.A. KONDRASHOV and **N.A. GRANOVSKY**
Priazovsky State Technical University, Mariupol, Ukraine

Peculiarities of plasma-MIG cladding of aluminium alloys are considered. The cause of formation of oxide-type non-metallic inclusions in the deposited metal was found to be an oxide film on the surface of metal electrode. Suggested is the diagram of the plasma-MIG cladding machine operating in the pulsed mode, allowing removal of oxide film from the metal electrode surface. The results obtained show that it is possible to dramatically decrease the quantity of non-metallic inclusions in the deposited metal.

Keywords: plasma-MIG cladding, aluminium alloys, non-metallic inclusions

The processes of plasma welding [1] and cladding find an increasingly wide application in manufacturing. One of the rapidly developing methods of plasma cladding is plasma-MIG cladding, possessing wide technological capabilities and high productivity, which is attributable to intensive heating of metal electrode inside a plasmatron [2]. Specialised equipment was developed for the plasma-MIG welding and cladding processes [3].

Plasma-MIG cladding holds promise for parts of wrought and cast aluminium-base alloys [4]. This process is particularly efficient for rejuvenation of massive parts with a large amount of deposited metal. However, as proved by investigations, the latter contains non-metallic inclusions of an oxide character, having a negative effect on performance of the deposited metal [5]. Therefore, the demand is to improve quality of the deposited metal in plasma-MIG cladding of aluminium alloys by decreasing its content of oxide-type non-metallic inclusions.

The purpose of the study was to reveal the causes of oxide inclusions formed in the deposited metal during the plasma-MIG cladding process, and develop methods for removing them. In MIG welding of aluminium, as a droplet transfers through the arc gap, its surface may be oxidised. This makes requirements to gas shielding of the welding zone more stringent. To meet the requirements, super-pure argon was used as plasma and shielding gas, and plasmatron PMNA-3 developed by the Priazovsky State Technical University was additionally equipped with a protective nozzle 80 mm in diameter, having reticular gas lenses. However, this failed to markedly reduce the quantity of oxide inclusions in the deposited metal, which allowed a conclusion that the inclusions get into the weld pool mostly from the metal electrode surface.

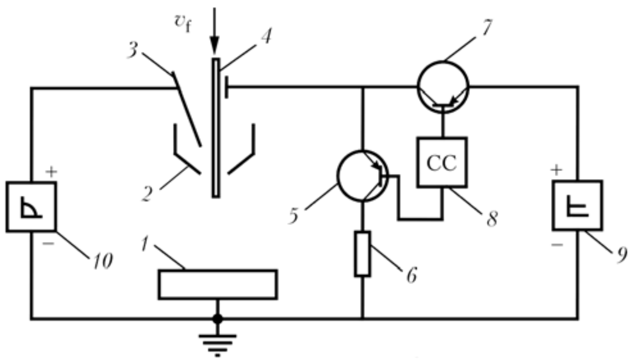

Figure 1. Diagram of plasma-MIG cladding machine: *1* — workpiece; *2* — plasmatron nozzle; *3, 4* — metal and tungsten electrodes; *5, 7* — power transistors; *6* — ballast resistor; *8* — power transistor control circuit; *9, 10* — plasma arc and metal electrode power sources, respectively

This is attributable to the fact that cladding of aluminium is performed, as a rule, at the direct current of reverse polarity. A workpiece in this case is a cathode. Therefore, the oxide film from its surface is readily removed due to the cathode sputtering effect. Both metal and tungsten electrodes are anodes, this making it impossible to remove the oxide film from the metal electrode surface. In melting of metal electrode, the oxide film transfers into the weld pool to form inclusions of the oxide character during solidification.

To ensure removal of oxide film from the metal electrode surface directly during the cladding process, the Chair of Welding Metallurgy and Technology of the Priazovsky State Technical University developed a machine for plasma-MIG cladding (Figure 1). As seen from the Figure, two power transistors *5* and *7* are included into the power circuit of the metal electrode arc, the control loops of which are connected to the control circuit that alternately opens the transistors. When one of them is opened, the other is closed (control of the transistors is antiphase). When transistor *7* is opened, the metal electrode is connected to power source *9*, and the «metal electrode–workpiece» arc is ignited. In the shown diagram of operation of the machine (Figure 2), this process corresponds to time t_1. At time moment t_2 transistor *7* is closed, and transistor *5* is opened, the metal electrode being connected through ballast resistor *6* to workpiece *1*, i.e. it becomes a cathode with respect to the tungsten electrode. This causes ignition of the arc in the «tungsten electrode–metal electrode» region. The arc current is determined by resistor *6*. Cathode cleaning of the metal electrode surface takes place at this time moment (t_2).

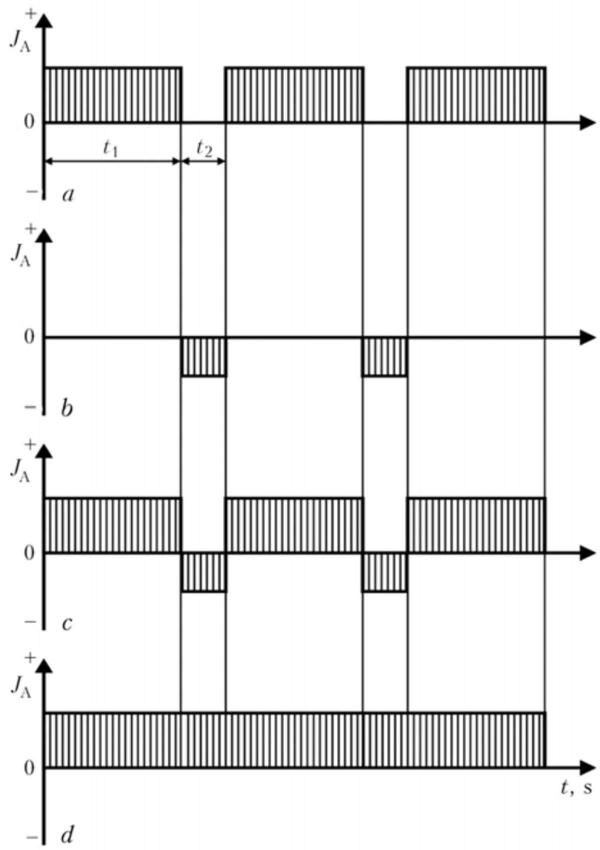

Figure 2. Diagram of operation of the machine: *a*, *b* — currents of transistors *7* and *5*, respectively; *c*, *d* — currents of metal and tungsten electrodes, respectively

Data given in study [6] show that the antiphase pulse current with a duration of the straight-polarity current pulses equal to 19 ms and that of the reverse-polarity current pulses equal to 3 ms can be applied for efficient cathode cleaning of aluminium workpieces. These data were taken as a basis.

Cladding was done on the electric aluminium plates 12 mm thick using wire of the SvAK5 grade, 1.6 mm in diameter, under the following conditions:

metal electrode arc current, A	240
metal electrode arc voltage, V	22
plasma arc current, A	125
plasma arc voltage, V	38
nozzle channel diameter, mm	6
welding speed, m / h	18
plasma gas flow rate, l / min	8.8
shielding gas flow rate, l / min	52
time t_1, ms	19
time t_2, ms	3
current at time moment t_2, A	30

The metal and tungsten electrode currents were measured using electron oscillographs. Because the metal electrode is immersed into the plasma arc column, no extra actions to repeatedly ignite the arc after completion of pulse trains t_1 and t_2 are required. The arc is reliably ignited at the beginning of each of the time modes t_1 and t_2.

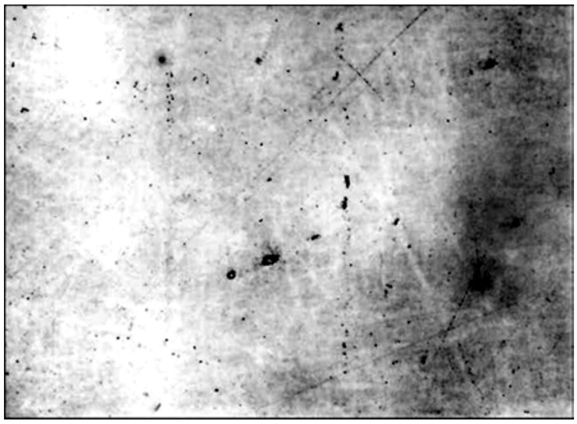

Figure 3. Microstructure of deposited metal containing non-metallic inclusions (×200) produced by using the standard modification of plasmatron PMNA-3 (without increased shielding gas nozzle). Cladding mode — continuous

To assess the cathode cleaning zone on the surface of metal electrode, the nozzle to feed the latter was removed from the plasmatron, and replaced by the plug with a 3.0 × 1.6 mm aluminium bus fixed in it. The bus passed via the entire channel of the nozzle and projected from it for 3 mm. Power source *9* of the metal electrode arc was turned off. Control circuit *8* was actuated after ignition of the plasma arc. After it counted 50 pulses fed to transistor *5*, the circuit was automatically disconnected to turn off the machine. After that the plug with the aluminium bus fixed in it was removed and examined to assess the efficiency of cathode cleaning on the basis of the cleaned metal surface area. The quantity of non-metallic inclusions was determined by metallographic examination of 1 cm^2 microsections cut from the deposited metal (Figure 3).

The drawbacks characteristic of the arc burning mode of 19 ms and arc burning pause of 3 ms were revealed by using the one-phase power source developed by the Priazovsky State Technical University, having a common power transformer with separate secondary windings to power the plasma and metal electrode arcs. This work cycle results in the formation of a constant component in the transformer winding that powers the metal electrode arc. This component causes superposed magnetisation of the transformer core and violates the normal cladding process, resulting in characteristic vibrations of the power transformer. The latter are caused by the fact that time of one half-cycle of the alternating current is 10 ms, whereas the cycle time of the current consumed by the metal electrode arc from the power source is $T = t_1 + t_2 = 19 + 3 = 22$ ms. Hence, one half-cycle of the supply current is completely utilised, whereas the other has a pause of 3 ms, thus leading to the formation

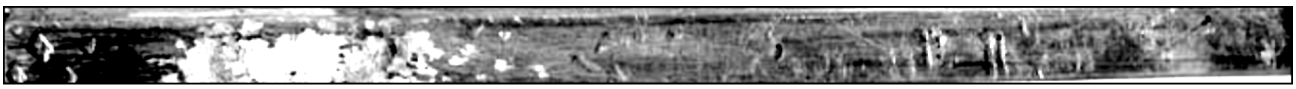

Figure 4. Aluminium bus sample after testing inside the plasmatron

Effect of cycle parameters t_1 and t_2 on the process of cleaning the surface of a bus sample inside the plasmatron, and quantity of non-metallic inclusions in the deposited metal

Values of t_1 and t_2, ms	Cleaned area on bus surface inside plasmatron, mm^2	Quantity of non-metallic inclusions per 1 cm^2 section of deposited metal, pcs
$t_1 = \infty$, $t_2 = 0$	0	17–23
$t_1 = 19$, $t_2 = 3$	9–12	3–6
$t_1 = 7$, $t_2 = 3$	14–17	0–2

of a constant component in the power transformer winding powering the metal electrode arc.

As a result, the work cycle of the machine was changed. Time of the current of metal electrode arc *4* flowing through power transformer *7* was reduced to 7 ms (the 3 ms pause time being retained). This change provided a stable cladding process with a simultaneous decrease in quantity of non-metallic inclusions contained in the deposited metal and increase in the cleaned area on the bus sample surface (Figure 4) inside the plasmatron (Table).

The optimal phase of beginning of cycle time t_2 was found to range from 20 to 70 electrical degrees. It is under these conditions that the deposited metal contains practically no non-metallic inclusions of the oxide character, and the cladding process is characterised by the best stability.

Continuation of research aimed at optimisation of pulse modes of plasma-MIG cladding of aluminium alloys holds much promise, as this will allow improvement of quality of the deposited metal and rise in deposition efficiency by additionally heating the metal electrode with the «tungsten electrode–metal electrode» arc.

CONCLUSIONS

1. In plasma-MIG cladding of aluminium alloys, oxides present on the surface of electrode wire are the main source of oxide-type non-metallic inclusions in the deposited metal.

2. The pulsed mode of the metal electrode arc, where the metal electrode periodically becomes a cathode with respect to the tungsten electrode, allows removal of oxide film from the metal electrode surface, and reduction of quantity of non-metallic inclusions in the deposited metal.

3. The optimal proportion of time of the metal electrode arc and time of cathode cleaning of the metal electrode surface is 7 and 3 ms, which makes it possible to remove as much oxides as possible from the metal electrode surface, and use the one-phase rectifier as a power source.

4. In the case of using the one-phase rectifier, the optimal phase of beginning of cathode cleaning is 20–70 electrical degrees.

1. Makarenko, N.A., Gvozdetsky, V.S. (2000) Plasma welding. *Avtomatich. Svarka*, **12**, 26–30.
2. Chigarev, V.V., Makarenko, N.A., Kondrashov, K.A. et al. (2001) Features of electrode wire melting in surfacing by plasma-MIG process. *The Paton Welding J.*, **8**, 10–12.
3. Kornienko, A.N., Makarenko, N.A., Kondrashov, K.A. et al. (2001) Versatile unit for plasma-MIG welding and cladding. *Svarochn. Proizvodstvo*, **9**, 30–31.
4. Shevers, A. (1997) Plasma-MIG lassen van aluminium kanvordelen bieden voven MIG lassen. *Bedrijf en Techn.*, 11(**98**), 140–142.
5. Kiselyov, S.N., Khavanov, V.A., Roshchin, V.V. et al. (1972) *Gas-arc welding of aluminium alloys*. Moscow: Mashinostroenie.
6. Mlakhovsky, V.A. (1974) *Plasma welding*. Moscow: Vysshaya Shkola.

NEW METHOD OF QUANTITATIVE DETERMINATION OF SUSCEPTIBILITY OF STRUCTURAL STEELS TO HYDROGEN EMBRITTLEMENT

The method is based on use of a physically-grounded quantitative criterion of hydrogen effect. Smooth cylindrical samples (without notch), which are deformed by a uniaxial tension in the preset interval of temperatures, are used in a realization of this method. Criterion of embrittlement is defined as a ratio of values of a mean stress of metal fracture in hydrogen-induced and initial states with account for a ratio of deformation in sample and curvature of a neck at the moment of fracture. There is a positive decision of Patent Agency of Russia of 28.09.92 on Application No.5040067 «Method of Quantitative Determination of Degree of Hydrogen Embrittlement of Structural Steels and Welds» Int. Cl. Go1n 17.00.

Purpose. Method is designed for determination of degree of embrittlement effect of hydrogen, absorbed by metal in steel melting, in manufacture of welded structures and in the process of service of steel products under the conditions of hydrogenation from surrounding or technological environment.

Application. This method can be used in metallurgy, welding industry, in the development of challenging welding consumables, service and repair of steel products.

Contacts: Prof. Pokhodnya I.K.
E-mail: pokhod@paton.kiev.ua

MAGNETIC CONTROL OF LOW-TEMPERATURE PLASMA FLOWS IN THE PROCESSES OF THERMAL SPRAYING OF COATINGS

V.N. PASHCHENKO and **S.P. SOLODKY**
NTUU «Kiev Polytechnic Institute», Kiev, Ukraine

The possibility of controlling the position of a low-temperature plasma jet by superposition of a transverse magnetic field on the initial section of the plasma flow was studied. It is established that the main parameters influencing the angle of the jet deviation, are the controlling electric magnet current and specific energy of the plasma jet. It is shown that the direction of plasma flow deviation depends on the directions of the magnetic flow in the zone of interaction and direction of the gas flow swirling.

Keywords: thermal spraying of coatings, low-temperature plasma, plasma flow, magnetic control, plasma jet, angle of deviation

Low-temperature plasma flows are widely used in surface engineering technologies, namely in surfacing, spraying, quenching, etc. A rational organization of the above technological processes is impossible without operational control of the position of the working medium relative to the processed object.

The problem of the relative position of phases (gaseous and solid) in the heterophase flow in thermal spraying of coatings is particularly urgent. Gas dynamic and mechanical methods of forming the required initial structure of the gas-powder flow are mostly used now, namely powder feeding through a system of channels, manipulation of the transporting gas parameters, variation of the point and direction of feeding the disperse material, blowing off or suction of the main carrier jet by a flow of additional substance, etc. [1].

On the other hand, presence in the high-temperature gas flow of a certain (often quite considerable) amount of moving charged particles allows (in theory) using electromagnetic fields for correction of their motion. The latter are quite widely used in the welding processes to control objects, through which the electric current flows. Work in the above direction is being conducted at the E.O. Paton Electric Welding Institute and NTUU «Kiev Polytechnic Institute».

Low-temperature plasma flows can be a new area of magnetic control application.

Content of charged particles in the volume of the high-temperature gas, in particular, of the plasma jet, depends on the achieved temperatures. Under the actual conditions temperature distribution across the section of the low-temperature plasma flow is non-uniform.

Temperature on the plasma jet axis is, as a rule, several times higher than its weight-average temperature. At weight-average temperature of the jet of 2000–4000 K, the temperature in the near-axis zone can be equal to $(9–20)\cdot10^3$ K [2].

This is indirectly confirmed by the results of measurement of distribution of temperature and enthalpies across the section of plasma jets of air and mixture of air with hydrocarbon gases [3]. According to the conducted temperature measurements the temperature on the plasma jet axis is equal to $(3.5–4.0)\cdot10^3$ K at 40 mm distance, and the nature of temperature dependence on the distance measured from the plasmatron nozzle edge leads to the conclusion that the axial temperature will be equal to $(9–12)\cdot10^3$ K.

Such a level of temperature is associated with the presence of a considerable amount of ionized components of the plasma gas within the initial section of the plasma jet. Thermodynamic calculations of the dependence of the composition of air plasma and plasma of the combustion products of hydrocarbon gases on temperature [4] are indicative of an essential increase of the electron gas content at the temperature above 7000 K. For instance, at 9000 K it is equal to 1 vol.%, and at 12000 K to 12 vol.%. The content of positive singly ionized N^+, O^+ ions (air plasma), and C^+, H^+, N^+, O^+ ions (plasma of a mixture of air with hydrocarbon gases) increases at the same time.

Presence of moving charged components of the plasma medium creates the prerequisites for using the magnetic fields to control the trajectory of motion of a certain part of the low-temperature plasma flow, and through it — for correction of the position of the entire plasma jet in space.

Investigation of the influence of the magnetic field on the low-temperature plasma flows were conducted in an experimental set-up, consisting of a low-temperature plasma generator and magnet system, combined with the nozzle part of the plasmatron (Figure 1).

Experiments were conducted in an arc plasma generator with a linear circuit with eddy feed of the plasma gas and self-gas-dynamic stabilization of the arc length using air or a mixture of air with hydrocarbon gases as the plasma gas. Arc current was varied in the range of 130 to 200 A at the total power of the plasmatron of 18 to 22 kW. Plasma gas consumption was 3.5–5.0 m^3 / h.

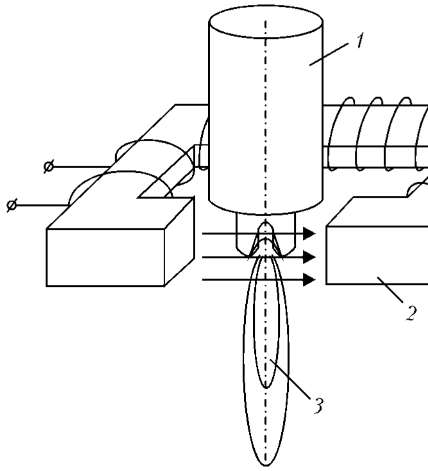

Figure 1. Layout of generating and controlling systems of experimental set-up: *1* — plasmatron; *2* — electric magnet; *3* — object of control (jet of low-temperature non-current-conducting plasma)

Controlling magnetic system consisted of a DC electric magnet in the form of a coil wound by copper wire on a Π-shaped ferromagnetic core. The electric magnet is rigidly fixed relative to the nozzle system of the plasmatron so that the initial section of the plasma jet were between the electric magnet poles.

The flow direction and value of magnetic induction were assigned proceeding from the direction of current, its value in the coil and were varied by an assigned cyclogram, using a system of electric magnet control. The plasma jet position in space was recorded by a digital video camera with automatic adjustment of brightness.

Current in the electric magnet $I_{e.m}$, arc current I_a and plasma gas pressure $p_{p.g}$ were used as the variable parameters. Range of variation of these parameters during the experiment was determined by the following factors: capabilities of the magnetic system — $5 < I_{e.m} \leq 15$ A; admissible current of the plasmatron thermochemical cathode (upper limit) and power source capabilities (lower limit) — $130 \leq I_a \leq 200$ A; conditions of stable arcing within the arc channel dependent on the plasma gas flow rate (2.5 m^3 / h — lower limit, corresponding to the arc drawing into the narrow part of the arc channel, and 5 m^3 / h — upper limit, corresponding to the arc carrying out beyond the channel). Change of the flow rate during result processing was matched to the change of the plasma gas pressure in the range of $0.3 \leq p_{p.g} \leq 0.5$ MPa.

Processing of measurement results (digital photos of the plasma flow) was conducted using an applied program package Photoshop 7 by superposition of several images and measurement of the angle of deflection of the plasma flow axis under the action of the magnetic field relative to the plasma flow axis in the absence of the field.

Figure 2, *a* shows an image of a plasmatron jet under the impact of the magnetic field with a fixed direction of magnetic induction. Change of the direction of current in the controlling system electric magnet leads to deviation of the plasmatron jet to the opposite side, practically to the same angle (Figure 2, *b*). Figure 2, *c* shows the result of superposition of three images in the absence and in the presence of a field of different polarity.

Angle of plasma jet deviation α (to one side from the initial position) increased with increase of current in the electric magnet and arc current, and decreased at increase of the plasma gas flow rate (Figure 3).

Increase of electric magnet current leads to an increase of magnetic induction in the interaction zone also in keeping with Lorents formula, increase of the force acting on a charged moving particle.

Increase of arc current or reduction of the plasma gas flow (as well as their simultaneous change) at unchanged other parameters, increases the specific power per a unit of the plasma gas volume. The associated increase of plasma temperature increases the content of the charged particles and their motion velocity, and, hence, the effectiveness of the magnetic field impact on the plasma flow.

In the studied range of plasma operating parameter variation, the total angle of plasma jet deviation (to both sides from the middle position) is equal to 11–12°.

Approximation of the obtained experimental curves yielded an empirical dependence of angle a of deviation of the plasma jet from the above operating parameters of the plasma generator in the studied ranges:

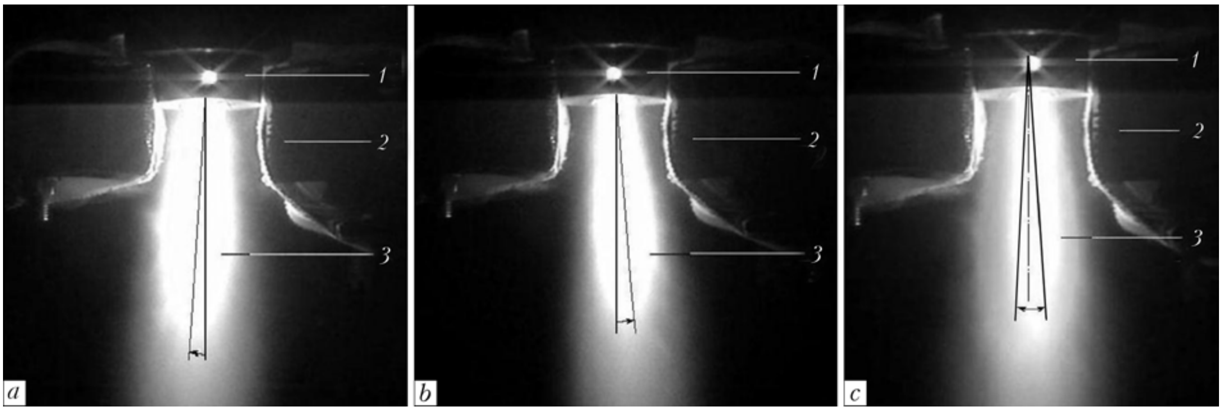

Figure 2. Combined images of air plasma jet in the absence of magnetic impact and in its presence: *a*, *b* — direction of magnetic induction from right to left and from left to right, respectively; *c* — alternative changing of direct current in the controlling magnet; *1* — plasmatron output electrode; *2* — electromagnet poles; *3* — plasma jet

$$\alpha = 0.886\,\frac{(I_{\rm e.m})^{0.41}(I_{\rm a} - 116.6)^{0.175}}{(27.14p_{\rm p.g} - 7.14)^{0.24}}.$$

In view of the complexity and multifactorial nature of the processes running at magnetic impact on the swirling gas flow, it is difficult to have a complete physical pattern of the nature of motion of the gas flow particles (including neutral particles). Further studies are required of the plasma jet behaviour in a transverse magnetic field at different values of the gas flow swirling, allowing for the relative position of the magnetic system and current-carrying sections of the arc column, the results of which will allow revealing the nature of experimentally established facts.

Experimental confirmation of the possibility of magnetic control of the spatial position of the plasma jet, alongside the alternative control methods opens up additional prospects for organizing, for instance, the processes of modification of the surface layers of products or deposition of plasma coatings, including those of a complex macrostructure.

CONCLUSIONS

1. Application of a transverse magnetic field on the plasma jet leads to deviation of the direction of gas flow motion.

2. Angle of plasma jet deviation is determined by the operating parameters of the plasma generator and controlling magnetic system and is equal to 5–6°.

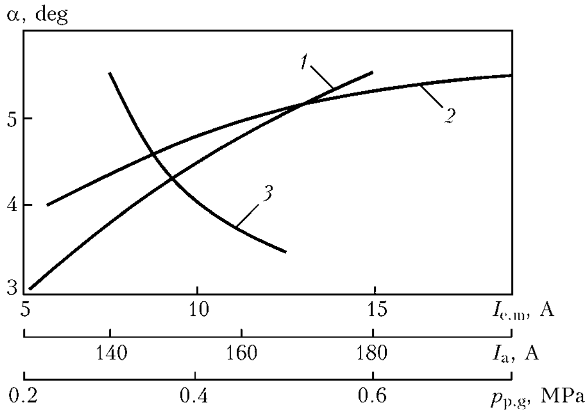

Figure 3. Dependence of the angle of plasma jet deviation on the parameters of electric magnet current (*1*), arc current (*2*) and pressure of plasma air (*3*)

3. Spatial orientation of a plane, in which deviation of the plasma jet is observed, depends on the directions of the magnetic flow and gas flow swirling.

1. Pashchenko, V.M. (2001) *Equipment for thermal spraying of coatings*. Manual. Kiev: IVTs Politekhnika.
2. Suris, A.L. (1989) *Plasma-chemical processes and apparatuses*. Moscow: Khimiya.
3. Pashchenko, V.M., Solodky, S.P. (2005) Study of influence of geometric and condition parameters of plasmatrons with a combined power supply on temperature and velocity fields of plasma jet. *Naukovi Visti NTUU KPI*, 2(**40**), 72–79.
4. Karp, I.N., Martsevoj, E.P., Pashchenko, V.N. (1985) Mathematical modeling of heating and particle motion in plasma jet. *Khim. Tekhnologiya*, **6**, 27–33.

PATENTS IN THE FIELD OF WELDING PRODUCTION*

Torch for arc welding in shielding gases characterized by that it additionally contains a mechanism for electrode wire feeding in the form of a feeding head and electric motor with a hollow shaft, installed in the central part of carrying element of the case — longitudinal current supplying bar, on the ends of which the front and rear flanges are fastened. Other features of the torch are also given. Patent of Ukraine 74709. B.I. Martynenko, S.M. Sverchkov, F.M. Didenko et al. (Company «Ukrainian RDI of Machine-Building Technologies») [1].

Device for welding position butt joints characterized by that it additionally includes the feeding head and special trough that are installed on the faceplate that provide precision wire feed to the welding zone, the filler wire feed mechanism incorporating a cassette with wire, electric motor with a hollow shaft and flexible hollow shaft, connected to the feeding head. Patent of Ukraine 74658. B.I. Martynenko, S.M. Sverchkov, F.M. Didenko et al. (Idem) [1].

Method of thermal cutting of metal sheets characterized by that the plasma cutting torch is shifted, using a gantry and carriage up to matching of plasma cutting torch axis with the center of cut out hole and after the gantry and carriage drives are stopped, plasma cutting torch is moved into horizontal direction relative to the carriage to a distance equal to the radius of the cut out hole, after that plasma cutting torch is rotated around vertical axis, that passes through the center of cut out hole, and when plasma cutter is switched on, a round hole is cut. Declaration Patent of Ukraine 11843. V.A. Najdorf (Experimental Plant of Technological Equipment «Nikkom» Company) [1].

Machine for thermal cutting of metal sheets characterized by that it is equipped with the means for linear horizontal transfer of plasma cutting torch relative to the carriage and its rotation around a vertical axis. Declaration Patent of Ukraine 11849. V.A. Najdorf (Idem) [1].

Device for joint formation at resistance butt welding of a pipe with a plug characterized by that part of yoke insulating element, that consists of insulation and metal elements, is placed between the current supply and circumferential stop-cooler, and the thickness of the section of inside diameter of circumferential metal element of the yoke has a value that is equal to the sum of the thickness of one plate of the circumferential stop-cooler and the extent of pipe end face penetration into the middle of the section of yoke metal element. Declaration Patent of Ukraine 12191. N.A. Lavrentiev, V.S. Krasnorutsky (NNTs «Kharkov Physical-Technical Institute») [1].

*The given information about patents of Ukraine was published in official bulletin «Promyslova Vlasnist» for 2006 (the number of bulletin in given in square brackets).

Installation for laser welding of pipelines characterized by that the welding head, laser or, at least, the laser radiator are mechanically connected to each other and manufactured with the possibility of being placed inside the pipeline, and each seat in the load magazine is equipped with the rod for service lines supply, at which end the mechanism for connecting and disconnecting the service lines to laser and welding head inside the welded pipe is mounted. Declaration Patent of Ukraine 12315. I.Yu. Novikova (Company «KEMZ Welding») [1].

Flash remover characterized by that it has a built-in shielding device in the direction of the metal passage next to the first support roller, screen and open box with an inclined bottom and unequal side walls. Other distinctive features are also listed. Declaration Patent of Ukraine 12216. S.A. Gritsenko, Yu.V. Sus, I.A. Evginenko et al. (Company «Novokramatorsk Machine-Building Plant») [1].

Electric welding unit containing the first power source with the first output, creating the primary output alternating current between the electrode and welded part, and the second source with the second output, creating the second alternating current between the electrode and the welded part, in this case the electric welding unit is a system of electric arc welding for striking an AC welding arc between the electrode and the part. Other distinctive features are also given. Patent of Ukraine 74884. W.S. Hjuston, R.K. Mayers, E.K. Stava (Lincoln Global Inc. USA) [2].

Method of nonconsumable electrode gas-shielded two-pass arc welding of pipe circumferential butt joint without edge preparation characterized by that incomplete penetrations from the inner and outer side at rotation of the circumferential butt joint, form a melt continuous along the entire thickness of edge penetration, for this purpose activated flux is applied on the edge surface and welding energy of not more than 0.95 of the heat input in each pass and not less than 1.20 for both passes is maintained to achieve through penetration. Patent of Ukraine 74936. V.M. Kulik, M.M. Savitsky, A.F. Lupan et al. (E.O. Paton EWI) [2].

Installation for resistance butt welding of a pipe shell with a plug characterized by that the terminal of the plug electrode holder is made as a slide, and stop element envelops the electrode holder slide and is fastened on the case ---- as a guide of the latter from the side of welding chamber, sealing elements being located on the end surface of stop element, that is turned to cup-like case, as well as between stop element and electrode holder slide. Patent of Ukraine 65292. N.A. Lavrentiev, N.N. Belash, V.S. Krasnorutsky (NNTs «Kharkov Physical-Technical Institute») [2].

Coating composition for surface protection from sticking of molten metal spatter characterized by that it contains brown coal and sugar as carbon-containing compounds, as well as caustic soda and water with the following ratio of components, wt.%: 10–20 of brown coal; 1.0–4.0 of caustic soda; 10–20 of sugar; the balance being water. Patent of Ukraine 64435. V.A. Kucherenko, O.V. Pogrebnoj (Trade-Industrial Company «Partner») [2].

Method of electric arc surfacing with two automatic machines characterized by that current supply is additionally provided to the middle of the part, and value of current, flowing up to the middle is set, depending on the current that flows to the ends, by the following expression: $I = (1.3–1.6)I_1$, A, where I is the value of the current that flows to the middle of the part, A; I_1 is the value of the current that flows to the end of the part, A. Patent of Ukraine 75256. V.S. Bojko, S.V. Schetinin, V.V. Klimanchuk et al. (Priazovsky STU, Company «Ilyich Mariupol Metal Works») [3].

Surface modification that includes putting into relative motion the part and the powerful flame in the crossing direction, in order to subject a number of regions on the product to the influence of powerful flame; and in each region putting the powerful flame into motion in a number of directions with respect to the workpiece is done beforehand in a preset way, so that in each region the workpiece material is melted and transferred under the action of powerful flame in such a way as to form a recess or a hole. Patent of Ukraine 75144. B.G.I. Dance (The Welding Institute, Great Britain) [3].

Flux-cored wire for underwater welding of steel 17G1S characterized by that its sheath is manufactured from commercial purity nickel, and the core has an additional content of calcium fluoride, potassium fluozirconate, feldspar and aluminum at the following ratio of components, wt.%: 8–10 of potassium fluorzirconate; 4–10 of feldspar; 4–6 of aluminum; the balance being calcium fluoride, while flux-cored wire filling coefficient is 22–25 %. Patent of Ukraine 75174. S.Yu. Maksimov, A.G. Radzievskaya, A.G. Pirogov (E.O. Paton EWI) [3].

Thermit pencil welding method performed with the electrode, manufactured from steel wire and covered with fine chalk on silicate glue, the thermal pencil being also manufactured from steel wire, coated by aluminum and iron filings applied on silicate glue; and mounted at the pencil end is a cap from Berthollet salt applied on the silicate glue that initiates burning and metal welding. Declaration Patent of Ukraine 13200. R.N. Nabok [3].

Exothermal rod for thermal-oxygen underwater metal cutting with automatic ignition characterized by that the head part of the rod contains a combustible cartridge, the length of which is equal to 0.1–0.2 of the rod length, and the mentioned cartridge has a central hole of 1–3 mm diameter, and contains an initiator cap. Other distinctive features are also listed. Declaration Patent of Ukraine 12966. B.V. Lebedev, V.G. Lebedev, A.P. Rudinsky [3].

Exothermal rod for thermal-oxygen underwater metal cutting characterized by that the pipe inner diameter (case of up to 500 mm length) is 10–18 mm, elements that burn in oxygen are cartridges, the height of which is not more than two of their diameters, pressed from powder materials, that burn in oxygen with a high specific heat of combustion, the mentioned cartridges being connected to each other in such a way that the rear part of previous cartridge is connected to the main part of the next cartridge, forming a solid rod. Declaration Patent of Ukraine 12967. B.V. Lebedev, V.G. Lebedev, A.P. Rudinsky [3].

Rod for thermal-oxygen underwater metal cutting in a technological sheath characterized by that the inner diameter of the sheath is 8–18 mm, one or a few elements are made from a material that burns in oxygen with high specific heat of combustion, they are enclosed in a sheath, and have a central elongated hole of 1–3 mm diameter, and the rod may have random length and random cross-section. Declaration Patent of Ukraine 12968. B.V. Lebedev, V.G. Lebedev, A.P. Rudinsky [3].

Exothermal rod for thermal-oxygen underwater cutting made of a bar of a random cross-section that can be inscribed into a circle of 6–16 mm diameter, with an inner central hole of 2–3 mm diameter, manufactured by rolling, extrusion, or casting from a material that burns in oxygen with a high specific temperature of combustion, for instance, from magnesium, aluminum, titanium and / or other alloys. Declaration Patent of Ukraine 12969. B.V. Lebedev, V.G. Lebedev, A.P. Rudinsky [3].

Exothermal rod for thermal-oxygen underwater metal cutting characterized by that the pipe inner diameter (case length of up to 500 mm) is equal to 10–18 mm, and wires that burn in oxygen take up 0.7–0.9 of the pipe inner volume and have a diameter of 0.7–1.0 mm. Declaration Patent of Ukraine 12970. B.V. Lebedev, V.G. Lebedev, A.P. Rudinsky [3].

Method of electroslag surfacing characterized by that surfacing is conducted at an angle of 10–75° to horizontal surface, and at the same time the surfaced blank is rotated relatively to mould, and the latter is moved along the surfaced blank with the speed that is determined by control sensor of liquid metal level, and consumable electrode of a cylindrical shape is fed to the molten pool with the preset speed, that is determined by the surfacing process mode. Declaration Patent of Ukraine 13365. A.V. Popov, B.A. Popov (Company «Latimeria») [3].

Clamping device characterized by that the mechanism of a flexible element tension is made in the form of flexible ties that are mounted in parallel to one another and fastened by axles on a spatial frame in its lugs at the edges, and by a chain traction in the middle. Other specific features are listed. Declaration Patent of Ukraine 13158. N.V. Shabaldak, O.E. Shkanov (Company «Golovnoj Spetsializirovanny KTI») [3].

CASPSP
SOFTWARE FOR COMPUTER SIMULATION OF PLASMA SPRAYING PROCESS
(Version 3.11)

CASPSP is a package of applied programs for computer simulation of turbulent plasma jets used for plasma spraying of coatings, as well as simulation of movement and heating of spray particles. This software allows sufficiently fast quantitative estimation of spatial distribution of temperature and velocity of plasma in a jet, as well as paths, velocities and thermal conditions of spray particles depending upon the spraying process parameters.

CASPSP-3.11 is a new version of the developed software. It comprises two interrelated modules:

- CASPSP — Simulation of Plasma Jet;
- CASPSP — Simulation of Spray Particles.

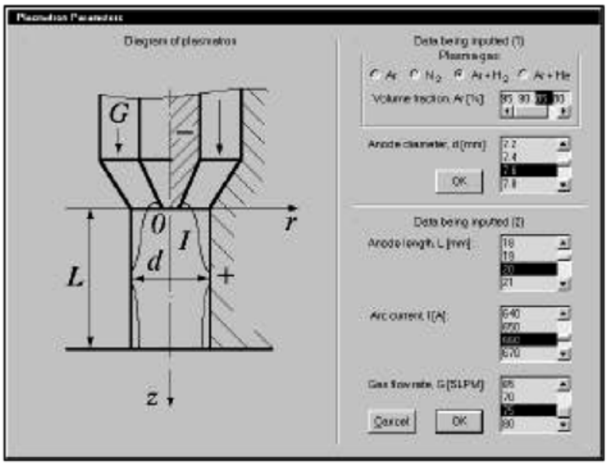

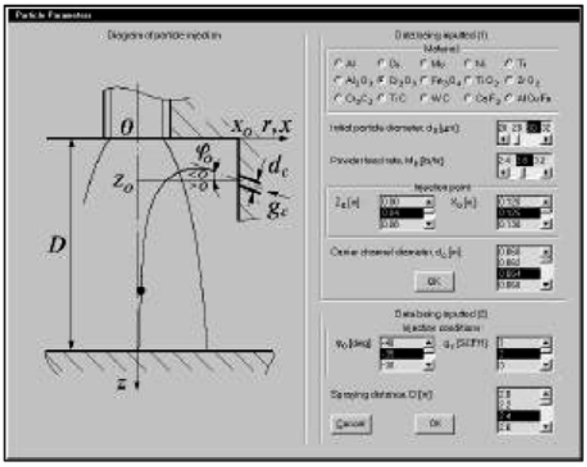

This software has a user-friendly interface (English) for operation in Windows 9x / NT / 2000. In addition to the control menu, it comprises the following systems for each module:

- input / output and data processing system;
- system for graphical display and printing out of simulation results;
- help system.

The first module is intended for simulation of turbulent plasma jets formed by plasmatrons with a smooth channel, which flow out into an atmospheric pressure environment (APS). The corresponding computer software is based on the mathematical model of gas dynamics and heat transfer in thermal arc plasma described by a system of MGD equations in an approximation of the turbulent boundary layer. This module makes it possible to compute, display and print out spatial distributions of temperature and velocity of the plasma jet with allowance for the electric arc processes occurring in a plasmatron, depending upon dimensions of its nozzle set up as anode, arc current, composition and flow rate of the plasma gas.

The second module is intended for simulation of behaviour of spray particles in the plasma jet with preliminarily calculated distributions of temperature and velocity of plasma. The corresponding software is based on the mathematical model of heating and acceleration of a spray particle, which is described by a non-linear thermal conductivity equation and equation of movement for a spherical particle in the plasma flow. This module makes it possible to compute and display the path, velocity and temperature field of a spray particle depending upon the material and initial diameter of the particle, as well as conditions of its introduction into the plasma jet.

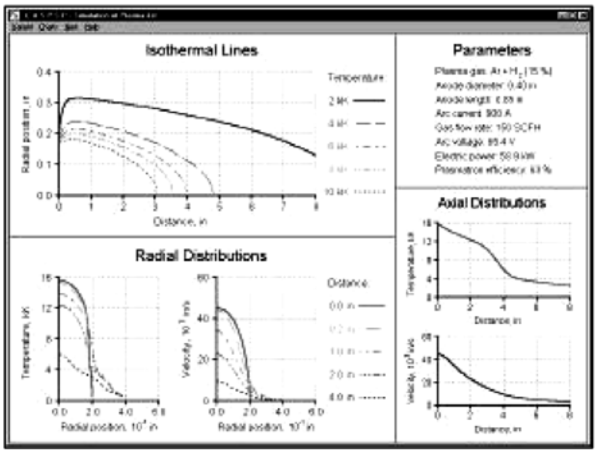

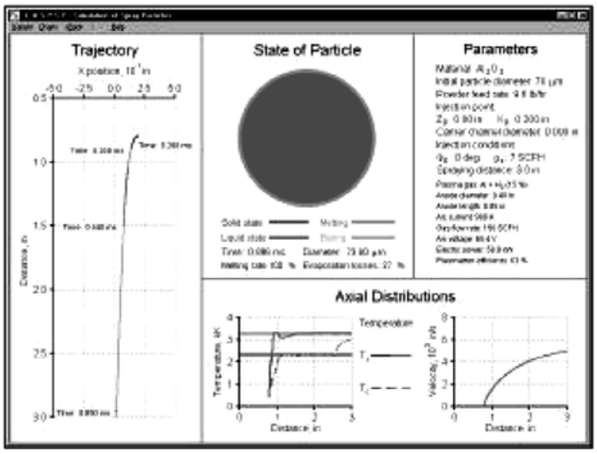

The new version of the software (version 3.11) allows selection of different measurement units for entered and derived data:

- size (cm | in);
- temperature (K | F | °C);
- gas flow rate (SLPM | SCFH);
- powder consumption (kg / hr | lb / hr).

This program product can be further upgraded.

Databases: plasma gas (Ar, N_2, Ar + H_2, Ar + He); particle material (Al, Cu, Mo, Ni, Ti, Al_2O_3, Cr_2O_3, Fe_3O_4, TiO_2, ZrO_2, Cr_3C_2, TiC, WC, CaF_2, AlCuFe).

The databases can be updated.

Requirements to computer. IBM PC or compatible with operational system Windows 9x / NT / 2000, XP / 2003. Minimum 64 Mb working memory. Minimum 5 Mb free space HDD. CD-ROM (software is supplied on CD). Monitor with resolution of minimum 1024×768 pixels. Preferably colour printer.

Application. This software can be useful for specialists, post-graduates and students involved in plasma spraying.

Proposals for co-operation. Full version of the software: CD and user manual (36 pp.). Price — UAH 7000. The software can be optionally modified at a customer's request.

Demonstration version: http: / / www.plasma.kiev.ua

Prof. Krivtsun I.V.
E-mail: borisov@pwi.ru.kiev.ua

REAL-TIME AUTOMATIC SEAM TRACKING AND OBSERVATION SYSTEM RASTR FOR EBW

The principle of obtaining information on the state of the workpiece surface by scanning with a probe — a sharp-focus electron beam.

At a similar cost the main advantages of RASTR in comparison with the optical and television systems are no optical illuminators, which are contaminated by the metal vapors; and the operator working under comfortable conditions.

Principle and application. The image of a 60 × 60 mm section in size containing the weld, the weld pool and the joint forms 3 times per second when the beam scans over the surface of the component within a short period. The process of electron beam welding does not exclude the possibility of its interruption for this short period of time $\tau_{int} = 0.1(d / v_w)$, where d is the diameter of the beam; v_w is the welding speed. For d = 1 mm (the size of the beam typical of powerful guns) at v_w = 6 m / h (1.7 mm / s) the interruption of the welding process for τ_{int} < 60 ms does not cause any disturbance in weld formation. At v_w = 60 m / h (17 mm / s) this time decreases to 6 ms. During these periods the welding beam maybe switched to the probing mode and the butt, the weld pool and the weld in the immediate vicinity of the pool maybe visualised. At the same time, the system automatically computes the value of mismatch between the position of the joint and the weld during welding and using mechanisms or a deflection system aligns the beam with the butt line.

Technical data of the system

Number of samplings, pixel	256 × 256
Dynamic error of the joint tracking, mm	±0.1

System works with power units of ELA type of 15, 60 and 120 kW power.

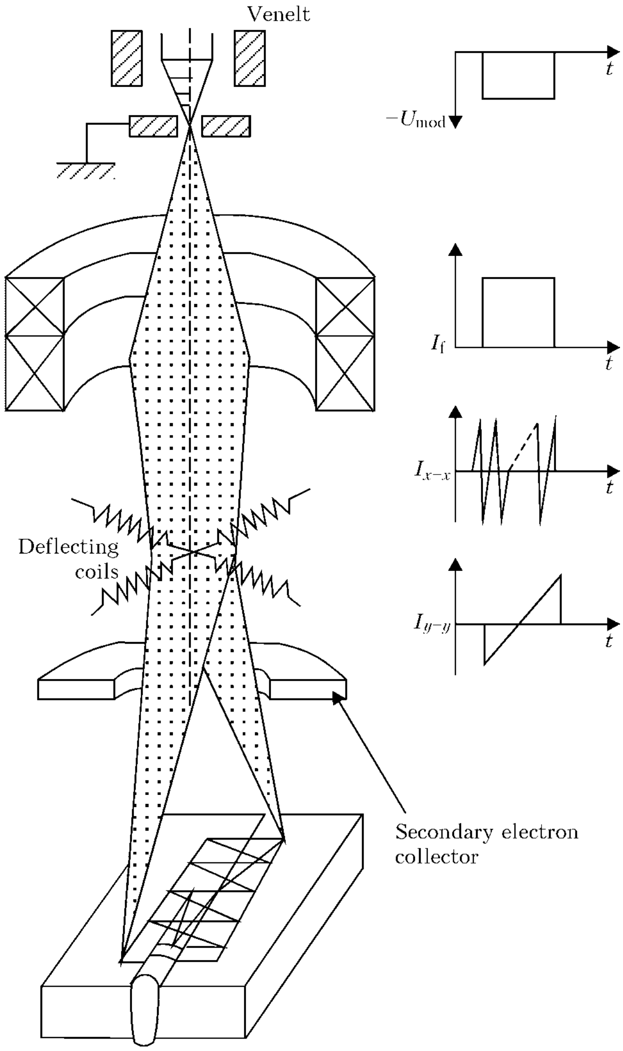

Principle of secondary electron image formation at EBW

Prof. Nazarenko O.K.
E-mail: nazarenko@technobeam.com.ua
http: / / www.nas.gov.ua / pwj / beam
http: / / paton.kiev.ua / eng / inst / ntkstructure / deplist / 571.html